# 3D Electron Density Imaging using Single Scattered X rays with Application to Breast CT and Mammographic Screening

by

Eric Peter Van Uytven

A thesis submitted to the Faculty of Graduate Studies

in partial fulfillment of the requirement

for the degree of

DOCTOR OF PHILOSOPHY

Department of Physics and Astronomy

University of Manitoba

Winnipeg, Manitoba, Canada

THE UNIVERSITY OF MANITOBA

FACULTY OF GRADUATE STUDIES

*****

COPYRIGHT PERMISSION

# 3D Electron Density Imaging using Single Scattered X rays with Application to Breast CT and Mammographic Screening

BY

Eric Peter Van Uytven

A Thesis/Practicum submitted to the Faculty of Graduate Studies of The University of Manitoba in partial fulfillment of the requirement of the degree

DOCTOR OF PHILOSOPHY

## ABSTRACT

Screening mammography is the current standard in detecting breast cancer. However, its fundamental disadvantage is that it projects a 3D object into a 2D image. Small lesions are difficult to detect when superimposed over layers of normal tissue. Commercial Computed Tomography (CT) produces a true 3D image yet has a limited role in mammography due to relatively low resolution and contrast.

With the intent of enhancing mammography and breast CT, we have developed an algorithm which can produce 3D electron density images using a single projection. Imaging an object with x rays produces a characteristic scattered photon spectrum at the detector plane. A known incident beam spectrum, beam shape, and arbitrary 3D matrix of electron density values enable a theoretical scattered photon distribution to be calculated. An iterative minimization algorithm is used to make changes to the electron density voxel matrix to reduce regular differences between the theoretical and the experimentally measured distributions. The object is characterized by the converged electron density image.

This technique has been validated in simulation using data produced by the EGSnrc Monte Carlo code system. At both mammographic and CT energies, a scanning polychromatic pencil beam was used to image breast tissue phantoms

containing lesion-like inhomogeneities. The resulting Monte Carlo data is processed using a Nelder-Mead iterative algorithm (MATLAB) to produce the 3D matrix of electron density values. Resulting images have confirmed the ability of the algorithm to detect various 1x1x2.5 $mm^3$ lesions with calcification content as low as 0.5% ($p<0.005$) at a dose comparable to mammography

## ACKNOWLEDGEMENTS

First and foremost, I would like to thank my supervisor, Stephen Pistorius, for taking me under his wing. His guidance and support were invaluable to me, and his insightfulness and academic rigor were an inspiration to me. Were it not for my discretion in writing this section, Stephen would probably want me to reference my claims. I hope to maintain warm professional relationship with Stephen in years to come.

I would like to extend special thanks to my advisory committee, who have generously donated their time and effort to my work. These people are Dr. Stephen Pistorius, Dr. Richard Gordon (co-supervisor), Dr. Norm Davison, Dr. Jason Fiege, and Dr. Boyd McCurdy. Thanks as well to the external examiner, Dr. Robert Leclair, who provided valuable contribution to this work.

Thanks to my many friends and colleagues, who have either helped me complete my work or retain my sanity. These people include Niranjan Venugopal, Peter Potrebko, Krista Chytyk, Heather Andres, Jorge Alpuche, David Niven, Jenna King, Cristian Mosquera, and Sylvia Cenzano. Special thanks to Christine Mazur for supporting me during trying times.

Thanks to information services, who provided the computational resources I needed to get the job done, and thanks for repairing my laptop the, oh, dozen times or so it died on me.

Thanks to all women with breast cancer. Your stories and courage in the face of adversity is an inspiration.

Finally, thanks to my parents. I could carry them on my back for the rest of my life and still not repay my debt to them.

To all women

## TABLE OF CONTENTS

## TABLE OF FIGURES AND TABLES

### CHAPTER 1: OVERVIEW

No figures or tables.

### CHAPTER 2: INTRODUCTION



### CHAPTER 3: MODELING PHOTON INTERACTIONS

## CHAPTER 4: DISCRETE SCATTER FLUENCE PREDICTION

## CHAPTER 5: DATA ACQUISITION AND ALGORITHM DESIGN

## CHAPTER 6: APPLICATION TO COMPTON CT DURING ALGORITHM DEVELOPMENT

## CHAPTER 7: COMPTON COHERENT SCATTER RADIOGRAPHY

# 1

# Overview

## 1.1 A Brief on Breast Cancer

Breast cancer is a cancer of breast tissue, occurring when malignant cells in the breast grow out of control and ultimately invade the rest of the body. Large collections of abnormal cells are called tumors, and may either be benign or malignant depending on whether or not they spread to the rest of the body. Although breast cancer occurs predominantly in women, it also occurs in men with an incidence that is one percent of the total rate. In women, the tumors may grow for several years before they are large enough to be felt in the breast. While epidemiological risk factors and biological markers have been discovered, the underlying cause of the majority of breast cancer remains a mystery. Thus, there is a large focus on early detection and treatment. The single most important factor for prognosis and outcome is lymph node involvement. Decreased survival rates are associated with positive lymph node involvement.[2] Early tumor detection is critical as the longer the cancer is left untreated, the higher the probability of metastasis.

Breast cancer is the most prevalent type of cancer in women. During their lives, women living to ninety years old in industrialized countries have an approximately one in nine chance of developing breast cancer. Currently, approximately one million women worldwide suffer from breast cancer, and the disease is, after lung cancer, the second most fatal form of cancer in women.

## 1.2 Breast Screening

As a step in increasing breast cancer survival, most industrialized countries have introduced a program of regular breast screening with the intent of detecting breast cancer before it is palpable. X ray mammography* is currently standard in routine breast cancer detection. In a mammographic procedure, each breast is compressed between two plates and exposed to a dose of low energy x rays. The planar distribution of transmitted x rays is recorded using either analog (film) or digital (flat panel) media. Multiple views may be taken in an effort to improve detection of lesions which may be obscured by normal structure in a single view. The radiologist then reads the mammograms, looking for the presence of malignant disease. If and when the radiologist detects an abnormality, the patient is typically referred for a diagnostic mammogram. This procedure involves using magnification or specially angled films. Ultrasound may also be used as a follow-up diagnostic test due to its ability to distinguish between benign

* In this thesis we associate the term mammography with projection imaging of the breast.

and malignant lesions. The patient may also receive a biopsy, where a small amount of breast tissue is removed for analysis.

The use of routine mammographic screening has proven benefits, yet remains controversial. Recognition of the limitations of mammography have led some researchers to study the feasibility of alternative imaging modalities, presented in the next chapter. However, these methods are currently either too novel, too costly, or too time intensive to replace mammography as a primary screening tool at present.

## 1.3 Thesis Objective and Layout

There exists another source of diagnostic information in mammography which has not been exploited. When a mammographic procedure is performed, scattered x rays are produced by the interaction of the primary x rays with breast tissue. A portion of these scattered x rays go on to exit the breast, some in the direction of the detector. As scattered x rays are seen as a contaminating factor in conventional imaging, they are typically removed by an anti-scatter grid which is placed downstream of the breast immediately in front of the detector plane. However, the presence of this anti-scatter grid may introduce a dose penalty up to a factor of three[3].

Breast computed tomography (CT) is a promising technique under development, offering the potential for sensitivity and specificity superior to mammography and offers 3D imaging with a resolution of approximately 1 $mm^3$.

A cone beam approach is often taken to breast CT where scatter is also seen as a contaminating factor.

The hypothesis of this thesis is that the scattered x rays that reach the detector can be used to reconstruct a 3D electron density image of the breast. In the case of mammography, this could be achieved without major alterations to a mammographic imaging system, saving the cost of replacing current screening equipment. By supplementing the traditional film or flat panel detector with a energy sensitive semiconductor array of detectors, this technique has the potential to simultaneously improve sensitivity and specificity of the mammographic screening process while reducing dose due to the removal of the previously necessary anti-scatter grid. The ability for a radiologist to consult both a high resolution mammogram and a CT-like image of electron density would promote a higher detection rate, and subsequently an overall improvement to the breast screening process.

# 2

# Introduction

## 2.1 Early Cancer Markers in the Breast

The human breast is a modified skin organ, composed of varying amounts of adipose, connective, and glandular tissue, with the function of nurturing the young by the production of milk. Mammary glands within the breast consist of several lobules which produce milk. The milk is transported through 10-20 lactiferous ducts which drain from the lobules to the nipple. The proliferation and destruction of breast tissue cells is controlled through hormonal regulatory mechanisms. The morphology of the breast is undergoing constant change, and for a particular woman the amount of ductal, lobular, and adipose tissue can vary as a function of age and hormonal status. Irregularity in these mechanisms may occasionally lead to morphological changes in the breast. These morphological changes may either be benign (such as the dilation of ductal passages during pregnancy) or malignant (such as the formation of a carcinoma). Cysts may occur as a result of the accumulation of fluid, milk, calcium, collagen, fibroblasts, inflammatory cells, or mucin.[4] While benign, these cysts are palpable, and may require further diagnostic follow-up. More importantly, however, a mutation in

the epithelial cells of the ductal or lobular systems may lead to formation of malignant breast tissue. In its very early stages, this malignant breast tissue has very low contrast relative to healthy tissue, and is therefore undetectable. However as the lesion grows in size, it develops certain features which distinguish the involved duct or gland from the rest of the breast. Calcium deposits in the lesion increase its density on a radiograph, and any increase in malignant mass may lead to distortions in the ductal structure, which is noticeable on a mammogram to a trained radiologist.

The circumstances surrounding malignant lesion formation are not fully understood. A large focus in breast cancer control has been on detection of the lesion at an early stage, before the cancer has had a chance to metastasize. To do this, many authors have focused their efforts on identifying cancer markers. Ng et al.[5] have studied malignant tumors with in-vivo neutron activation, and have found the accumulation of several trace elements. They postulate that the presence of these elements in growing malignant tissue provides a chemical environment leading to the formation of small microcalcifications, a significant feature of benign and malignant lesions. Microcalcifications are tiny deposits of calcium, and typically occur in various shapes ranging in diameter from 0.1-1 mm (average: 0.3 mm). Calcification deposits have high contrast on mammograms due to their high relative radio-opacity, and are significant cancer markers when occurring in clusters of three or more within a square-centimeter region of a mammogram[6]. Sometimes no localized deposits of calcium are visible in a lesion, however higher calcium content contributes to an increase in physical and

electron density of the lesion over glandular tissue of up to 5%. Following the work of Ng, Buchbinder et al.[7] found that malignant tumors contain a higher calcium content on average than benign tumors.

Murphy et al.[8] studied the correlation between carcinomas and benign tumors, and discovered that in 31 cases where clustered microcalcifications were apparent, 35% of biopsies revealed cancer while 50% were benign. They concluded that microcalcifications were sensitive, but nonspecific cancer markers.

However, other authors who have studied the problem report findings that indicate calcifications are the best indicator of carcinoma.[9] Lanyi[10] has commented on the importance of calcifications as cancer markers, stating they are "the most important leading symptom in mammographic detection of preclinical carcinomas". Millis et al.[11] found that calcifications were apparent on mammograms 49% of the time when carcinoma was confirmed following a biopsy. A histological study revealed that calcification was present in carcinomas 63% of the time. In contrast, calcifications were only present in benign tumors 20% of the time.

Other features of malignant tissue are related to the manner in which the lesions grow, and are often characterized by the shape of the lesion boundary. Sickles et al.[12] closely studied 300 cases of nonpalpable breast cancer. They concluded that the most dominant indication of malignancy was clustered microcalcifications, which appeared in 42% of all cases. Other signs included rod, curvilinear, and branching shapes (23% of all cases), other structural changes

(20% of all cases), dominant masses with smooth margins (23% of all cases), and dominant masses with margins typical of carcinoma (16% of all cases).

## 2.2 Mammography

Mammography, the standard in breast screening, is the oldest modality for breast cancer detection. Mammography is still the screening test of choice for breast cancer since it is both cost- and time-effective, though the sensitivity and specificity of the test is highly operator dependant.[13] The goal of mammography is to detect nonpalpable breast lesions at an early stage, as several authors have pointed out the correlation between increasing tumor size and the probability of metastasis.[14-16] There is still debate in the medical community regarding the success of mammography as a screening tool. While some studies have failed to find the benefits of mammography,[17, 18] the majority of studies have shown a clear correlation between the use of a routine mammographic screening program and increased survival.[19-25] Screening mammography has shown the ability to decrease the mortality due to breast cancer by 30%.[26] A review performed by Zhou and Gordon[27] concluded when small cancerous tumors were found early using mammography, the women enjoyed a five-year survival rate of 82%, whereas the survival rate for women without early detection was only 60%.

Ultimately, the goal of mammography as a screening test is 100% sensitivity and 100% specificity. Sensitivity is defined as the probability of a positive test among patients with disease, while specificity is defined as the

probability of a negative test among patients without the disease. A mammographic test lacking in either sensitivity or specificity increases the burden on medical resources. A low sensitivity, evidenced by a low true positive rate*, implies the test is poor at identifying early cases of cancer. The missed lesions have a higher likelihood of metastasizing, adversely affecting both the patient and medical resources allocated to breast cancer treatment. On the other hand, a poor specificity indicates a large number of false positives†, where a healthy patient is referred for useless time consuming follow-up tests such as cytology, biopsy, and ultrasound. The sensitivity and specificity of a diagnostic test are correlated, and a compromise must be found between sensitivity and specificity. In the U.S., the false positive rate for women who underwent yearly screening over a five year period was 2.9%, while the rate for women undergoing intermittent mammography (more infrequent than once a year) was 4.6%.[28] More recent studies have indicated that the false positive rate can vary from 1.5% to 24.1% depending on radiologist (27,394 mammograms over 1067 radiologists).[13] These errors are costly and approximately US$100M is spent every year in the U.S. on follow-up breast cancer testing.

CAD (computer-aided diagnosis) systems have been recently developed to assist the radiologist in locating mammographic lesions. The CAD algorithms have been designed to improve image quality, enhance mammographic features, and highlight potential areas of cancer development. Their effectiveness is as yet

* The true positive rate is defined as the percentage of cases where a test returned positive where the cancer was actually present.

† The false positive rate is defined as the percentage of cases where the test was negative when a cancer was actually present. Also equal to (1 – specificity)

unclear. A study performed by Destounis[29] revealed that 71% of cancers missed by a radiologist were detected using a CAD system. In a second study, a CAD system outlined 6 lesions for biopsy that a radiologist did not, and all turned out to be cancerous. Another recent study of CAD in mammography has reported sensitivity of 0.71-0.8 and specificity of 0.86, with no improvement through the use of computer assisted diagnosis.[30] One difficulty in identifying lesions is the problem inherent in mammography: a mammogram is a 2D projection image of a 3D structure. In locating calcifications, this is not necessarily a drawback, as calcifications are rarely found in the breast in any great number, and calcifications appear with high contrast against background structure noise. However, like radiologists, CAD programs also try and locate structural abnormalities indicative of non-calcified lesions. However, when the complete 3D structure of the breast is collapsed onto a 2D imaging plane, structural abnormalities may be distorted and hidden by overlapping structures. As a result, structural noise in the mammogram may confuse the CAD algorithm. Destournis found that their CAD algorithm was too sensitive, flagging twice as many non-cancerous masses as the radiologist, which is the consequence of an overly low specificity. These results indicate that 3D imaging of the breast may greatly assist the ability of both radiologists and CAD to identify anomalous structures in the breast.[31]

Despite the successes of mammography, approximately 20% of women who are diagnosed with breast cancer will die of the disease in five years[32] due to metastasis of the lesion. Studies like these have fueled considerable opposition to mammography. Firstly, the routine exposure of women with cancer to x rays

have been shown to promote the formation of new cancers,[33] though recent studies are unable to correlate mammography with increased risk,[34] or are satisfied with the benefit/risk ratio.[35] Despite good specificity, one of the limitations of mammography is the large false negative rate* associated with women with dense breasts. Several authors have investigated the factors which limit the sensitivity and specificity of breast cancer. Since the majority of screening cases are normal, it is difficult to track false negatives in cases where a patient has a cancerous lesion which was missed during the mammographic test. To do this, retrospective studies must be performed. When a patient is diagnosed with cancer, researchers can study prior mammograms which were read as negative. Often, the signs of a lesion were present but were missed by the radiologist. One study reports as many as 10-30% of cancerous lesions are missed during routine mammographic screening.[36] Birdwell[37] performed a retrospective study of 115 breast cancers in a attempt to determine where mammography was failing. Specifically, their case studies were of negative mammograms of women who were later diagnosed with malignant tumors. The signs of cancer retrospectively visible on the negative mammograms were mass lesions in 70% of cases and calcifications in 30% of cases. Distracting non-malignant lesions were cited as a dominant factor in the production of false negatives. Maxwell et al.[38] performed a similar study. They found that the largest correlation was from microcalcifications, which was undetected due to low radiographic density and/or masking by structure. Approximately 25% of cancers

* Cases where the radiologist fails to detect existing cancerous lesions in a mammogram is referred to as a false negative (FN). Cases where the mammographic test is positive where no cancer is present is referred to as a false positive (FP).

exhibited microcalcifications in earlier mammograms, while 15% had either masses or deformities. All other cases had no indications on earlier mammograms. The authors concluded a 'striking' correlation between microcalcifications and the later development of breast cancer. Also, the authors concluded that calcifications less than 500 $\mu$m are often missed (23%) in screening mammography, and are likely to correlate with invasive ductal carcinomas.

These studies indicate that mammography may be deficient when attempting to locate small abnormalities surrounded by overlapping structures, even if there is disagreement regarding the type of abnormality that is most often missed. Unfortunately, as previously stated, there is a significant loss of information associated with imaging a 3D object with a 2D modality. The ability of an x-ray screening test, such as mammography, relies upon its ability to identify those features associated with cancer. When structural noise is not an issue, mammography excels at detection of high contrast fine structure (such as microcalcifications) due to the high imaging resolution (~20 lp/mm). However, larger low contrast lesions may be missed due to overlapping tissues. To illustrate this, Figure 2.1 illustrates the difference in mammograms between women with fatty and dense breasts. The presence of disease is clearly more difficult to detect in the right image, where the higher radio-opacity is due to dense fibrous and glandular tissue, and hinders the radiologist's ability to detect the presence of lesions. Additionally, women are deterred from participating in a mammographic screening program due to the discomfort of undergoing breast compression.[39]

Another aspect which detracts from the ability of mammography to detect small lesions is the limitation in the dose delivered to the patient. Positive cancer detection relies on the differences in x-ray attenuation between normal and malignant lesions. However, these differences only become apparent at very low x-ray energies. At these lower energies, x rays are much more readily absorbed, increasing image noise and depositing higher doses. As diagnostic x rays have been found to be cancer inducing, the mammographic dose is kept to a maximum of approximately 3 mGy[40], the dose one would receive from cosmic rays flying from New York to Los Angeles.

In an effort to achieve detection earlier than is possible with mammography, several cancer detection modalities have been investigated, including clinical exam,[41] self exam,[42] ductal lavage,[43, 44] microwave imaging,[45] ultrasonagraphy,[46] optical tomography,[47] positron emission tomography (PET),[48, 49] ultrasound,[50] x ray CT,[51, 52] and magnetic resonance imaging[53] (MRI).

However, none of these modalities have been able to replace mammography in terms of detection performance, non-invasiveness, screening time, and cost-effectiveness. Despite its problems, mammography is the only widespread radiological technique in use today for breast screening.

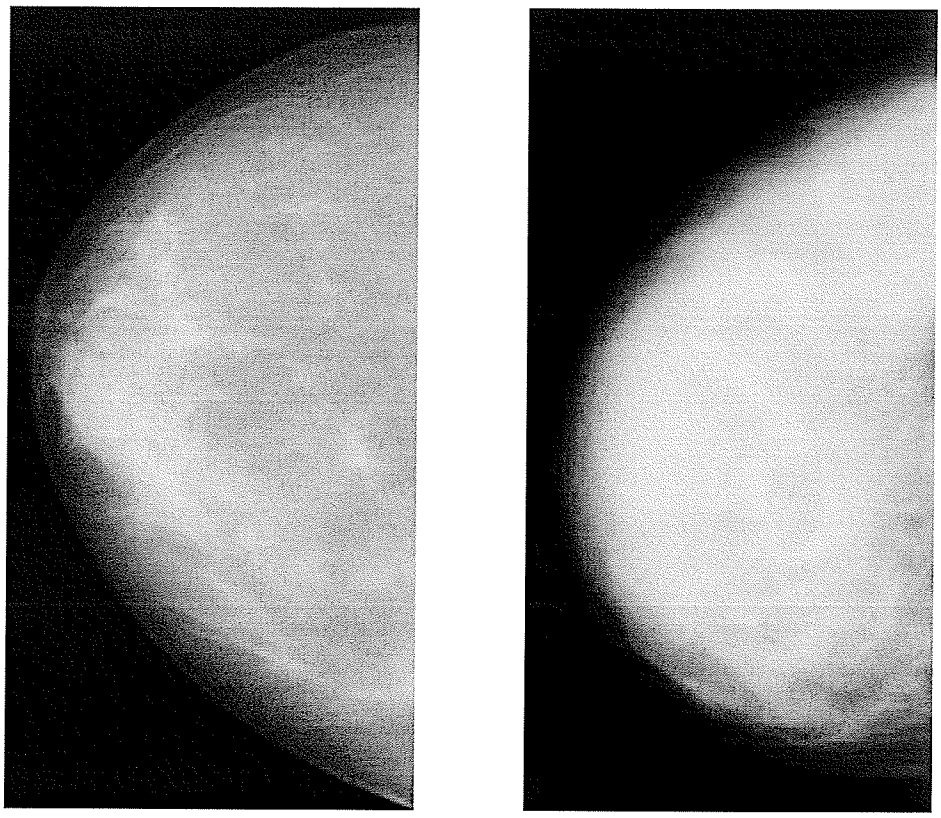

Figure 2.1: Fatty (left) and dense glandular (right) breast composition.

## 2.3 Past and Present Applications of Scattered X ray Imaging

Tissue densitometry is a technique involving the accurate determination of physical or electron density at a point within the target object. Lale[54] first devised a method of tissue densitometry based on Compton scatter. The target is irradiated with a polyenergetic high energy pencil beam, and a collimator is designed to accept single scatter photons originating from a small target volume in the object (Figure 2.2). In principle, the target could be scanned through the beam to obtain a full 3D electron density image. In 1968, Lale[55] developed a method for patient scanning using a megavoltage system designed using the principles of his earlier work. Despite promising results, several drawbacks existed with the system, such as mechanical collimation problems, poor resolution (2.5 cm x 3 mm x 3 mm), and slow scanning times.

In 1974, Farmer and Collins[56] built upon Lale's idea. Using an energy-discriminating Ge detector, they extended the field of view (FOV) from a point to a line, based on the principle of angular and energy discrimination. This novel technique improved imaging resolution and decreased scanning time. However, they reported a low signal-to-noise ratio (SNR) as well as geometric and mechanical problems. Some of these problems such as low SNR were attributed to the small acceptance solid angle of a single point detector. To overcome this issue, a plan for a multi-detector system was introduced in the paper, but no such system was ever constructed to my knowledge. Furthermore, the authors

encountered a loss of contrast and resolution due to multiply-scattered photons and attenuation artifacts.

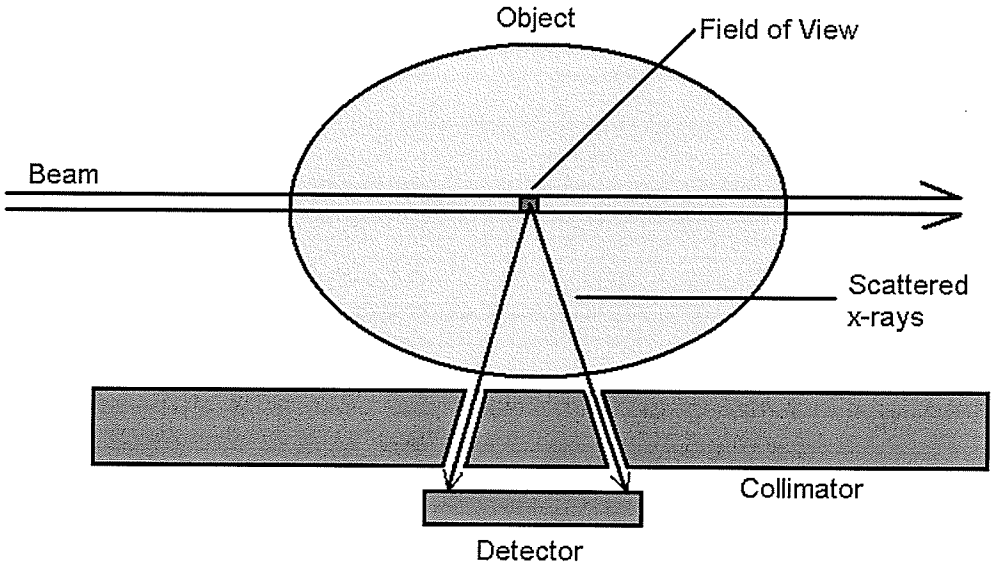


Figure 2.2: Single point tissue densitometry system devised by Lale measures scattered photon fluence and reconstructs electron density in the point FOV.

In a paper published in 1977, J.J. Battista et al.[57] investigated the effect of multiple scatter and attenuation artifacts on a Compton scatter system. Using an experimental system, the authors investigated the ratio of multiple-to-single scattered photons reaching a collimated detector at an angle approximately 45° from the incident beam. Using a dual-energy windowing technique, the multiple scatter was estimated and corrected. To correct for attenuation, an iterative method to estimate 3D attenuation coefficients was developed, using the attenuation of the incident beam as the primary source of information. Imaging a

homogenous test object, the implementation of corrections improved the uniformity of the resulting image significantly, where the pre-correction image contained significant electron density gradient artifacts. Relative to the original cylindrical phantom, the image has a precision of better than 5%, however, the corrections were limited to the aforementioned 45° scattering angle, and thus had limited usefulness for other scattering angles.

Battista et al. published a follow-up paper in 1978[58], expanding their model to allow scattering angles from 30° to 130°. The energy of the incident monoenergetic beam was variable, ranging from 300-2000 keV. They imaged a 0.3 $cm^3$ volume in a 25x25x25 $cm^3$ water phantom and obtained a 0.5% electron density accuracy. The authors made several important observations:

1) Multiple scatter reaching a collimated detector may be minimized but never fully eliminated. This places an upper limit of the accuracy of collimated Compton scatter techniques.

2) As the energy of the incident beam is increased (from 300keV to 2000 keV), the multiple-to-single scatter ratio decreased, however the dose as a function of energy increased 400% over this energy range.

3) Forward scatter imaging was optimal, where both multiple scatter and dose decreased significantly as the scattering angle was

reduced from 130° to 30°. The multiple-single scatter ratio reduced from 122% to 27%, while the dose decreased from 143 mGy to 12 mGy.

These observations were all predicted, confirmed by experiment, and reproduced by other authors.[59] In 1981, the authors reported good progress on the application of their system to radiotherapy planning.[60] While reporting an electron density accuracy of 4.3% with a spatial resolution of 0.5 cm, the conclusion of the paper was that there was little further progress possible for whole body Compton scatter imaging. However, other authors were more hopeful.[61]

Brateman et al.[62] applied a scatter CT technique using a softer beam (~70 kV) to image an 8 cm cylindrical phantom containing an imhomogeneity. Curiously, no quantitative information was reported, however this author estimates a 0.5 cm imaging resolution.

Achmad et al.[63] devised a technique of determining the electron density at a point within a large volume object at kilo-voltage energies. As no rotation was involved, one could consider it a single projection technique. Using a single collimated source and two collimated detectors, the authors devised a mathematical method of obtaining attenuation data within the object by swapping the source and detector, and exploiting the polychromatic nature of the beam. Using this technique, they managed to determine the electron density of points within the object to an uncertainty of 0.1%-0.7%, and the method has proven to

be robust, performing well even with the introduction of attenuating objects of various densities.

Several in vivo Compton scatter scanners have been proposed for various applications. El Khettabi et al.[64] proposed a 400 kV brain scanner which could potentially produce 3D electron density brain scans with a single projection. Testing their method with Monte Carlo N-particle Transport (MCNP) measurements, they have obtained 3D electron density images with a voxel resolution of 130 $mm^3$ and uncertainty of approximately 10%. A follow-up method was presented by Arsenault et al.[65] The reconstruction model proposed by Arsenault is unique in its ability to use fan beams, however no experimental or Monte Carlo simulated results were presented.

The potential of scatter imaging specific to mammography was revealed in 1984 by Dance[66] and more recently by Boone.[67] Both authors investigated the scatter-to-primary ratio (SPR) in mammography under a variety of test conditions. For the average compressed breast thickness of 5.2 cm, the SPR proved to be in excess of 0.5, indicating a potential to apply scatter imaging to a mammographic geometry.

The concept of coherent scatter imaging has also been investigated. Batchelar[68] et al. devised a CT system using low angle ($<10^{o}$) coherent scatter x rays for analysis of bone mineral content, an application previously investigated by Clarke et al.[69, 70] Leclair and Johns[71, 72] investigated material analysis using integrated Compton/coherent scattering, and suggested their model might be used for more generalized scatter imaging.

## 2.4 Compton Coherent Scatter Radiography – A Novel Imaging Algorithm

### 2.4.1 Rationale

In section 2.2, we reviewed the studies of many authors who have studied the limitations of mammography. Retrospective studies have shown that small lesions obscured by overlapping structural noise present the major challenge to improvement in sensitivity and specificity. The problem is large enough that many investigations have been performed via alternative imaging modalities. However, other established modalities are unsuitable for screening in some way, (Table 2.1) and only breast CT (including variations such as tomosynthesis) seems suited to wide scale mammographic screening. In section 2.3, we have reviewed the chronological progression of Compton and coherent scatter imaging, and have seen many authors demonstrate the extraction of information from scattered x rays.

The main impetus of this work is the hypothesis that scatter imaging can be incorporated easily into a conventional primary x ray imaging system. In this fashion all the benefits of the primary modality are retained, while the limitations are mitigated through the proven imaging capabilities of scatter imaging. Furthermore, the use of x ray scatter already present in the image provides an avenue for reducing the required dose to provide a superior screening test.

### 2.4.2 Theory

Using Compton and coherent scattered photons, this thesis proposes an algorithm which functions as a 3D imaging technique specially adapted to mammographic purposes. Hereafter, the algorithm shall be referred to as CCSR (Compton-coherent Scatter Radiography). We hypothesize that the distribution of single scattered x ray radiation, differential in both energy and position, contain sufficient information for 3D electron density reconstruction of the target object. Moreover, we also hypothesize that in the absence of noise, a unique electron density solution exists for each scatter distribution (see Appendix B). Using known physics and certain assumptions (presented later), we may analytically calculate the single scatter distribution produced by the interaction of a radiation beam with an arbitrary object. Following the aforementioned assumption that a unique target configuration produces a unique scatter spectrum, the algorithm iteratively determines the target electron density configuration which minimizes the differences between measured and calculated scatter distributions. The major challenges associated with this technique are associated with an uncollimated imaging geometry. Since the geometry is uncollimated, single scatter and multiple scatter will both be recorded on the detector planes. In order to reconstruct from single scatter, multiply scattered photons (accounting for a significant percentage of scattered photons) must be properly predicted and subtracted from the total distribution. To allow this, our algorithm iteratively predicts the resulting distributions of both single and multiply scattered photons.

Furthermore, in order to effectively predict the distribution of single scattered photons, the energy dependent attenuation (beam hardening) and scatter of the incident polyenergetic beam must be accounted for.

Table 2.1: Some popular new candidates for breast screening: benefits and limitations

| **Modality** | **Benefit** | **Limitation** | **Current Use** |
|---|---|---|---|
| MRI | 3D, no dose, higher contrast | Cost, doesn't detect small calcifications | Characterization of suspicious lesions |
| Breast CT | 3D, higher contrast, patient comfort | Lower resolution compared to mammography | Breast screening (clinical trials) |
| Ultrasound | No dose | Higher screening time, low detail, not approved by FDA for screening | Characterization of suspicious lesions, image guided biopsy |

One of the primary objectives of this thesis was to design an algorithm which would function under the most realistic conditions possible. The early versions of the algorithm were basic, using monoenergetic beams and unrealistic physical and geometrical assumptions. Following a period of rigorous testing, the

complexity of the algorithm was increased, subsequently removing more and more approximations. At each major step, the algorithm was tested, using certain criteria to define whether or not the testing phase was successful. We designed and tested the algorithm entirely in a simulated environment. We relied upon the EGSnrc photon transport package as discussed in section 2.5, coupled with simulated but realistic phantoms to provide us with data similar to experiment.

### 2.4.3 Application

One of the unique features of CCSR is the potential ability to create 3D breast images. Other modalities have been proposed for 3D imaging of the breast, including microwave imaging,[45] ultrasound,[50] and MRI,[53] however none of these are as yet suited for routine screening. In this work, we present three applications for CCSR, two of which involve breast screening.

First, we show how CCSR may function to enhance breast CT. Recently, Boone et al. have introduced a dedicated breast CT scanner for breast screening.[51] The imager can perform a scan in 17 seconds, and the authors claim it can find tumors as small as 5 mm. For their clinical trials, which are currently underway as of this writing, 190 women have registered. Chen et al.[52] performed a feasibility study and concluded that breast CT offers potential for improved low-contrast detectability and tumor localization. CCSR may be integrated into breast CT by introducing energy sensitive detectors in the CT detector array. CT image reconstruction would involve processing both primary and scatter data to create

two separate images of attenuation and electron density, respectively. The addition of an electron density image adds atomic information not otherwise present in the primary CT image. If breast CT does show potential for routine high-sensitivity breast screening, CCSR may still be used to boost the sensitivity through signal enhancement, noise reduction, and proper scatter prediction.

Secondly, as an adjunct to mammography, CCSR offers the radiographer a means of supplementing a 2D projection image with a 3D electron density image. As malignant lesions demonstrate higher electron density they could be detectable using CCSR. The lesions will provide higher contrast against background structures because attenuation values are not being integrated in the dimension perpendicular to the imaging plane as is the case with mammography. In addition to the potential improvement in sensitivity, tumor localization information at time of screening could be used to estimate the probability of metastasis to axillary lymph nodes.[73]

A third potential application is the Compton spectrometer, which relies on a functional relationship between atomic composition in the target material and scatter distributions. As such, it is possible to discriminate the scatter spectra belonging to materials of varying atomic compositions. If a pencil beam of photons is used to irradiate a small sample of biological material, the elemental composition of the sample may be reconstructed from the resulting scattered photon spectrum.

It has been demonstrated that performing a needle biopsy on some types of cancer may provoke metastatis.[74] Normally, a forming tumor is encapsulated by

biological boundaries, limiting its rate of growth. However, when a needle biopsy is performed, cancer cells may spread through the needle hole and metastasize to the rest of the body. While we only examine *in vitro* spectroscopy of a small tissue sample in this work, it may be possible to perform Compton spectroscopy *in vivo*, eliminating the need for performing a needle biopsy.

## 2.5 The EGSnrc Monte Carlo Photon Transport Package

Monte Carlo methods are part of the class of algorithms used to simulate mathematical and physical processes. By using stochastic random number generators, these methods aim to reproduce the physical system as accurately as possible. Monte Carlo methods are typically used to simulate systems with many degrees of freedom, where large computational speed gains over purely analytical or numerical solutions can be achieved or where analytical/numerical solutions are not available.

The EGSnrc[75] Monte Carlo radiation transport package is a Monte Carlo code which specializes in simulating the transport of photons, electrons, and positrons through matter. For each input particle, a history is determined by transporting the particle in small steps, checking for matter interactions, and following any secondary particles which are produced. Typically, the end of a single photon history corresponds to one of three events:

- the particle leaves the active geometry

- the particle is removed as a result of certain interactions such as the photoelectric effect or pair production.
- the energy of the particle drops below a certain threshold value due to various interactions, at which point all the energy is deposited locally.

The algorithm uses RANMAR[76], a pseudo random number generator, which produces an uncorrelated sequence of numbers associated with a particular seed value. For each interaction, several random numbers out of the sequence are used to determine the specifics of the interaction. For example, three random numbers are generated during a Klein-Nishina Compton scatter interaction to determine the photon scattering angle. The history of each individual particle is highly stochastic. However, as the number of simulated particles increase, deterministic trends start to occur, and the algorithm begins to approach the results of an analytical system.

The first medical physics paper with Monte Carlo in either the title or abstract[70] was published in 1967 by Bentley,[77, 78] and since then the use of these algorithms in the area of medical physics has exploded. Following this publication, the number of Monte Carlo publications in the area of medical physics has doubled every five years up to the year 2000.[77] In this period, following Moore's Law,[79] computer power per unit cost has approximately doubled every 18 months per unit cost, and this increase is partially responsible for the proliferation of Monte Carlo studies.

The use of Monte Carlo in medical physics is pervasive, with applications in brachytherapy,[80] commercial treatment planning,[81-83] diagnostic x ray applications,[84] and radiation protection.[85] Monte Carlo is a trusted method in medical physics, especially evidenced by the drive to convert dose calculation methods in treatment planning systems to the Monte Carlo method,[77] removing the need for conditional approximations leading to dose inaccuracy. The AAPM (American Association of Physicists in Medicine) has recently approved a Task Force report on the application of Monte Carlo techniques to clinical treatment planning.[86]

We have used the EGSnrc Monte Carlo transport package exclusively for the simulation of our experimental data. Using the Fano theorem[87] to simulate a situation which can be computed analytically, EGSnrc was the only Monte Carlo package proven to be accurate to its own cross sections to within 0.1%.[88, 89] The use of Monte Carlo was mainly due to necessity, though convenience and cost-effectiveness was certainly a factor.

During the development of this algorithm, many factors needed to be evaluated and taken into account. Our development strategy was to start from the ground up, designing and testing our imaging algorithm for the most basic and trivial circumstances. At first, we completely neglected coherent and multiple scatter processes, allowing us to evaluate results in a highly controlled simulated environment. Once the acquired images were satisfactory, we moved on by removing approximations or testing more complex phantoms. However, when problems occurred, there were only a limited number of factors to consider.

In designing the algorithm, it was critical to accurately predict the scatter photon distributions. Systematic prediction errors at mammographic energies can bring large variations to the output, with detrimental effects to the inverse imaging algorithm. The adjustable variables in our simulation create a parameter space of several dimensions, all which have an effect on the scatter distribution. These variables include, but are not limited to:

- beam width
- beam spectrum
- phantom compositions and spatial arrangement
- detector area
- detector energy resolution
- air gap size

The power of EGSnrc allows us to explore this parameter space without experimental limitations. Ultimately, the parameters we select must be realistic, but in the design phase, we created simplifying conditions which allowed us to fully understand the physics involved and design the scatter model accordingly.

Finally, we benefit from full separation of single and multiple scatter in EGSnrc. This has allowed us to design a multiple scatter prediction model which operates independently from our single scatter model. After each model was successfully tested, they were combined into a successful algorithm which images electron density while compensating for multiple scatter contamination.

Systematic sources of error in EGSnrc may include programming errors, modeling errors, and cross section inaccuracies. The EGSnrc package has been in development for decades with numerous applications, reducing the possibility of large programming and modeling errors. Furthermore, the work introduced in this thesis confirms that if we use the same cross sections as EGSnrc, we can reconstruct the scatter distributions from first physical principles with a systematic error less than 0.1%.

Systematic inaccuracies are likely present in the EGSnrc cross sections. EGSnrc uses a standalone program, PEGS4,[90] to generate cross section data. The user creates an input for PEGS4, consisting of the relative elemental composition of the material as well as the physical density. From this information, PEGS4 combines elemental cross sections to obtain the cross section data for the compound, which is subsequently stored in a data file for later use. The elemental cross sections used in PEGS4 have been obtained using experimental data,[91, 92] and errors in these data tables will propagate throughout EGSnrc. Current versions of EGSnrc use the XCOM cross section database[93], available online. For this database, Hubbell[94] estimated the error in mass attenuation coefficients from 5 keV to a few MeV at 1-2%. The error in Compton cross sections was also estimated at approximately 1%. The cross section data we used for our work has been obtained from the same sources for the elements hydrogen, carbon, nitrogen, oxygen, phosphorous, and calcium. In our forward model, we combine the cross sections of these elements in an additive fashion.

As we are using the exact same cross sections in our algorithm as those used in producing our experimental data, we have effectively removed this source of error. As the algorithm is in a relatively early stage of development, we did not investigate the effects of a systematic error in cross section. However, since electron density is proportional to the Compton scattering cross section, the theory indicates that the error in cross section would translate to a corresponding error in electron density of approximately 1%.

# 3

## Modeling Photon Interactions

## 3.1 Properties of photons

The photon is a quanta of electromagnetic radiation which has several distinct attributes. Physical properties of the photon include:

- position
- frequency
- momentum
- zero rest mass
- lack of electric charge
- two possible polarization states
- two possible helicity states

In this work, we focus on the extracting information from scattered photons related to the position and frequency only. The interactions we discuss in this chapter relate to the absorption or scattering of photons, and our simulated detectors measure only position and frequency (or energy) of the scattered photon. While it may be possible to extract information from the other properties of photons, that is outside the scope of this work.

In sections 3.2-3.4, we will discuss the three major scattering and absorption interactions. Section 3.5 introduces a functional relationship between electron density of sample of breast tissue and mass attenuation coefficient, an important relation used throughout the rest of this project.

## 3.2 Photoelectric Interactions

The photoelectric effect occurs when a photon interacts with a bound atomic electron. The photon transfers all its energy to the electron and the electron is ejected from the atom with a kinetic energy equal to the energy transferred from the photon minus the electronic binding energy. Below 100 keV, the electron rapidly loses its energy through Coulomb interactions with other atoms, effectively depositing its energy locally.

The photoelectric interaction may be considered the most important photon interaction at low energies as it is both the primary source of deposited dose and the means in which the majority of diagnostic x ray imaging techniques derive their information. At mammographic energies, most photons interact through photoelectric absorption. For energies below 100 keV, the approximate photoelectric cross section is given by the following relation[95]:

$$\tau \cong k\frac{Z^4}{h\nu^3} \tag{3.1}$$

where $k$ is a constant, $Z$ is the atomic number of the atom, and $h\nu$ is the energy of the incident photon. Units are $cm^2$ per unit volume.

It is important to note that the mass attenuation coefficient of the photoelectric effect is strongly dependent on the atomic number $Z$. This allows for the discrimination of different tissues in diagnostic transmission radiology. For example, consider breast tissue and calcified breast tissue, two types of tissue very similar in density and mean atomic number. For this example, let breast tissue be a mixture of 50/50 adipose/glandular tissues, while letting carcinoma be the same breast tissue impregnated with 1% Calcium Hydroxyapatite ($Ca_{10}(PO_4)_6(OH)_2$) by weight. The mass attenuation coefficients are plotted as a function of energy in Figure 3.1. The small difference in mean atomic number ($Z_{glandular}$=7.5 versus. $Z_{carcinoma}$=7.7)[96] results in a percentage difference between the two mass attenuation curves that is larger at lower energies due to the photoelectric effect. Johns and Yaffee[96] concluded that the mass-attenuation coefficients of fibrous and malignant tissue are experimentally indistinguishable at energies higher than 31 keV. Thus, mammography operates at low energies in order to provide contrast between these similar tissues. Relative attenuation differences between tissues will be taken into account for Compton scatter imaging as well, and will be explained in more detail in section 3.4.

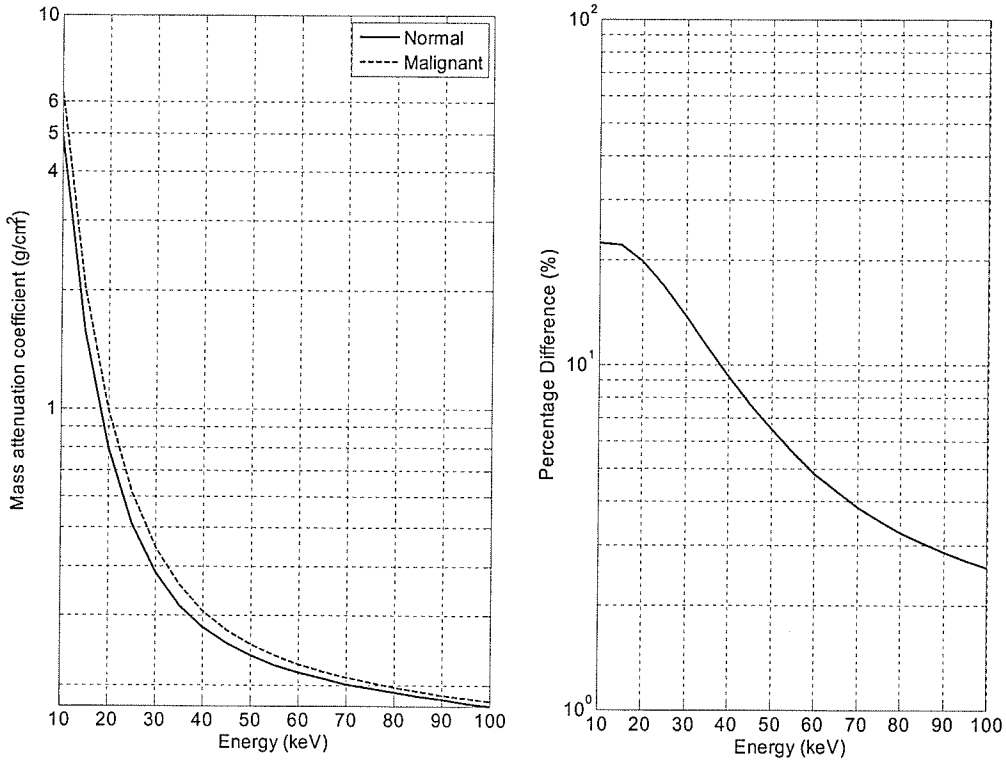


(a) (b)

Figure 3.1: (a) Mass attenuation coefficients of normal breast tissue (solid line) and carcinoma (dashed line) as a function of energy. (b) Percentage difference between the two curves of panel (a).

## 3.3 Compton Scatter

A Compton interaction occurs when an incident photon scatters inelastically off a bound or free electron, transferring a partial amount of kinetic energy. After interacting with an electron, a secondary photon is produced with reduced energy and a scattering angle related to the reduction in energy. The electron is ejected from the atom at an angle that obeys conservation of momentum, and at low energies, it deposits its energy locally. Since a secondary photon is produced, the volume of interaction between the primary beam and the material can be considered a secondary radiation source.

### 3.3.1 Klein-Nishina Cross Section

The majority of scattering algorithms employ Klein-Nishina (KN) scattering physics, which applies Dirac's relativistic theory of the electron to the Compton effect to obtain improved cross sections. However, KN physics carries two simplifying approximations regarding the scattering electron: (1) they are unbound electrons and (2) the electrons are at rest. Under these approximations, the kinematic relationship between the incident photon energy $K_0$, scattered photon energy $K$, and scattering angle $\theta$ is given by:

$$K = \frac{K_0}{1 + K_0(1 - \cos\theta)} \tag{3.2}$$

where the energies are given in units of the electron's rest energy $m_o c^2$. The Klein-Nishina differential cross section in $cm^2$ per electron per unit angle differential in scattering angle $\theta$ is given by:

$$d\sigma_{KN} = \pi r_0^2 \left(\frac{K_0}{K}\right)^2 \left[\frac{K_0}{K} + \frac{K}{K_0} - \sin^2\theta\right] \sin\theta d\theta \tag{3.3}$$

where $r_o$ is the classical electron radius.

### 3.3.2 Doppler Broadened Cross Section

When the approximations of section 3.3.1 are removed, a significant energy broadening occurs around the scattered photon energy. Accounting for this process is critical to energy sensitive single scatter distribution prediction like CCSR.

The broadened Compton scatter cross section describes the probability of a photon scattering from an initial energy $K$ through a solid angle $\Omega$ into a

scattered energy $K'$, and is given in $cm^2$ per steradian for a single atom under the impulse approximation*[97] by:

$$\frac{d^2\sigma}{d\Omega dK} = \frac{r_0^2 K}{2K_0 q\left(1+p_z^2\right)^{1/2}} XJ(p_z) \tag{3.4}$$

where

$$q = \left|\vec{K}_0 - \vec{K}\right| = \sqrt{K_0^2 + K^2 - 2K_0 K\cos\theta} \tag{3.5}$$

is the scattering vector of the photon, and

$$p_z = \frac{\vec{p}\cdot\vec{q}}{q} = \frac{K_0 K(1-\cos\theta) - (K_0 - K)}{q} \tag{3.6}$$

is the projection of the initial momentum of the electron on the scattering vector $\vec{q} = \vec{K}_0 - \vec{K}$. The function $X$ is given by:

$$X(K_0, K) = \frac{R}{R'} + \frac{R'}{R} + 2\left(\frac{1}{R} - \frac{1}{R'}\right) + \left(\frac{1}{R} - \frac{1}{R'}\right)^2 \tag{3.7}$$

where

* The impulse approximation assumes a non-relativistic interaction where bound electrons are scattered into plane-wave states and electron binding energy is considered negligible in comparison to the interaction energy transfer.

$$R = K\left[(1+p_z^2)^{1/2} + (K_0 - K\cos\theta)p_z / q\right] \tag{3.8}$$

and

$$R' = R - K_0 K(1-\cos\theta) \tag{3.9}$$

$J(p_z)$ is the Compton profile, and can be analytically calculated[97] as:

$$J(p_z) = 2\pi \int_{|p_z|}^{\infty} p\rho(p)dp \tag{3.10}$$

where $\rho(p)$ is the momentum distribution of the scatterer and $p$ is the momentum. Following Brusa et al.[98], contributions from different electron shells are considered separately. Binding effects are taken into account by a step factor $\Theta$ which rejects interactions in which insufficient energy is transferred*:

$$J(p_z) = \sum_i Z_i J_i(p_z)\Theta(K_0 - K - U_i) \tag{3.11}$$

$Z_i$ is the occupation number of shell $i$ and $U_i$ is the binding energy of electrons in shell $i$.

* $\Theta$ (x) = 1 if x $\geq$0, 0 otherwise.

It can be seen from Equation 3.4 that the single atomic Compton cross section is determined by the incident energy, scattered energy, angle, and details of the atomic structure of the scattering atom through the form factor $J(p_z)$. Since Doppler broadening is sensitive to atomic structure, the distribution of electron density of the target is not sufficient information for predicting x ray scatter. This presents both a challenge and an opportunity. If no assumptions are made regarding the target material, the number of convergence variables in the system is increased due to the elemental degeneracy of the voxel electron density. That is, many combinations of elements in the voxel may have the same electron density. Instead of one variable per voxel (electron density), we potentially have $n$ variables (electron density + relative elemental composition), where $n$ is equal to the total number of elements potentially present in the voxel. The opportunity lies in the ability to potentially resolve the elemental composition of a sample material, and preliminary experiments performed in simulation appear to corroborate this hypothesis. (see Chapter 8)

## 3.4 Coherent Scatter

Coherent scatter is a cooperative process, where an incident photon interacts with matter to scatter through an angle $\theta$ while retaining its incident energy. The scattering cross section increases with increasing atomic number $Z$ or decreasing incident energy $K$, and is a significant interaction at mammographic energies.

In this work, the coherent scattering cross section is calculated using the independent atom approximation. The differential cross sections calculated here are for individual atoms, and is given by:

$$\frac{d_A\sigma_C}{d\Omega} = \frac{d_e\sigma_T}{d\Omega} F[q]^2 \tag{3.12}$$

where

$$\frac{d_e\sigma_T}{d\Omega} = \frac{r_0^2}{2}(1+\cos^2\theta) \tag{3.13}$$

is the Thompson differential cross section. This differential cross section represents a theory where the electron is assumed to be free to oscillate under the influence of the incident electromagnetic wave. However, it neglects the fact that atomic electrons are bound and subject to the electromagnetic forces of other intra-atomic particles. Thus, we introduce the unitless form factor $F[q]$, which can be interpreted as the effective charge that scatters a given photon, and is the Fourier transform of the atomic charge distribution. Under the independent atom approximation where interactions between atoms is neglected, this factor can be expressed as a weighted sum of elemental contributions:

$$F[q] = \sum_i p_i F[q, Z_i] \tag{3.14}$$

where

$$q = K\sqrt{\frac{1-\cos\theta}{2}} \tag{3.15}$$

is the factor that contains the dependence of the coherent cross section on energy $K$ and scattering angle $\theta$, and $p_i$ is the fraction of the $i^{th}$ element in the mixture or compound, where $\sum_i p_i = 1$. Recent studies[99] have shown that there are problems with the independent atom approximation, and more accurate experimental form factors are being integrated into EGSnrc as new data becomes available. In this work, we use the individual form factors $F[q, Z_i]$ have been obtained by Hubbell and Øverbø.[100]

## 3.5 Relation between Atomic Composition, Electron Densities, and Attenuation Coefficients

CCSR is a method of electron density distribution prediction. When Klein-Nishina Compton physics is used and coherent scatter is ignored, electron density is the only piece of information required to predict the distribution of scatter for a particular phantom configuration. However, proper prediction of coherent and Doppler broadened cross sections requires some more extensive knowledge of the material in question, namely the atomic composition. A problem arises: how do

we image the electron density of a material without knowing its atomic composition? Fortunately, in breast imaging, there are a limited number of possible tissues present in the breast. Thus, it is possible to approximate a functional relationship between the atomic composition and electron density of each voxel. While the elemental composition of glandular and adipose tissue is known[101], the elemental composition of calcified tissue is not available in the literature. It is however possible to calculate it based on the percentage of calcification present and the chemical formula of the calcification.

Using this information, we can calculate mass-attenuation coefficients based on atomic composition, allowing the calculation of a new functional relationship between mass-attenuation coefficient and electron density. Figure 3.2 illustrates this functional relationship using the materials outlined in Table 3.1. Normal tissues are assumed to range between 0/100 and 100/0 adipose/glandular tissue, and abnormal tissues are assumed to be glandular tissue with calcification content between 0% and 50%. Malignant tissues have been shown to have densities ~1% larger and linear attenuation coefficients ~5% larger than normal tissues[96], indicating a higher effective atomic number. In our model, malignant tissues are modeled by glandular tissue with 0.5-13.8% Calcium Hydroxyapatite calcification content by weight. Any ratio of glandular and adipose not present in the table can be obtained through a process of linear interpolation between the tissues presented in Table 3.1. See Appendix A.

Table 3.1: Density and elemental composition of standard breast tissues and Calcium Hydroxyapatite

| Material | Physical Density | H | C | N | O | P | Ca |
|---|---|---|---|---|---|---|---|
| Adipose Tissue (0/100) | 0.9301 | 0.112 | 0.619 | 0.017 | 0.251 | 0.001 | - |
| Standard Breast Tissue (50/50) | 0.9819 | 0.107 | 0.401 | 0.025 | 0.464 | 0.003 | - |
| Glandular Tissue (100/0) | 1.04 | 0.102 | 0.184 | 0.032 | 0.677 | 0.005 | - |
| Calcium Hydroxyapatite $Ca_{10}(PO_4)_6(OH)_2$ | 3.16 | 0.0839 | 0.313 | 0.0195 | 0.453 | 0.043 | 0.0878 |

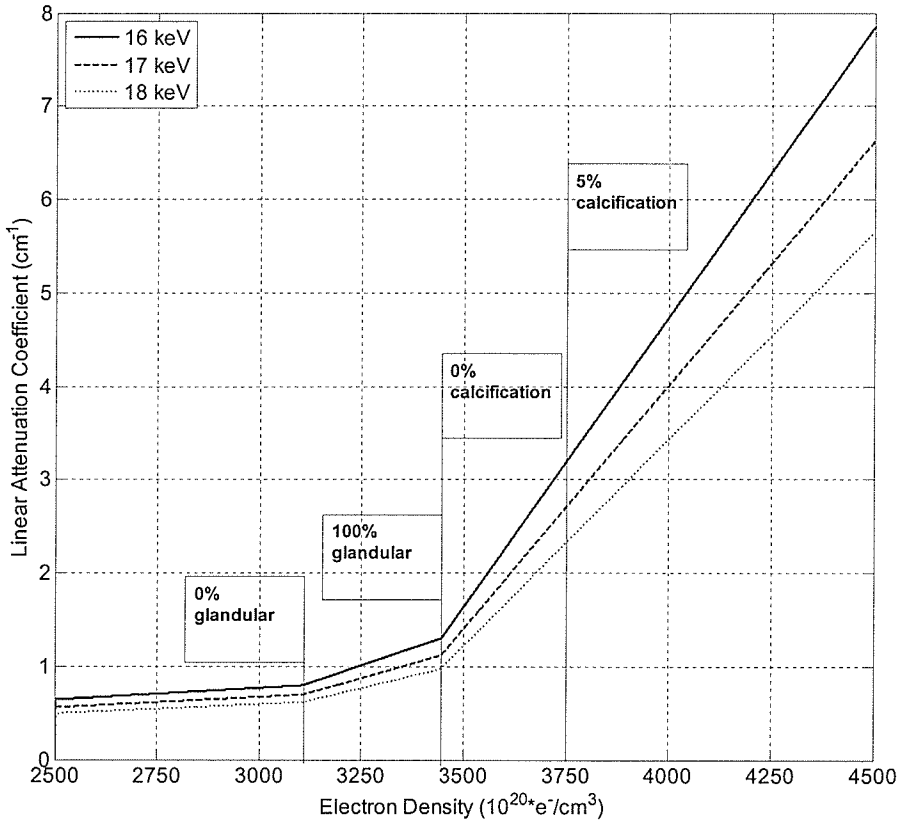


Figure 3.2: Functional relationship between linear attenuation coefficient and electron density for 3 select mammographic energies. Percentage calcification is by volume.

# 4

## Discrete Scatter Fluence Prediction

## 4.1 Required A priori Information

Any scatter prediction model must make initial assumptions or approximations about the material being imaged, since the information needed to analytically calculate scattering distributions (i.e. the electron density distribution, atomic structure) is the object of the imaging procedure. As such, certain approximations and/or assumptions were made during the development of the algorithm. The following list details the relevant approximations.

### 1. Exterior Dimensions of the Breast

In order to successfully calculate the attenuation of scattered x rays, the radiological path length from the point of scatter to the detector is required. There are two major geometries considered in this work, pendulant breast and compressed breast. The determination of the exterior dimensions of the breast is difficult for pendulant forms; however we may overcome this by placing the breast in a water 'sleeve' of known dimensions. This is described in greater detail

in Chapter 7. In the case of compressed breast geometry, the exterior dimensions are easier to obtain, because the breast is compressed into a slab-like geometry where the thickness of the slab can easily be obtained through paddle width measurements. Pliable solid water equivalent material may be used to fill any air gaps left between the compression paddles. This is more fully explained in section 7.2 when dealing with multiple scatter.

Knowing the scatter path length allows for accurate electron density imaging and is considered a necessary a priori parameter in this algorithm.

**2. Average Breast Composition**

Breast structure and composition may vary greatly between women. The most important variation by far is the relative amount of adipose and glandular tissue. Generally, older women have breasts with more adipose tissue than younger women. The percent difference in density between adipose and glandular tissue is approximately 10%, and this difference can account for significant differences in their x ray attenuation properties.

For this project, we have consistently worked with breast material that reflects a 50/50 ratio of adipose and glandular tissue. In the algorithm, we assume a 50/50 ratio when calculating the attenuation of scattered x rays, and thus we assume we know the average breast composition a priori. However, the information provided by the primary mammogram can be used to approximate this ratio prior to scatter reconstruction. Although compositional information as a

function of Z would not be known, the mixture of glandular and adipose tissue is reasonably isotropic throughout the breast.[102]

### 3. Mass-attenuation Coefficients at all Energies for Adipose, Glandular, and Calcified tissue

These coefficients are required to calculate photon attenuation of both primary and scattered x rays. For any energy, the coefficients may be calculated using the elemental composition of the material of interest. Recall from section 3.4 that the electron density of a voxel may be used to obtain its elemental composition. Using this information, the mass attenuation coefficient in $cm^2/g$ is obtained using an additive relation of the component elements:

$$\frac{\mu}{\rho} = \sum_i w_i \left(\frac{\mu}{\rho}\right)_i \tag{4.1}$$

where $w_i$ the percentage of element $i$ present in the mixture by weight. The elemental mass attenuation coefficients $\left(\frac{\mu}{\rho}\right)_i$ are obtained using the cross sections of Storm and Israel.[103] Every iteration, this calculation is performed for each voxel.

## 4.2 Geometry

One of the unique aspects of CCSR is its ability to enable 3D imaging using only a single projection. The basic geometry for the system is shown in Figure 4.1. A finite width pencil beam is used to irradiate the object of interest. Two area detectors are placed upstream and downstream of the object, and capture scattered photons originating inside the object. This technique allows the irradiated volume to be imaged with finite resolution. As illustrated in Figure 4.1, the field of view (FOV) is composed of a column of voxels with resolution defined by the beam dimensions and a user-selectable $z$ value, occurring inline with the beam. To obtain a full 3D imaging capability, the beam may be scanned in $x$ and $y$ directions perpendicular to the beam axis. Two basic variations of the geometry are used:

- In Chapter 6, the phantom is simulated as a cylinder 8 cm in diameter (in the $xy$ direction) and 8 cm thick (in the $z$ direction). All experiments are performed using a central beam position.
- In Chapter 7, the phantom is simulated as a 5x5x5 $cm^3$ cube. A scanning beam is used to image slices of the phantom.

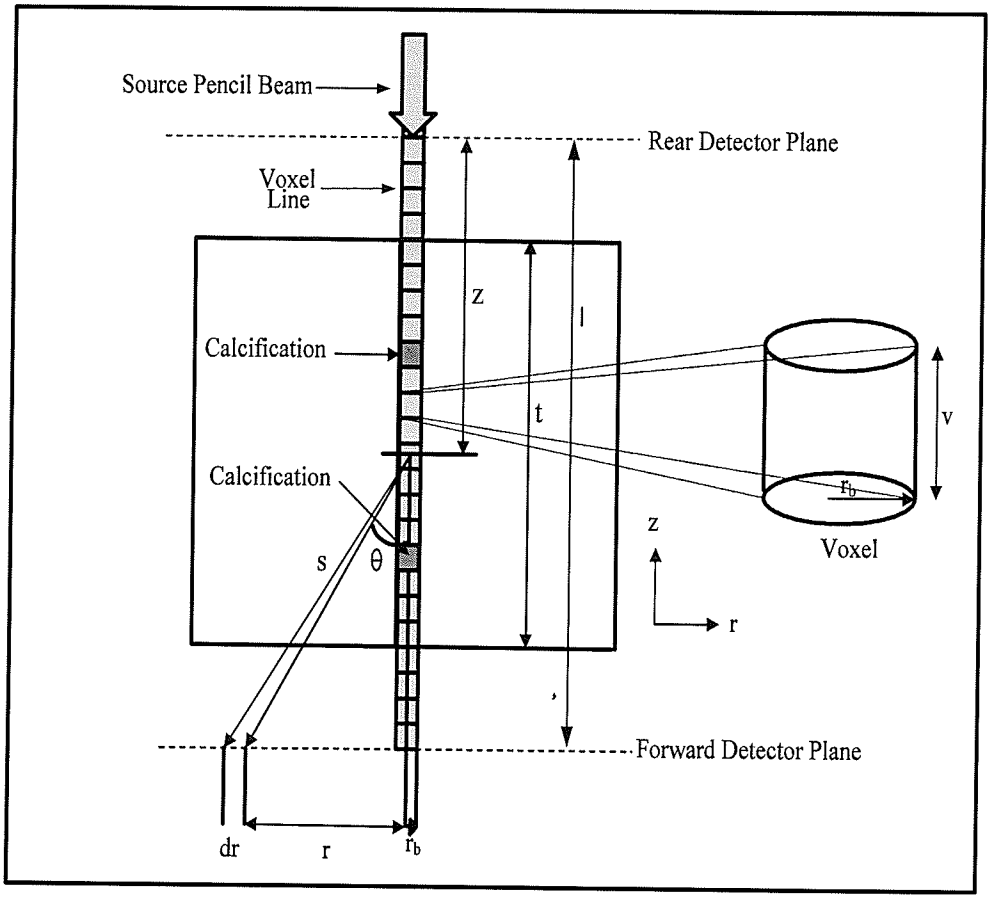


Figure 4.1: Plan view of the phantom, showing pencil beam and imaging FOV (Field of View). The voxel shape is cylindrical for scatter CT (Chapter 6), and cubic for scatter mammography (Chapter 7).

## 4.3 Detector

A detector which was able to record both position and energy of impinging photons was simulated with adjustable binning (i.e. resolution) parameters. To complement the cylindrically symmetric simulation geometry inherent in the Compton scatter cross section, the simulated detector array was

configured as a ring array, instead of the more usual square pixel array (Figure 4.2). The square pixels of a traditional x ray imaging detector are replaced with a series of detector rings, where a ring is defined by boundaries $R$ and $R+\Delta R$. All photons impinging within this radial range constitute one signal. In practice, a square pixel array may also be used, though an extra conversion between Cartesian and cylindrical data spaces is necessary.

The simulated detector parameters are outlined in Table 4.1. We used $\Delta R$ =1 mm spatial resolution for all simulations. Depending on the application, we chose energy resolutions of $\Delta E$=500 eV at CT energies and $\Delta E$=200 eV at mammographic energies.

Table 4.1: Simulated scatter detector parameters.*

| | Minimum | Maximum | Resolution | |
|---|---|---|---|---|
| | | | CT | Mammo |
| Position (cm) | 0 | 10 | 0.1 | 0.1 |
| Energy (keV) | 0 | 100 | 0.5 | 0.2 |

The 1 mm spatial resolution is well within the capabilities of typical flat panel detectors, while a 200-500 eV energy resolution has been achieved using state of the art microcalorimeters. Chow et al.[104] have demonstrated that

* Not to be confused with the primary detector, which may have higher resolution.

superconducting tunnel junction (STJ) detectors can resolve 60 keV x rays with a resolution of 0.07 keV.

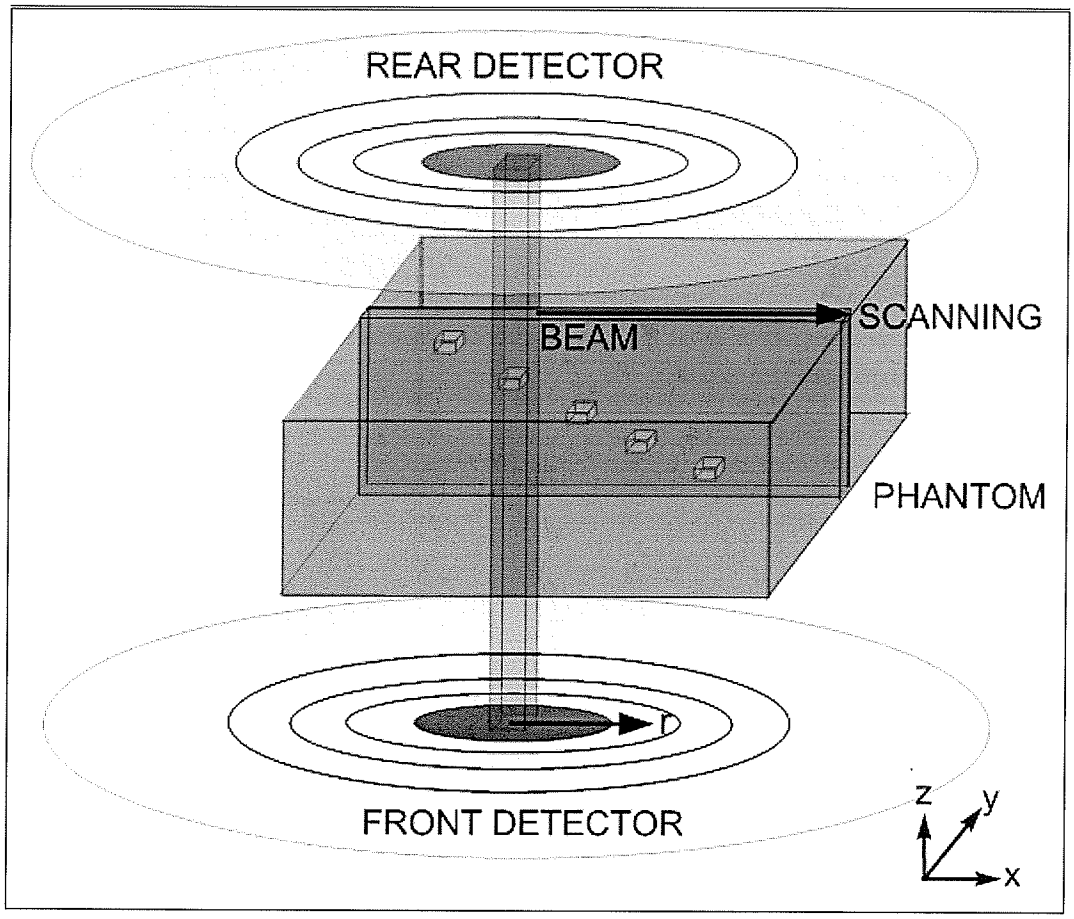


Figure 4.2: Phantom and detector configuration.

However, one disadvantage of STJ detectors is that they require cryogenic cooling, limiting their convenience. Semiconductor detectors do not require cooling, and their energy resolution has been steadily improving over the past 15 years. These detectors would be a good choice for this work, as their freedom from cooling and low cost would allow an easier and more cost-effective implementation of CCSR. Table 4.2 shows the chronological progression of

semiconductor detector resolution over the past several years. If this trend continues, semiconductors would be the material of choice for experimental implementation of this project, though currently not achieving a resolution superior to 200 eV.

The theoretical limit for semiconductor detectors is energy dependent, and is given by the statistical variation in the number of produced electrons which are read out. The average energy required to produce ionization is 2.95 eV in Germanium, 3.62 eV in Silicon, and 4.43 eV in CdTe. The production of electron-hole pairs is a statistical process. Each interaction will produce an ion/hole pair with energies that follow a Poisson distribution, and the fractional energy resolution is given by the following formula[105, 106]:

$$\frac{\Delta E_{stat}}{E} = 2.35\sqrt{\frac{F\delta}{E}} \tag{4.2}$$

where $F$ is the statistical Fano factor,[107] $\delta$ is the mean energy to produce an electron-hole pair, 2.35 is the FWHM factor of the distribution, and $E$ is the photon energy. At mammographic energies (<20 keV), Equation 4.2 yields a statistically limiting resolution of approximately 200 eV. This value drives our choice of energy resolution for that energy range.

Using these simulated detector parameters, the recorded photon distributions are parsed into a two-dimensional 'detector space' with the limits and resolution described in Table 4.1. We use the formalism (R, K) to refer to the area of detector space bounded from radii $R$ to $R+\Delta R$ and energies $K$ to $K+\Delta K$.

Table 4.2: Chronological progression of energy resolution for various semiconductor detectors.

| Year | Energy Resolution | Author | Detector Type | Fano Factor | Statistical Limit Resolution. (keV) |
|---|---|---|---|---|---|
| 1992 | **7 keV** @ 60 keV | Hasegawa | HPGe | 0.15[105] | 0.383 @ 60 |
| 1999 | **1.1 keV** @ 60 keV | Cook | CdTe | 0.11[108] | 0.402 @ 60 |
| 2001 | **0.83 keV** @ 59.5 keV | Tak. | CdTe | 0.11 | 0.402 @ 60 |
| 2005 | **~ 0.425 keV** @ 60 keV | Gehrke | HPGe | 0.15[105] | 0.383 @ 60 |
| 2006 | **~ 0.463 keV** @ 60 keV | Ortek | Si-PIN | 0.15[105] | 0.424 keV @ 60 keV |

## 4.4 Generalized Calculation of Scattered Photon Distributions

A MATLAB algorithm was written to calculate from first principles the number of singly-scattered photons that would be detected in each discrete 2D bin, given the incident photon spectrum, incident beam shape, number of incident photons, and electron density distribution throughout the phantom.

A step-by-step procedure was developed to calculate the number of photons that scatter into the radius-energy (R, K) bin for each voxel along the beam line. The formula presented in this section is generalized and applies to either Compton or coherent scatter. The total is calculated as the sum of the number of photons scattered from each respective voxel. The procedure for calculating the number of photons scattered into each (R, K) bin is as follows.

1. In order to approximate the realistic case of infinite scattering centers* (photons may scatter at any point along the beam line) in a computationally feasible manner the following approach was used. Each voxel is populated with $m$ equally spaced 'scattering centers' along the $z$ axis (Figure 4.3). These scattering centers approximate the scatter originating from a subvoxel of space of thickness $\Delta z$ with the scatter center at the middle. The number of photons originating from

* Why not increase the voxel resolution? We wanted a larger number of scattering centers without a larger amount of convergence variables. In this way, the voxel electron density 'drives' the scattering from all centers within the voxel.

each scattering center is calculated separately using the electron density of the voxel containing the scatter center.

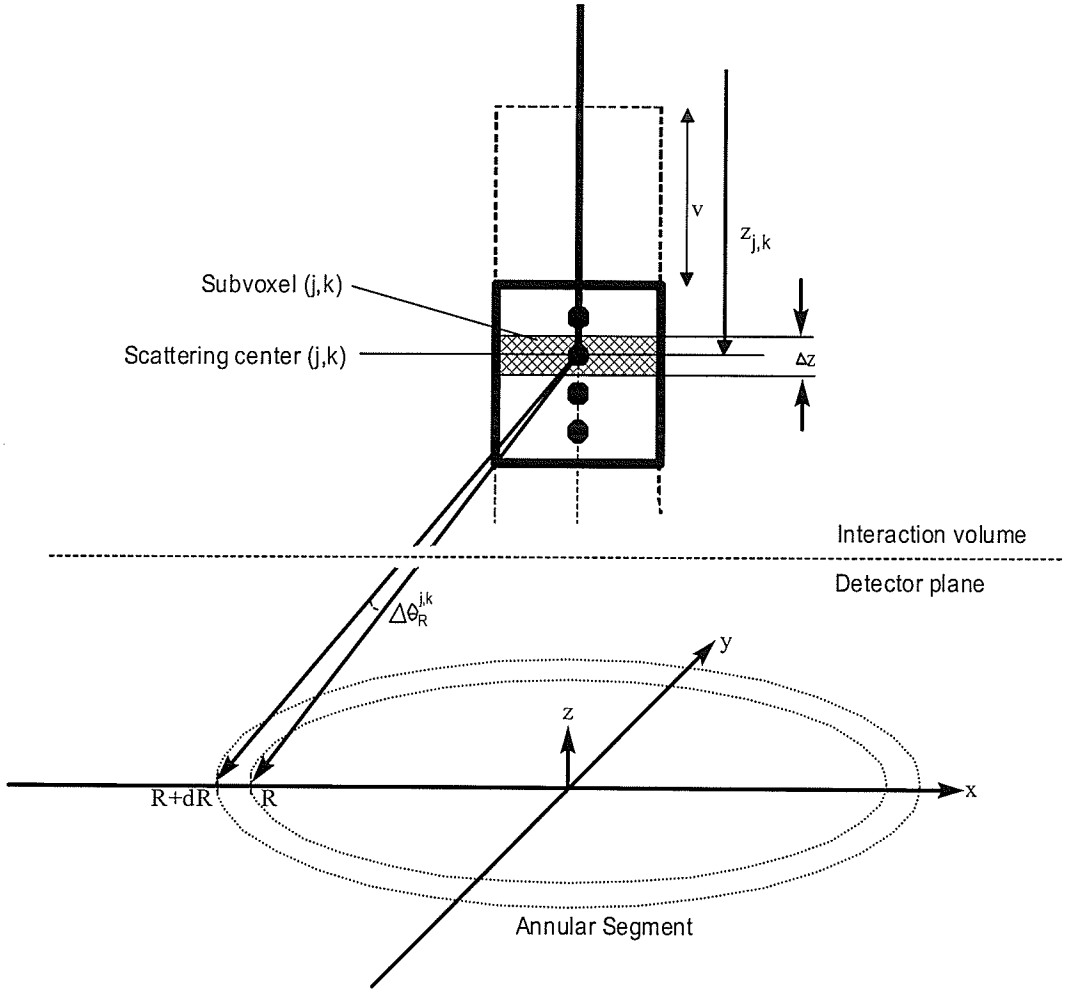


Figure 4.3: A voxel containing 4 scattering centers and 4 subvoxels. $z_{j,k}$ and v are defined in Figure 4.1. A distance between scattering centers of 0.125 cm is considered sufficient to approximate a line source. $\Delta z$ is defined as the distance between two scattering centers. The angular ring spanning from R to R+dR is defined by the index R in the bracket (R, K). The quantity $\Delta\theta_R^{j,k}$ is the angle subtended by the annular strip (R, R+ΔR) measured from the scattering center (j,k).

2. The number of primary photons that reach the TOP of each subvoxel defined by the scattering center is calculated using the number of incident photons, the electron densities, and the attenuation coefficients of all voxels. The number of primary photons $N_0^{j,k}(K_0)$ of energy $K_0$ incident on the top of scattering center $k$ of voxel $j$ is determined by calculating the attenuation of the $N_0(K_0)$ photons from the top of the slab:

$$N_0^{j,k}(K_0) = N_0(K_0) \times \exp\left[\left(\sum_{i=1}^{j-1} -\left(\frac{\mu}{\rho}\right)_{K_0}^{i} \rho_i v\right) - \left(\frac{\mu}{\rho}\right)_{K_0}^{j} \rho_j \left(z_{j,k} - \frac{\Delta z}{2} - v \times (j-1)\right)\right] \tag{4.3}$$

where $N_0(K_0)$ is the mean number of incident primary photons between energies of $K_0$ and $K_0 + \Delta K_0$, $\left(\frac{\mu}{\rho}\right)_{K_0}$ are the mass attenuation coefficients, $\rho_j$ is physical density of the $j^{\text{th}}$ voxel, $z_{j,k}$ is the distance from the top of the phantom to the scattering center $k$ of voxel $j$, and $v$ is the voxel thickness (Figure 4.3). Since the physical density for each voxel is not known, an estimated value is calculated from the electron densities using the following equation:

$$\rho_i \cong \frac{\rho_{e,i}}{\rho_{e0,i}} \times 0.985 \frac{g}{cm^3} \tag{4.4}$$

where $\rho_{e,i}$ is the electron density of the $i^{th}$ voxel, $\rho_{e0,i}$ is the electron density of 50/50 breast tissue. The physical density of 50/50 breast tissue is 0.985 g/cm$^3$ Physical densities are calculated dynamically during the convergence process.

The scattering angle is defined by $R$ and $z_{j,k}$, the detector position, and the scattering center, respectively. The angle $\Delta\theta_R^{j,k}$ is calculated for each scattering center from the radial size of the detector bin as follows:

$$\Delta\theta_R^{j,k} = \arccos\left(\frac{l - z_{j,k}}{R + dR}\right) - \arccos\left(\frac{l - z_{j,k}}{R}\right) \tag{4.5}$$

where $l$-$z_{j,k}$ is the length along the beam axis from scatter point ($j$, $k$) to the forward detector plane, and $R$ defines the inner radius of the detector ring location.

3. In addition to the aforementioned dependencies, the number of photons scattered into bin (R, K) is dependent on the spectral distribution of the incident beam. This is because the incident and scattered photon energies for Compton and coherent cross sections are correlated. Typically this correlation is described using kinematic equations. As the correlations are different for each cross section, they will be presented in the next section. It is sufficient to introduce a parameter $N_0^{j,k}(K_0)$ here. This parameter effectively states the number of photons of energy $K_0$ that are available to scatter into (R, K).

4. The total number $N_{tot}(R,K)$ of photons scattering into (R, K) is given by the product of the number of available incident primary photons of correct energy, the probability of scatter into bin (R, K), and the scattered photon attenuation factor:

$$N_{tot}(R,K) = \sum_{i=K_{0i}}^{K_{0f}} \sum_{j=1}^{n} \sum_{k=1}^{m} N_{scat}(i,j,k,R) \times \exp\left[ -\left( \frac{\mu_{bt}}{\rho} \right)_i \rho_{bt} \sqrt{(l_{j,k} - z_{j,k} - 2)^2 + R^2} \right] \tag{4.6}$$

where $K_{0i}$ is the lower bound energy of incident spectrum, $K_{0f}$ is the upper bound energy, $n$ is number of voxels, $m$ is the number of scattering centers per voxel, $\left( \frac{\mu_{bt}}{\rho} \right)_i$ is the mass-attenuation coefficient of normal breast tissue at energy $i$, $\rho_{bt}$ is the density of 50/50 breast tissue, and $\sqrt{(l_{j,k} - z_{j,k} - 2)^2 + R^2}$ is the distance traveled by the scattered photon in breast tissue from the scattering point to the lower slab boundary.

The factor $N_{scat}(i,j,k,R)$ is the number of photons scattering inside the subvoxel of length $\Delta z$ belonging to scattering center $k$ of voxel $j$ into (R, K). The number of photons reaching the top of this segment is $N_0^{j,k}(K_0)$. If the total linear cross section in $\Delta z$ is given as $\mu^{j,k}$, the number of primary photons reaching the bottom of the subvoxel is:

$$N_0^{j,k+1}(K_0) = N_0^{j,k}(K_0) * \exp(-\mu^j \Delta z) \tag{4.7}$$

The number of photons which interacted in the subvoxel is:

$$N_{\text{int}}^{j,k} = N_0^{j,k}(K_0) - N_0^{j,k+1}(K_0) = N_0^{j,k}(K_0)\left(1 - \exp(-\mu^j \Delta z\right) \tag{4.8}$$

Finally, the number of photons scattering in the direction of bin (R, K) is:

$$N_{scat}(i,j,k,R) = N_{\text{int}}^{j,k} \frac{\Delta\sigma_{R,E}^{j,k}}{\mu^j} = N_0^{j,k}(i)\left(1 - \exp(-\mu^j \Delta z\right)\frac{\Delta\sigma_{R,E}^{j,k}}{\mu^j} \tag{4.9}$$

where $\frac{\Delta\sigma_{R,E}^{j,k}}{\mu^j}$ is fraction of ALL scatter interactions in the subvoxel which are scattered into bin (R, K), and may be defined as:

$$\Delta\sigma_{R,E}^{j,k} = \left(\Delta\sigma_{R,E}^{j,k}\right)_{comp} + \left(\Delta\sigma_{R,E}^{j,k}\right)_{coh} \tag{4.10}$$

where $\left(\Delta\sigma_{R,E}^{j,k}\right)_{comp}$ and $\left(\Delta\sigma_{R,E}^{j,k}\right)_{coh}$ are the Compton and coherent cross sections per unit volume, respectively. The derivation of the coherent, Compton Klein-Nishina, and Compton Doppler broadened cross sections is presented in section 4.6.

The factor $\left(1-\exp(-\mu^j \Delta z\right)$ is computationally intensive to calculate for large arrays due to the presence of the exponential. The following approximation can be made* when $\Delta z << 1/\mu^j$, which is satisfied when $x$=0.25 cm:

$$\left[1-\exp\left(-\mu^j \Delta z\right)\right] \approx \mu^j \Delta z \tag{4.11}$$

and this is the approximation we use in the algorithm.†

5. The derivation of the backscatter space is similar, with the geometric variables modified for backscatter geometry.

## 4.5 Calculation of $N_0(K_0)$

This section deals with deriving the general formula for the number of photons of energies between $K_0$ and $K_0+\Delta K_0$, which we designate $N_0(K_0)$. We need to calculate the percentage of total incident photons which fit into the energy range ($K_0$, $K_0+\Delta K_0$). This value multiplied by $N_0$ will yield the total number of *incident* photons $N_0(K_0, K_0+\Delta K_0)$ neglecting attenuation. A typical spectrum used in this project is shown in Figure 4.4, where $K_i = K_0$ and $K_f = K_0 + \Delta K_0$.

---

* $e^x \cong 1+x$ for small $x$

† This approximation substantially improves computation time by removing the inefficient exponential operation.

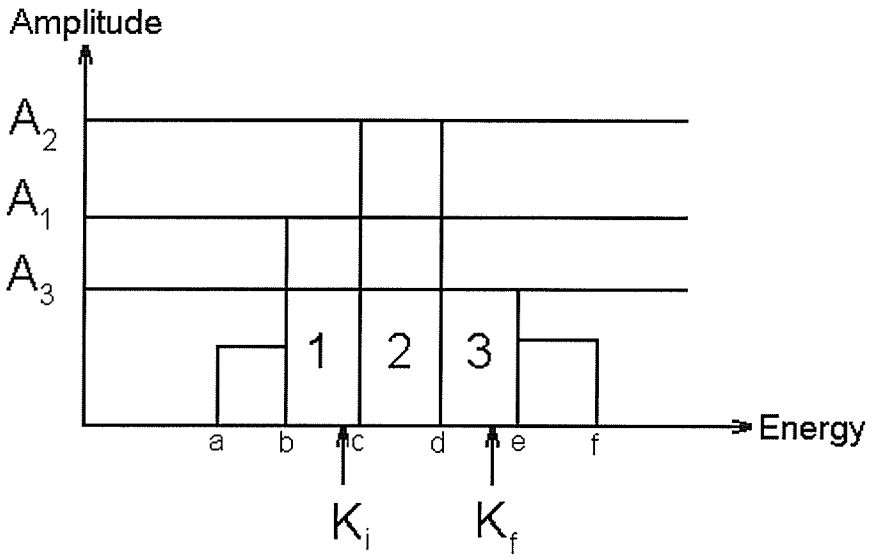


Figure 4.4: Diagram for calculation of the average number of photons occurring between energies $K_i$ and $K_f$.

Given that the spectrum is normalized to 1, we wish to calculate the fraction of photons $f$ falling between $K_i$ and $K_f$. The calculation is performed using the simple linear interpolation*:

$$f = \frac{K_c - K_i}{K_c - K_b} f_1 + f_2 + \frac{K_f - K_d}{K_e - K_d} f_3 \qquad (4.12)$$

where, $f_1, f_2$, and $f_3$ are the fractions of photons in bins 1,2, and 3, respectively. The number of photons of correct incident energy is:

* Analytic integration or Lagrange interpolation could be substituted for this formula, however as a small number of bins was involved (< 3), this method requires less computational time.

$$N_0(K_0) = f \times N_0 \tag{4.13}$$

where $N_0$ is the total number of incident photons.

## 4.6 Calculation of Cross Sections in a Discrete Geometry

### 4.6.1 Coherent Scattering Cross Section

The discrete calculation of the coherent cross section, in $cm^2$ per unit volume per steradian per unit volume, takes the form:

$$\left(\Delta\sigma_{R,K}^{j,k}\right)_{coh} = \sum_{i=A} \rho_i \frac{r_0^2}{2}(1+\cos^2\theta_R^{j,k})F^2\left[x, \rho_e(j,k,R)\right]\Delta\Omega_R^{j,k} \tag{4.14}$$

where $\rho_i$ is the number of atoms of element $i$ per unit volume, and the summation occurs over all elements present in the volume. The formula is composed of two major components. $\left(\frac{\Delta\sigma_{R,K}^{j,k}}{\Delta\Omega_R^{j,k}}\right)_T = \frac{r_0^2}{2}(1+\cos^2\theta_R^{j,k})$ is the Thomson differential cross section in units of $cm^2$ per steradian per electron, and $F\left[x, \rho_e(j,k,R)\right]$ is the unitless form factor. The variable $x$ is defined as

$$x = \frac{m_e c}{hc} K_0 \sin \frac{\theta_R^{j,k}}{2} \tag{4.15}$$

where *hc* is Planck's constant multiplied by the speed of light. All other factors have been previously defined. Calculation of coherent scatter into *(R,K)* is simplified by the fact that the scattered photon energies are identical to the initial energies. The boundary values (*K, K+ΔK*) are used in Equation 4.12 of section 4.5.

### 4.6.2 Klein-Nishina Compton Cross Section

The partial Klein-Nishina cross-section $\Delta\sigma_{R,K}^{j,k}$ predicts the probability of an interaction producing a scattered photon with scattering angle $\Delta\theta_R^{j,k}$ (see Figure 4.3), per unit angle and per unit volume, and is dependent on the position of *j* and *k* the radius *R*, and the energy *K*:

$$\left(\Delta\sigma_{R,K}^{j,k}\right)_{comp} = \rho_e \frac{r_o^{\,2}}{2}\left(\frac{K}{(K_0)_{R,K}^{j,k}}\right)^2\left[\frac{K}{(K_0)_{R,K}^{j,k}} + \frac{(K_0)_{R,K}^{j,k}}{K} - \sin^2(\theta_R^{j,k})\right]\times$$
$$\left(2\pi \sin(\theta_R^{j,k})\right)\Delta\theta_R^{j,k} \tag{4.16}$$

where $\rho_e$ is the electron density per unit volume, $r_o$ is the classical electron radius, $(K_0)_{R,K}^{j,k}$ is the incident photon energy calculated using $K, \theta_{j,k}$ and Compton kinematics and $\Delta\theta_R^{j,k}$ is the angular range subtended by $R$ and $R+dR$ at the point $(j,k)$.

As a consequence of the kinematics of Klein-Nishina physics, only a fraction of incident primary photons are allowed to scatter from scattering center $k$ and incident energy boundaries ($K_0$, $K_0+\Delta K_0$) through an angle $\theta_R^{j,k}$ into bin $(R, K)$. The energy of a Compton scattered photon $K$ is related to the incident photon energy $(K_0)_{R,K}^{j,k}$ and the scattering angle $\theta_R^{j,k}$ via the following equation:

$$(K_0)_{R,E}^{j,k} = \frac{1}{\frac{1}{K} + \left(\cos\theta_R^{j,k} - 1\right)} \tag{4.17}$$

Calculation of the incident energy boundaries required in section 4.5 can be obtained using this equation.

### 4.6.3 Doppler Broadened Compton Cross Section

Unlike previous cross section calculations, the discrete Doppler broadened Compton cross section into (R, K) can not be calculated using the method of section 4.5.

With Doppler broadening, a photon with any incident energy is eligible for scatter into (R, K) with a probability defined indirectly by Equation 3.4. The CCSR calculation of the total Doppler Broadened Cross section is based on calculating the cross sections for all combinations of incident and scattered energies, and is expressed per unit angle per unit volume by the following formula:

$$\left(\Delta\sigma_{R,E}^{j,k}\right)_{comp} = \rho_e \sum_{E_0=K_i}^{K_f} N_0^{j,k}(K_0, K_0+\Delta K_0)\Delta\theta_R^{j,k} \times \frac{r_0^2 K}{2K_0 q(K_0,K,\theta_R^{j,k})\left(1+p_z^2(K_0,K,\theta_R^{j,k})\right)^{1/2}} \times X(K_0,K,\theta_R^{j,k})J(p_z(K_0,K,\theta_R^{j,k})) \tag{4.18}$$

where $N_0^{j,k}(K_0, K_0+\Delta K_0)$, $j$, $k$, and $\Delta\theta_R^{j,k}$ are defined above. The summation resolution we have used for all cases is 20 eV, which we have found to be sufficient to approximate a continuous integration while still retaining a reasonable computation time. The discrete value of $q$ is:

$$q = \sqrt{K_0^2 + K^2 - 2K_0 K\cos\theta_R^{j,k}} \tag{4.19}$$

while $p_z$ is:

$$p_z = \frac{\vec{p}\cdot\vec{q}}{q} = \frac{K_0 K(1-\cos\theta_R^{j,k}) - K_0 + K}{q(K_0,K,\theta_R^{j,k})} \tag{4.20}$$

$X$ is defined as in section 3.3.2:

$$X = \frac{R}{R'} + \frac{R'}{R} + 2\left(\frac{1}{R} - \frac{1}{R'}\right) + \left(\frac{1}{R} - \frac{1}{R'}\right)^2 \tag{4.21}$$

where the discrete values of $R$ and $R'$ are:

$$R = K_0\left(\sqrt{1 + p_z^2(K_0, K, \theta_R^{j,k})} + \frac{K_0 - K\cos\theta_R^{j,k}}{q(K_0, K, \theta_R^{j,k})} p_z(K_0, K, \theta_R^{j,k})\right) \tag{4.22}$$

and

$$R' = R - K_0 K(1 - \cos\theta_R^{j,k}) \tag{4.23}$$

and $J(p_z)$ is the Compton profile for the electron, which represent the effects of atomic binding. Tabular values of $J(p_z)$ for the elements H, C, N, O, P, and Ca were obtained from Biggs[109].

# 5

## Data Acquisition and Algorithm Design

## 5.1 EGSnrc Data Acquisitions and Post Processing

As discussed in section 2.5, we have used the EGSnrc Monte Carlo package to simulate both CT and mammographic imaging systems. For our CT experiments in Chapter 6 we have simulated a cylindrical phantom, and we have modified the DOSRZNRC user code to allow us to output scatter distributions in a data file. We have simulated non-cylindrical phantoms in our mammographic experiments of Chapter 7, and for this purpose we have used the Cartesian greater user code, DOSXYZNRC.

Both user codes have been modified to output the same format data file, including headers containing all relevant simulation parameters. Each first order scatter distribution is stored in its own array, while all second order and higher scatter distributions, regardless of type, are stored in their respective arrays. Separate arrays are used for forward scattered and back scattered photons. A PERL script is used to modify the output data into a format readable in MATLAB.

## 5.2 Algorithm Design in MATLAB

We coded two major functions in MATLAB. The first function is primarily dedicated to parameter initialization and loading of relevant data files. The second function is dedicated to evaluation of the objective function, accepting the current distribution of electron density as input.

MATLAB is optimized for array operations. Despite being a high level programming language, we have found little improvement in computational speed when compiling the code into C++ using the compilation toolbox provided from MathWorks, noticing a speed gain of only approximately 5%. To help improve the computational speed, the algorithm has been vectorized to the maximum extent possible in MATLAB.

With the exception of the simulated annealing code, native MATLAB optimization algorithms were used. For simulated annealing, we used the ASAMIN MATLAB code*.

A Graphical User Interface (GUI) has been constructed for monitoring of output. After each iteration, several plots are displayed, including the old and new electron density distributions, simulated and predicted scatter distributions, and associated residues.

* http://www.econ.ubc.ca/ssakata/public_html/software

## 5.3 Optimization Algorithms

The reconstruction of the image is an iterative process of optimization, which involves the minimization of an objective function *f(x)*. The formula for the objective function is as follows:

$$f(x) = \sum_{K=K_i}^{K_f} \sum_{r=r_i}^{r_f} F(r,K)^2 \tag{5.1}$$

where $x$ is the input vector representing the influence of the voxel electron densities on the scattered photon distribution. The function $F(r,K)$ is defined as:

$$\vec{F}(\vec{r},\vec{E}) = \vec{S}(\vec{r},\vec{K}) - \vec{P}(\vec{r},\vec{K}) \tag{5.2}$$

$\vec{S}(\vec{r},\vec{K})$ and $\vec{P}(\vec{r},\vec{K})$ represent the simulated Monte Carlo results and predicted data spaces, respectively. The least squares difference is obtained for each element and summed over the whole data space from $K_i$ to $K_f$ and $r_i$ to $r_f$.

There is a large selection of optimization algorithms which can be used to optimize *f(x)*. Three major classes of optimization algorithms were tested, and are presented in the following sub-sections.

### 5.3.1 Trust Region

This form of optimization is based upon approximating the objective function in a limited neighborhood, called a trust region.[110] The objective function inside the trust region is approximated by a polynomial, typically the first two terms of the Taylor approximation of $f(x)$ at $x$, which lead to a spheroid or ellipsoid space. If minima are found inside the trust region, the trust region is considered to be an accurate representation of the local objective function $f(x)$. The current search point is then moved to the new minima and the trust region is expanded. Finally, when no improvement is found inside the trust region, the trust region is contracted in an attempt to better approximate the local objective function. Contractions continue until either a new promising search direction arises, or the function converges. If a new direction arises, the search point is moved to the new minima, and the trust region is expanded again.

### 5.3.2 Simulated Annealing

Simulated annealing[111] is an optimization algorithm that is inspired by the way a metal cools and freezes into a minimum energy crystalline structure. The atoms in the metal 'bounce' around, and randomly wander through states of various energy. As the temperature is gradually reduced, the atoms find appropriate states of minimum energy, though they may still occasionally explore higher energy states during the cooling.

Similarly, the algorithm strives to find the global minimum in a multi-dimensional problem by allowing a great deal of random direction at first, even if the direction sometimes leads to a higher value of the objective function *f(x)*. As the algorithmic 'temperature' is reduced, the search direction gradually becomes one of descent, where unfavorable directions (higher *f(x)*) are less tolerated. The major advantage of simulated annealing over other techniques is its ability to avoid becoming trapped in local minima, though there is a large computational cost associated with the algorithm.

We tested ASAMIN, a third-party simulated annealing code for MATLAB. We found the algorithm was robust in achieving a good solution (<1% error) using a variety of starting points, with little (<1%) difference between converged solutions. We have found this algorithm to be effective in locating minima in our objective function. However, in the latter stages of the project, we have been improving the resolution in the z-axis of our imaging system. As such, we introduce a continuously increasing number of dimensions in the optimization function. The computational requirements were prohibitive for the highest resolution we used. With 32 imaging voxels, the time required to search the solution space for a global minimum was prohibitive (several thousand evaluations over several days), prompting the search for a faster optimization method.

### 5.3.3 Gradient Methods

Algorithms that fall under this category include steepest descent, Gauss-Newton,[110, 112] and Levenberg-Marquardt[113] methods. The simplest of these methods is the steepest descent. For each iteration, the search direction is calculated as the negative of the gradient vector $\nabla f(x)$. The length of the iterative line step is chosen to minimize the objective function *f(x)* along the line. An unfavorable characteristic of this approach is that the search steps tend to zigzag towards the final solution. The method is computationally inefficient when, for example, the function to be minimized contains long narrow valleys. The Gauss-Newton algorithm is more sophisticated than steepest descent, and calculates search directions based on the solution of a linear system of equations containing the Jacobian *J(x)* of the input vector *x*. The Levenberg-Marquardt algorithm is a hybrid of Gauss-Newton and steepest descent in that the calculated search direction is a cross between the Gauss-Newton and steepest descent search directions.

While gradient algorithms are more prone to falling into local minima than algorithms such as simulated annealing, they do function with an objective function that can be discontinuous in its first and second derivatives. As the first derivative of the objective function produced by our algorithm is discontinuous and the Gauss-Newton function is computationally more efficient than simulated annealing or trust region, we have selected the Gauss-Newton optimization method for the final version of our algorithm. A Gauss-Newton algorithm is

generally more efficient than a Levengerg-Marquardt algorithm when the residual is at zero. However, using an efficient algorithm such the Gauss-Newton method, the problem of converging to local minima must be addressed.

### 5.3.4 Strategies for Avoiding Local Minima

We observed that all the gradient method algorithms we used were prone to falling into local minima far from the correct solution, and we employed several strategies to minimize this problem.

**1. Primary photon constraint**

To include the primary photon count as a new constraint on our solution, we introduce a new residue:

$$g(x) = (N_S - N_P)^2, \tag{5.3}$$

where $N_S$ is the number of simulated primaries, and $N_P$ is the number of predicted primaries. The simplest case of incorporating $g(x)$ into our objective function is through addition:

$$h(x) = Ag(x) + f(x) \tag{5.4}$$

Care needs to be taken in selecting the constant $A$, as the introduction of this constraint complicates the solution space. That is, if the first term of the equation dominates then the algorithm might converge on incorrect solutions which minimize the first term but not the second, effectively creating new local minima where none existed before. Figure 5.1 illustrates one example. The original objective function $f(x)$ is shown in black. The dashed line shows example alterations that could occur due to the introduction of the primary constraint (and have been observed in practice). When $g(x)$ is introduced, a local minimum on the left side is eliminated by the new constraint term. However, a new local minimum has appeared on the right side of the figure, where $g(x)$ is minimized despite a large $f(x)$. Consequently, if a starting point of large $x$ is chosen in this example, convergence may occur in the local minima where it would have correctly identified the global minima beforehand. Thus, care is warranted in selecting $A$ and the parameters of the minimization function.

In a noiseless environment, $g(x)$ would not be necessary as we have established that a global minimum exists and corresponds to the correct solution (Appendix B). However, the contribution of certain voxels can be very small, and could lead to large variations in electron density as the algorithm attempts a fit to a noisy data space. However, these variations are heavily penalized by $g(x)$, and are thus eliminated. These local minima are the sort that we aim to eliminate through the use of $g(x)$. We have experimented with the value of $A$, and have found that a value of $A = 3 \times 10^{-5} \times N_0$ allows superior convergence of the

algorithm compared to before, where $N_0$ is the number of incident primary photons. However, further investigation is required to test the optimal value of this parameter.

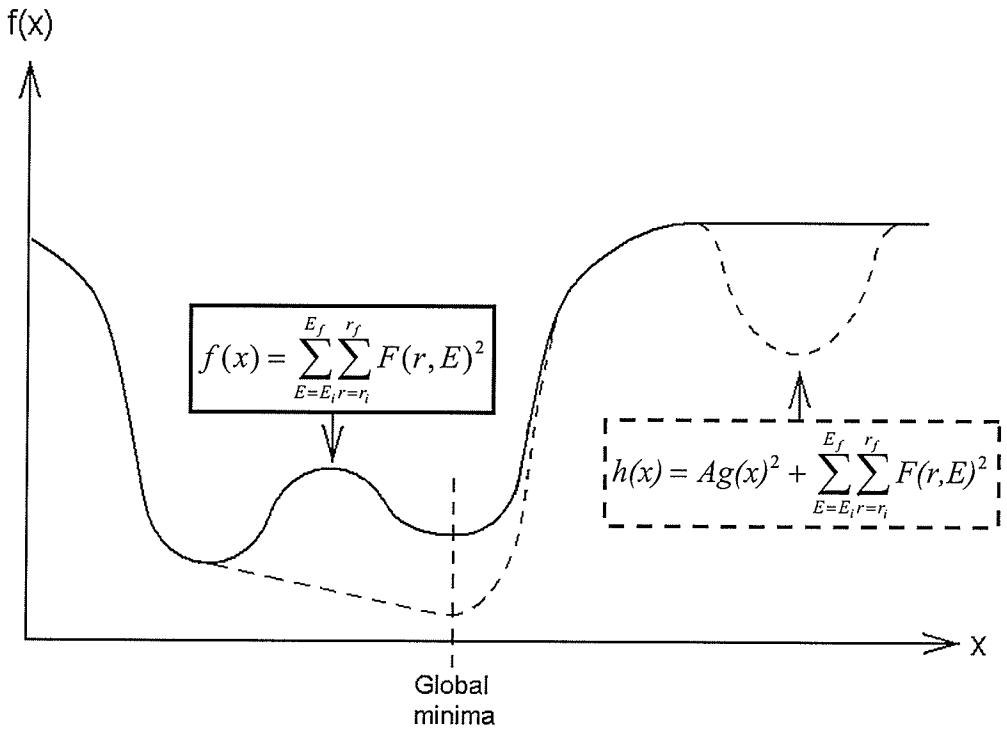


Figure 5.1: Effect of primary constraint on the objective function $f(x)$ for arbitrary $x$. The solid line represents the initial objective function. The dashed line represents the modified objective function showing the effects of introducing a primary constraint, including the elimination (left) and introduction (right) of local minima.

## 2. Grid Refinement A

When an optimization problem contains large numbers of variables*, one approach is to solve the problem using a smaller number of variables. The solution to the lower order problem is then interpolated and used as a starting point for higher order problems. We have employed this approach here, by starting our imaging process by using 1 cm voxels. The resulting image is then interpolated to a 0.5 cm voxel resolution and the process is repeated. Finally, an image with a 0.25 cm resolution is produced. Consider imaging a 5 cm thick segment of breast tissue voxels where a lesion has been placed at 5-5.25 cm. Figure 5.2 shows the converged electron density distributions in cases where the grid refinement algorithm is applied. In panel (a), the phantom is imaged using no grid refinement technique. In this case, the optimization process appears to have encountered a local minimum as the converged solution is far from the expected solution. Two lesions were imaged, both false negatives as they are not at the location of the actual lesion. Panels (b)-(d) illustrate the progression of the grid refinement technique. As the resolution is progressively increase, the contrast of the imaged lesion (a true positive) increases with respect to the surrounding breast tissue. At the highest resolution, the electron density of the lesion voxel is 100.6% of the expected electron density.

* Each voxel is considered as a separate variable.

### 3. Grid Refinement B

We also tested a second grid refinement approach devised from an analysis of each individual voxel contribution to each single forward and back scattered photon distribution. Figure 5.3 shows an analysis of the photon contribution to both detectors as a function of voxel position for a homogenous breast tissue phantom of thickness 5 cm. We note in this case that the voxel closest to the backscatter detector has the largest contribution. A gradient-based optimization algorithm will tend to optimize the electron density value of this voxel before other voxels with lower gradients. As a result, the converged value for this dominant voxel will likely be more accurate than other voxels, and less prone to local minima. In Chapter 6, we discuss using a weighting method to take this effect into account. In Chapter 7, we introduce a modification to improve results.

Implementation of grid refinement B involves the following series of steps. First, by converging in the parameter space that includes all voxels, a solution is found. Following this, the voxel value with the highest photon contribution is made constant, and solution reconvergence is repeated using the previous image as a starting point. That can be visualized by removing a dimension from the voxel parameter space that corresponds to the fixed voxel value. Figure 5.4 illustrates the improvement this technique brings when the phantom described in the previous section is imaged. Panel (a) illustrates the

results with no grid refinement enhancement, while panel (b) shows significant improvement when the technique is used.

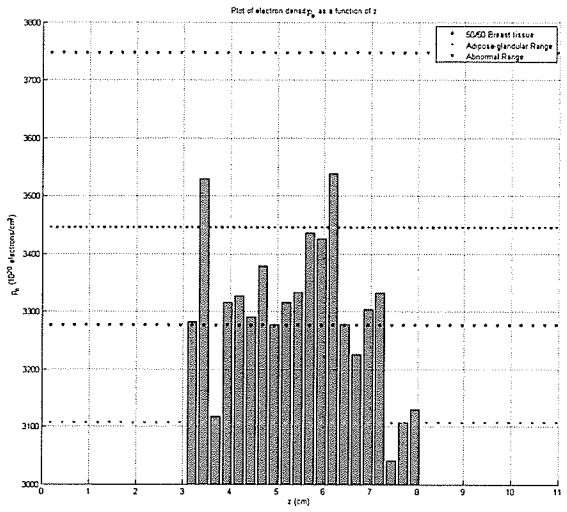


(a)

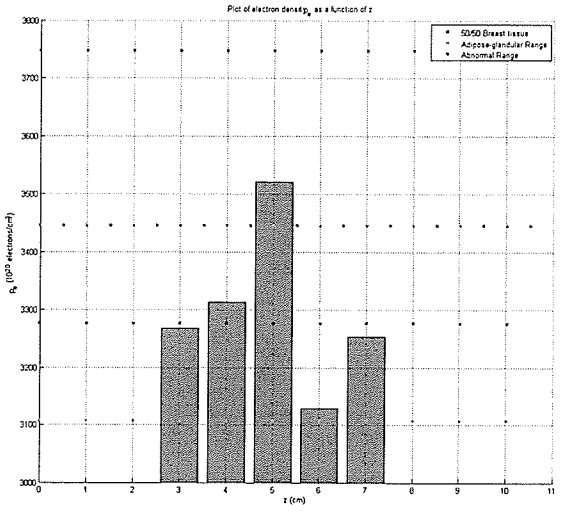


(b)

Figure 5.2: (a) Converged electron density distribution when no grid refinement technique is applied. Two false positives have occurred, neither indicating the location of the lesion. (b) First stage of the grid refinement approach. (1 cm resolution) A true positive occurs at the location of the calcification. (continued)

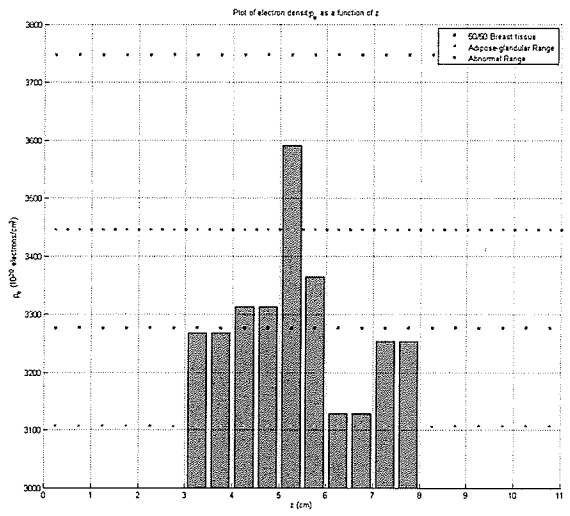


(c)

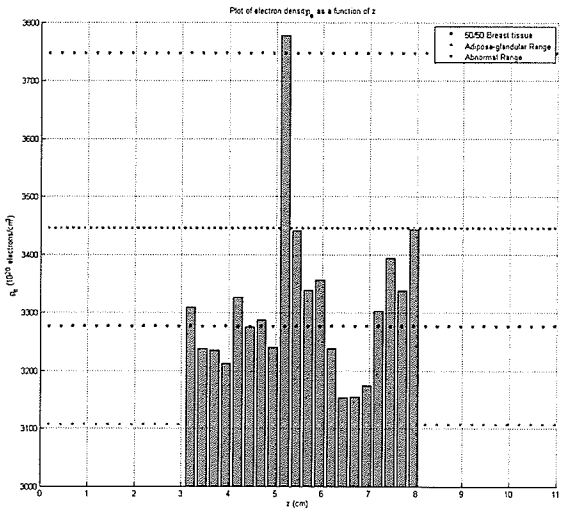


(d)

Figure 5.2: (continued) (c) Second stage of the grid refinement approach. (0.5 cm resolution) The true positive value is approximately 96% of the electron density of the lesion (d) Final stage of the grid refinement approach. (0.25 cm resolution) The true positive is 100.6% the electron density of the lesion.

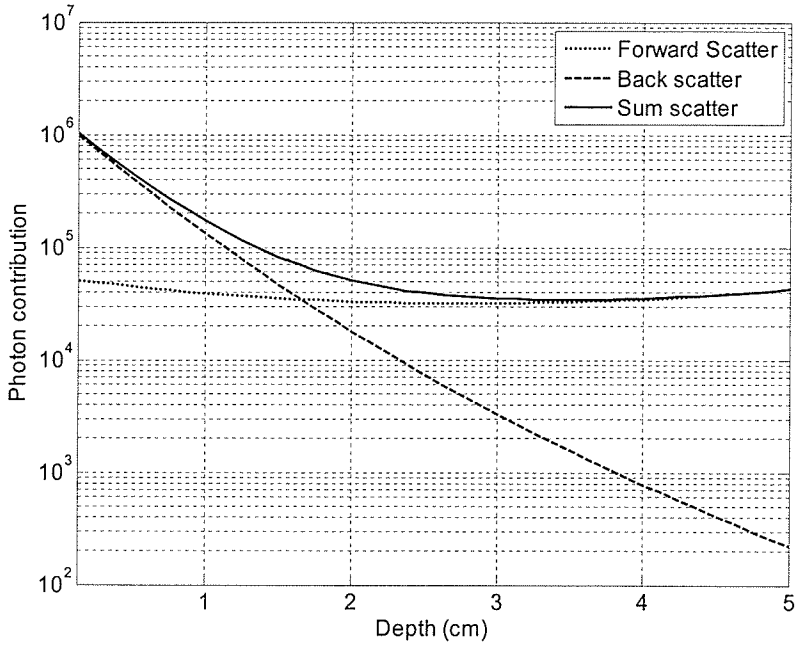


Figure 5.3: Integrated photon contributions to forward and rear detectors as a function of contributing voxel depth.

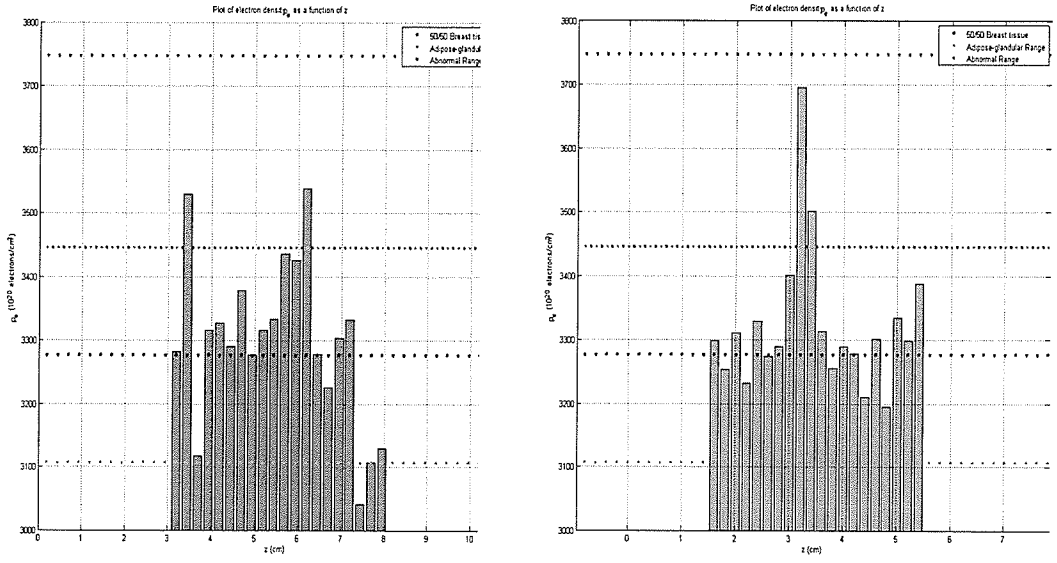

Figure 5.4: (a) Converged electron density distribution when no grid refinement technique is applied.(same as 5.3(a)). (b): Using grid refinement B technique, the lesion is detected, though a broadening is visible.

# 6

## Application to Compton CT

## 6.1 Introduction

In this chapter, we adapt the CCSR algorithm to the spectral and geometric conditions present in CT. That is, we simulate a beam with mean energy similar to CT, and a phantom which is representative of the uncompressed, thicker, breast imaged using CT.

In this proposal, CT image reconstruction involves processing both primary and scatter data to create two separate images of attenuation and electron density, respectively. The addition of an electron density image adds atomic information not otherwise present in the primary CT image. The major benefits to the inclusion of CCSR with breast CT include a reduction of dose due to the removal of any anti-scatter grids, increase in sensitivity due to the additional electron density image being produced, and atomic structure information being supplied that is not otherwise available in the CT image, which only reflects attenuation properties.

## 6.2 Materials and Methods

As mentioned in section 4.2, we chose to simulate a phantom cylinder of 8 cm thickness and 8 cm diameter, consisting of a homogenous mixture of 50/50 adipose-glandular breast tissue. Air gaps of thickness 2 cm were placed in front of and behind the cylinder, yielding a field of view (FOV) thickness of 12 cm ($l$=12 cm from Figure 4.1). Lesions were simulated by inserting simulated 0.5x0.5x0.5 $mm^3$ calcifications inside 1x1x2.5 $mm^3$ voxels of breast tissue.

Lesions were placed along the central z-axis with centers placed at 3.125 cm and 7.625 cm from the top of the phantom. PEGS (Preprocessor to EGS) material data files were created for 50/50 breast tissue using published elemental data.[114] Calcified breast tissue files were generated by combining 50/50 breast tissue and calcium hydroxyapatite ($Ca_{10}(PO_4)_6(OH)_2$) in a 0.95/0.05 ratio by weight.

### 6.2.1 Beam spectrum

We simulated a cylindrical 1 $mm^2$ non-diverging polyenergetic pencil beam of x rays perpendicularly incident on the cylinder and in line with the inhomogeneities. The optimal x ray energy for application of this approach to breast CT has not yet been established. However, it has been shown[115] that

KERMA* is at a minimum in the 50-70 keV energy range. For the purposes of this study an x ray photon spectrum produced by a 80 kVp electron beam, incident on a Tungsten target, and with 2 mm of Tungsten filtration was used.[1] The incident beam spectrum (Figure 6.1), which may be produced using a conventional Tungsten target/filter x ray tube, was chosen to minimize dose while maximizing electron density contrast.

Tungsten target and heavy Tungsten filtration produce the following characteristics in the spectrum:

1. The unfiltered bremsstrahlung spectrum is heavily attenuated at lower energies, due to the effects of beam hardening.
2. X ray energies slightly higher than the Tungsten K edge (69.4 keV) are heavily attenuated due to the discontinuous increase in x ray absorption at that energy. This effect is due to the fact that for energies lower than the K-edge, K shell electrons do not participate in the photoelectric effect due to insufficient energy to eject the electron, whereas for photon energies slightly higher than the K shell energy, the electrons are available to undergo the photoelectric effect. This creates a discontinuity in the attenuation curve. 2 mm of filtration has the effect in this case of almost completely removing spectrum components higher than the K edge.

* KERMA: Kinetic Energy released in material

3. There are 10 K shell x ray fluorescence energies in Tungsten between 65 keV and 70 keV (Attix[95], page 206). Using 500 eV binning, these photopeaks resolve as two peaks in the resulting spectrum.

The benefits include faster imaging time due to a narrow spectral range of detected photons* and the superior performance which has been demonstrated for quasi-monochromatic beams in a mammographic setting.[116]

### 6.2.2 Approximations

Several approximations have been made in the simulation and development of this algorithm for Compton CT. These include:

*1. Klein-Nishina approximation for the Compton scatter cross sections.* Computation time was a factor for the thicker uncompressed breast presented in this section. The implementation of Doppler broadening increases the algorithmic computational time by a factor of 10. We address the inclusion of doppler broadening in Chapter 7.

*2. No coherent scatter.* The photon backscatter, a valuable source of information, is predominantly Compton scatter, and thus a good approximation for the

* Imaging time is inversely proportional to spectral range.

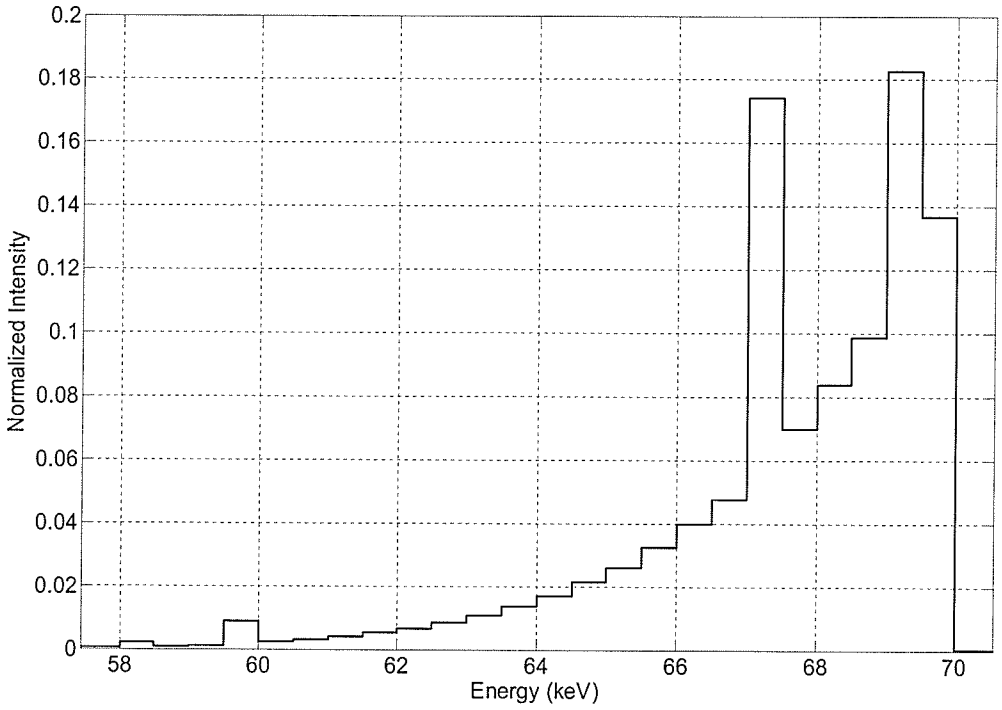


Figure 6.1: The incident beam spectrum for an 80 kVp electron beam impinging on a Tungsten target with 2 mm of Tungsten filtration.[1] Spectrum sampling resolution is 500 eV.

backscatter. Coherently scattered photons can provide an additional source of atomic information,[72, 99] but in this section we report on the application of our algorithm to Compton scatter imaging. Coherent scatter theory is implemented in Chapter 7.

*3. No multiple scatter.* The relatively homogenous nature of the breast, compared to, say, tissue containing bone or air, makes it possible to take advantage of a predictable multiple scatter background and use a subtraction technique to eliminate it. The application of this is addressed in Chapter 7.

*4. Constant mass attenuation coefficient throughout the simulated breast.* As a first approximation the mass attenuation coefficient of 50/50 breast tissue is used for all voxels. While valid when averaged over large regions of the breast, this approximation is invalid for small local areas such as in the vicinity of calcifications. The small size of the calcifications has however allowed this approximation to be implemented with minimal impact to the reconstructed image.

*5. Correct radiological path length of scattered photons known a priori.* For the purposes of determining attenuation from the scatter point to the detector, the correct post-scatter radiological path length for all photons is assumed to be known. The determination of the breast/air interface which may be obtained by CT reconstruction of the primary photons is critical to this assumption.

Two electron density distributions were imaged; the forward scatter data was used to generate the first distribution while the backscatter data were used to

generate the second distribution. The final electron density values were calculated from the forward- and back-scattered electron density distribution using the following equation:

$$\rho_e^j = \frac{w_f^j \rho_{e,f}^j + w_b^j \rho_{e,b}^j}{w_f^j + w_b^j} \tag{6.1}$$

where $\rho_{e,f}^j$ and $\rho_{e,b}^j$ are the electron density distributions calculated using the forward and back scatter, respectively*. The weights for the $j^{th}$ voxel were calculated using the following equations:

$$w_f^j = \frac{N_f^j}{N_f} \text{ and } w_b^j = \frac{N_b^j}{N_b} \tag{6.2}$$

where $N_f$ and $N_b$ are the total number of photons that strike the forward and backscatter detectors respectively, while $N_f^j$ and $N_b^j$ are the number of photons originating from voxel $j$ that strike the forward and backscatter detectors, respectively. The weighting factors are calculated based on the forward and back scattered electron density distributions after convergence. When the forward scattered and back scattered electron density distributions are combined, the distribution processed from forward scatter will have a higher weights for voxels on the distal side of the phantom while distribution processed from the backscatter

* Simultaneous optimization was considered and implemented in Chapter 7.

will having higher weight for voxels on the proximal side of the phantom. The final converged electron density distribution characterizes the phantom.

Three studies were performed to explore the dependence on dose as well as detector energy coverage. The first study used $10^8$ incident photons, a dose consistent with breast CT, while for the second study $10^7$ incident photons we used to investigate the effect of increasing statistical noise. The reduced dose associated with $10^7$ incident photons would allow CCSR to be combined with tomographic reconstruction using 10 projections. The final study also used $10^7$ photons while the radius of each detector was reduced to 10 cm, keeping the detector resolution the same. This allowed the effects of restricting our detector space to be evaluated.

Each study was repeated 5 times with different random number seeds in order to evaluate the uncertainty due to statistical noise while retaining the same geometry and calcification locations.

### 6.2.3 Production of Receiver Operating Characteristic (ROC) curves

To explore the suitability of CCSR in detecting calcifications in a phantom, we generated ROC curves to test the relative overlap between two converged electron density sets. These are the sets containing:

1) normal breast tissue voxels

2) calcified breast tissue voxels

Five separate simulations were performed per study, producing 10 electron density values associated with calcifications and 190 values associated with normal breast tissue. For each simulation, the location of both calcifications was randomized, to eliminate any possible positional bias.

An ROC analysis was performed on all five images, and the true positive fraction (TPF) was defined as the number of calcified electron density values higher than a threshold electron density value. Conversely, the false positive fraction (FPF) related to the number of calcified electron density values less than the threshold value. The ROC curve was generated using threshold values from 2.5 to 4.5 x $10^{23}$ electrons/$cm^3$.

## 6.3 Results

### 6.3.1 2D Scatter Distributions

The forward scattered and back scattered detector data for the polyenergetic beam are shown in Figure 6.2. These detector spaces represent the solutions of Equation 4.6 for all $R$ and $K$ with the converged simulation electron density and attenuation values. The data space range shown in Figure 6.3 contains

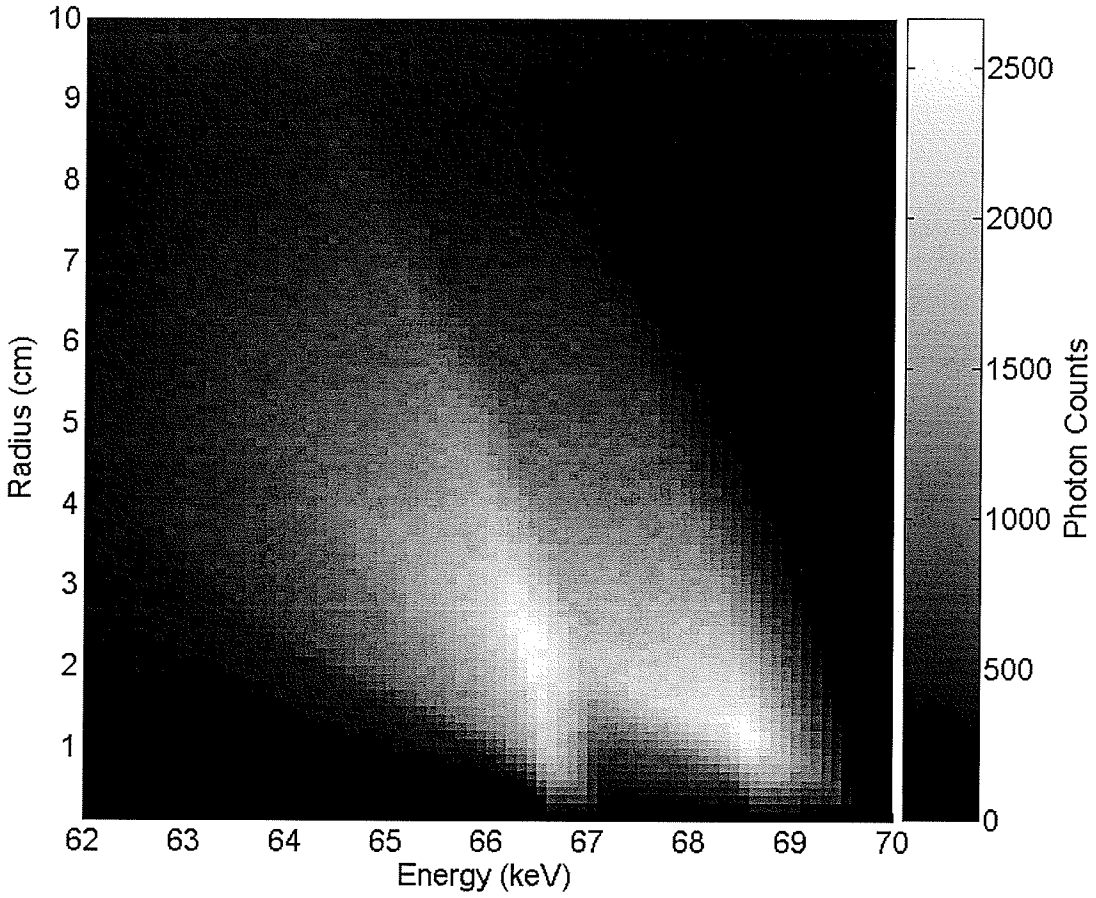


Figure 6.2: The forward scattered photon distribution resulting from a polyenergetic beam incident on an 8 cm thick breast phantom containing inhomogeneities. Note the two fan-shaped distributions, resulting from the two fluorescent peaks in the incident spectrum.

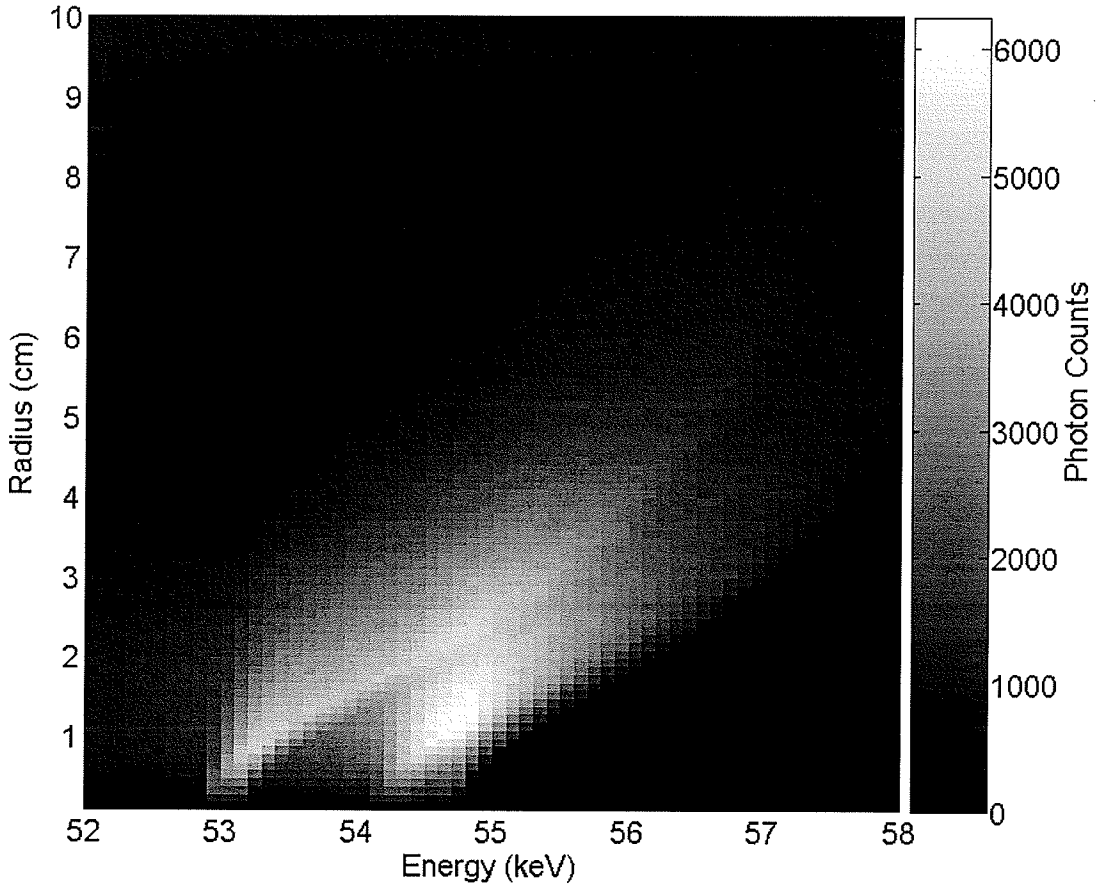


Figure 6.3: The back scattered photon distribution resulting from a polyenergetic beam incident on an 8 cm thick breast phantom with calcification inhomogeneities. Note the two fan-shaped distributions, resulting from the two fluorescent peaks in the incident spectrum.

81% of all detected forward scattered photons, while the data space shown in Figure 6.4 contains 82% of all detected backscattered photons. The forward scattered data set for all data points in the 63.0-68.0 keV energy range and the back scattered data set for all data points in the 53.0-58.0 keV energy range were used in all studies. Radial ranges were 0-20 cm for the first two studies and 0-10 cm for the third study.

### 6.3.2 Convergence Results

Figure 6.4(a) shows 1D images of the phantom (I), initial estimate (II), and converged electron density values for all 3 studies (III-V), each displayed as a column of arbitrary width. Figure 6.4(b) shows electron density histograms for cases labeled (III)-(V). Image (I) shows a 1D cross section of the phantom material in the field of view defined in Figure 4.1. Predicted electron density of normal breast tissue is $3.28 \times 10^{23}$ e/cm$^3$. Predicted electron density of lesions is $3.59 \times 10^{23}$ e/cm$^3$. This phantom was used for all studies. Image (II) shows the iterative starting point of the algorithm, where all voxels in the 1D voxel line were assigned values of normal breast tissue.

Figure 6.5 is a plot of photon count vs. radius for a single 500 eV energy slice representing energies 57-57.5 keV, calculated for the first study using the iterative starting point shown in Figure 6.4(a). The experimental EGSnrc simulation data is shown as well as the pre- and post-convergence predicted

distributions. The reconstructed images shown in Figure 6.4 have been obtained from a single reconstruction, as would be the case in a typical imaging scenario.

Image (III) of Figure 6.4 shows the converged electron density distribution for $10^8$ photons. Average voxel dose reported by EGSnrc was 3 mGy. The average standard deviation obtained from 5 trials was 27 x $10^{20}$ electrons per voxel, while the average imaged electron densities deviated from actual values by 16 x $10^{20}$ electrons per voxel, corresponding to an average deviation of 0.49% from the phantom values. No electron density broadening occurs around the imaged inhomogeneities; however the reconstructed values of the two inhomogeneous voxels are systematically below the expected values by 2.2% and 1.9%. (Table 6.1)

If this algorithm were to be used in conjunction with a CT reconstruction technique a number of projections would be required and therefore the second study was performed using the same data subspace while using $10^7$ primary photons, corresponding to an average voxel dose of 0.3 mGy (allowing 10 projections). For this lower dose study, the converged electron density distribution is shown in image (IV). As expected with a 10-fold reduction in the number of detected photons, the average standard deviation increases to 62 x $10^{20}$ electrons per voxel, while the mean electron density of the imaged voxels deviates from expected by 15.1 x $10^{20}$ electrons per voxel, corresponding to a variation of 0.46% from expected values. The reconstructed values of the two inhomogeneous voxels are now 4.2% and 3.7% lower than expected.

In the third study, the number of photons contained in the 10 cm radius limited detector space account for 91% of all scattered photons in the larger 0-20 cm radial range.

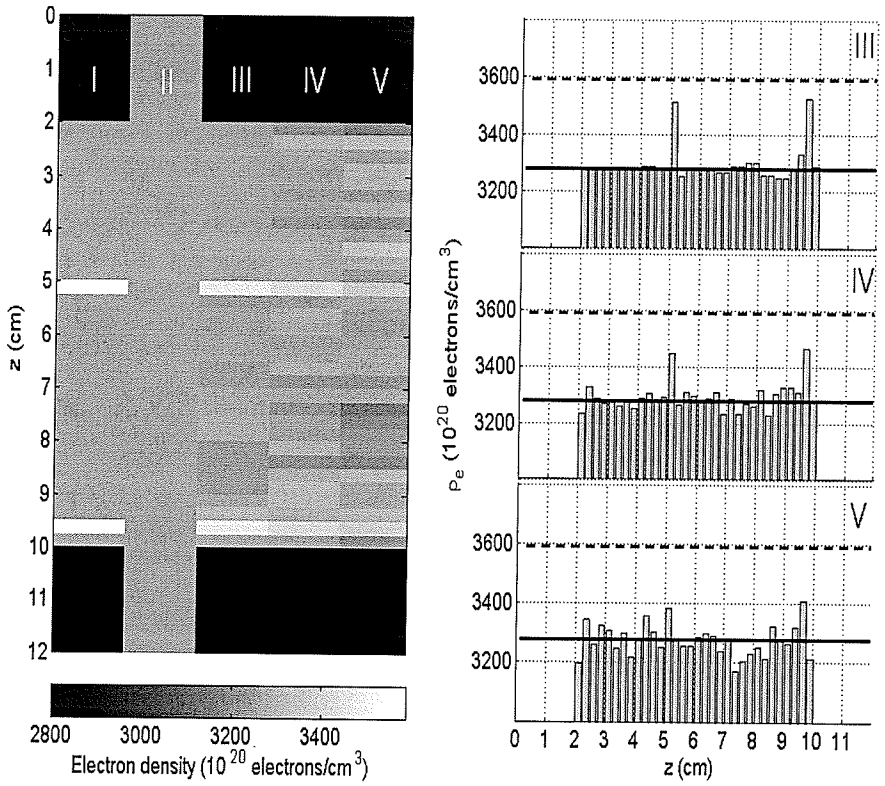


(a) (b)

Figure 6.4: (a) Grayscale 1D electron density images. (I) the simulated phantom, (II) the iterative starting point of the algorithm, (III) the reconstruction of the first study corresponding to $10^8$ photons, (IV) the reconstruction of the second study corresponding to $10^7$ photons, (V) the reconstruction of the third study corresponding to $10^7$ photons and a limited radial subspace of 0-10 cm. (b) Histograms of electron density values for the resulting images (III)-(V). The solid horizontal line refers to the electron density of 50/50 breast tissue while the dashed horizontal line refers to the electron density of calcified tissue.

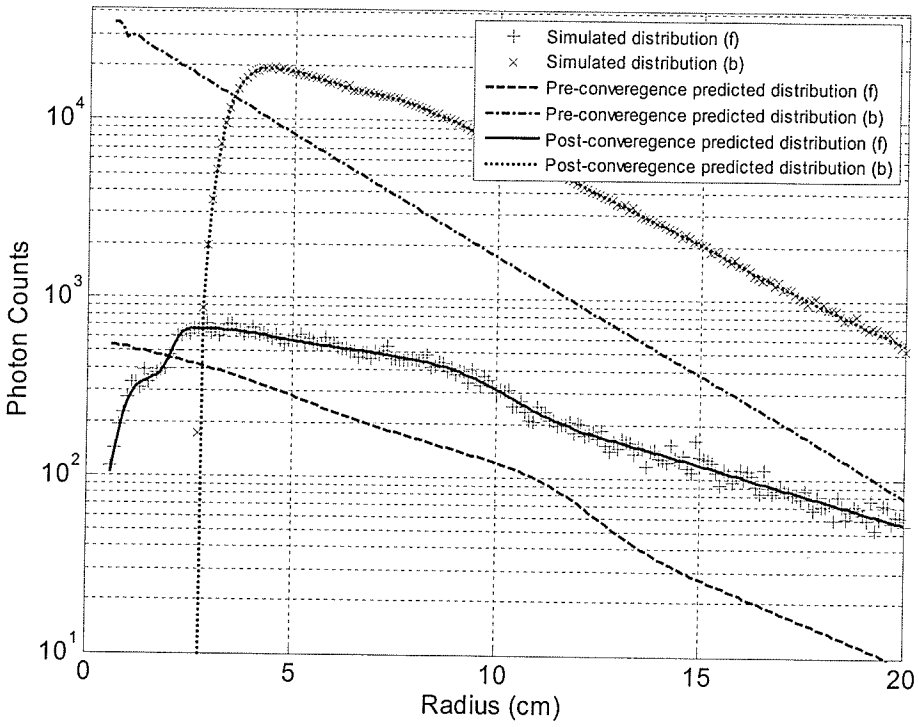


Figure 6.5: A 500 eV energy slice of the data space of energy range 57-57.5 keV. The simulated distributions represent the experimental simulated data while the predicted curves correspond to the calculated distributions using the iterative starting point (pre-convergence) and after converging (post-convergence). The labels (f) and (b) refer to forward- and back-scattered data, respectively.

The results are shown in Figure 6.4, Image (V). The full width at half maximum of the lesion peaks corresponded to approximately 0.5 cm. The statistical error was 82 x $10^{20}$ electrons per voxel while imaged voxels deviate from expected by 56 x $10^{20}$ electrons per voxel, or 1.7%. The electron density values are 6.2% and 5.0% lower than expected, and the difference in peak electron densities of the first inhomogeneity (3361 e/cm$^3$ at 5.5-5.25 cm) is less than 1%, potentially a false positive error.

For all studies the converged electron density of both inhomogeneities is reported in Table 6.1. Percentage differences are calculated relative to calcified tissue and normal breast tissue electron densities and vary from -1.6% for the first study to -7.0% for the low dose, small detector study. The statistical uncertainty of the calcifications is shown in the final column and ranges from a low of 0.52% to 2.2%. In all studies the phantom boundary was resolved to 0.25 cm resolution, illustrating that CCSR is capable of performing 1D boundary delineation with a single projection.

The results from the ROC analysis (Figure 6.6) for study 1 ($A_z$=0.999) indicate a qualitatively[3] 'excellent' ability to resolve calcified tissue from normal breast tissue, as were the results of the second study ($A_Z$=0.996). While the electron density results of the third study deviated quite significantly from those that were expected and were clearly inferior to those obtained using the wider detector geometry it is still possible to detect the presence of the inhomogeneity, with the ROC analysis classifying this ($A_z$=0.961) in the 'very good' category.

Table 6.1: Converged electron density values of the calcified voxels relative to normal breast tissue ($3.360 \times 10^{23}$ e/cm$^3$) and calcified tissue ($3.586 \times 10^{23}$ e/cm$^3$). The fourth and fifth columns are the systematic error and statistical uncertainty, respectively.

| Study | Inhomogeneity | Measured electron density ($\times 10^{23}$ e/cm$^3$) | Difference from expected electron density (%) | Statistical uncertainty (%) |
|---|---|---|---|---|
| #1 | #1 | 3.51 | -2.2 | 0.52 |
| | #2 | 3.52 | -1.9 | 0.71 |
| #2 | #1 | 3.44 | -4.2 | 1.7 |
| | #2 | 3.46 | -3.7 | 1.5 |
| #3 | #1 | 3.38 | -6.2 | 2.6 |
| | #2 | 3.41 | -5.0 | 2.2 |

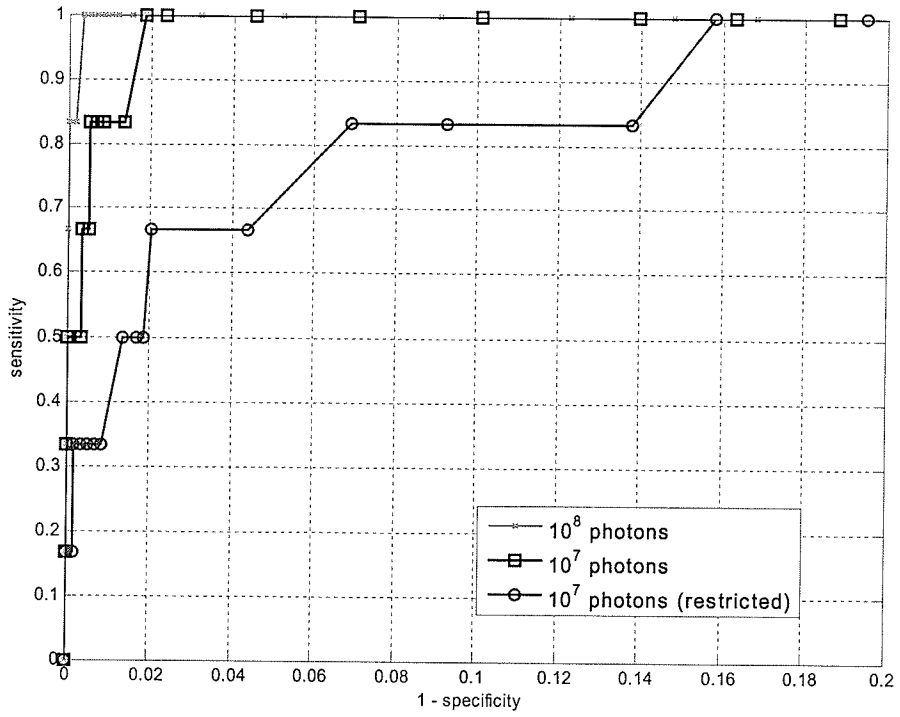


Figure 6.6: ROC curves for each of the three study conditions, indicating that the simulation conditions of studies 1 and 2 have an excellent ability to resolve the inhomogeneities. Note that due to the quality of the results, the ROC plot has been magnified to the upper left hand corner area.

## 6.4 Discussion

The ROC results indicate that our imaging algorithm is a suitable test for the presence of lesions in all three imaging studies. However, while the average deviation from phantom values was less than the uncertainty; the average deviation of the inhomogeneities was greater than the uncertainty, indicating

systematic errors related specifically to quantifying the electron density of the inhomogeneities. Errors are also noticeable at the upstream edge of the phantom, where an overshoot is present.

The second experiment was designed to explore the effects of detecting fewer photons and with an order of magnitude reduction in the number of photons produced an average error of 0.42% in comparison to the 0.28% error of the first experiment, while the measured electron densities of the inhomogeneities were approximately 2% lower than those of the first study. In the third study, the reduced detector space results in only 9% fewer photons being detected but these photons appear to play a significant role in correctly imaging the electron density distribution, particularly with low photon counts.

### 6.4.1 Scope of Results

We use the Klein-Nishina approximation in both our EGSnrc simulation and our reconstruction algorithm. While the Klein-Nishina model is valid when the energy of detected photons is integrated by the detector,[97] our reconstruction technique is subject to the effects of Doppler broadening. However, for the results included in this chapter we have neglected Doppler broadening for the following reasons:

1. Chronologically, the algorithm was still in development. Klein-Nishina physics offers the simplest and most computationally effective form of Compton scatter implementation.

2. Many of the authors cited in section 2.3 have used Klein-Nishina physics for their work, including applications involving energy discrimination, such as the implementation of Achmad.[63]

3. Doppler broadening is more of a concern at low energies (<20 keV), where cross section gradients are larger, and energy bins are smaller (200 eV vs. 500 eV used here).

Multiple scatter has also been neglected during the production of these results. In chapter 7, we present a model of multiple scatter prediction that has proven to be robust under harsher conditions than the ones used here. These conditions include beam position closer to edges and higher detector space gradients.

Coherent scatter has also been ignored, but the inclusion of coherent scatter prediction would theoretically increase the amount of available information, not limit it.

Following the completion and publication in a peer-reviewed journal of the work detailed in this chapter[117], we decided on a change of focus for the algorithm, moving to a mammographic geometry.

### 6.4.2 Extension of the results to three dimensions

Our studies involved one dimensional distributions of electron density along an arbitrary axis, in this case the *z*-axis defined in Figure 4.1. The process

of extending our technique to three dimensions involves scanning the pencil beam along the $x$- and $y$-axes of the phantom. The scanned area would then be imaged in 3D, each voxel being defined by the $(x,y)$ position of the scanning beam, and the z position of the imaged voxel distribution for the $(x,y)$ beam position. Through the use of a scanning pencil beam, only one projection in any direction is needed for 3D electron density imaging if the boundaries of the object are known a priori through other imaging techniques, such as breast CT, photography, or laser delineation.

We propose that CCSR may be combined with breast CT to increase the information content of the resulting image. CCSR may be integrated into breast CT by introducing energy sensitive detectors in a CT detector array (Figure 6.7). CT image reconstruction would involve processing both primary and scatter data to create a fused image or two separate images of attenuation and electron density, respectively. The addition of an electron density image adds atomic information not otherwise present in the primary CT image.

Our results indicate that with the advent of state-of-the-art energy sensitive imaging detectors, it is feasible to reconstruct an electron density image of a phantom using only the Compton scattered photon information due to the interaction of the primary beam with the phantom. We expect the inclusion of coherently scattered photons to increase signal-to-noise ratio. The ability of this approach to generate 3D images from a single projection may allow CCSR to improve the sensitivity and specificity of breast imaging, while retaining comparable dose.

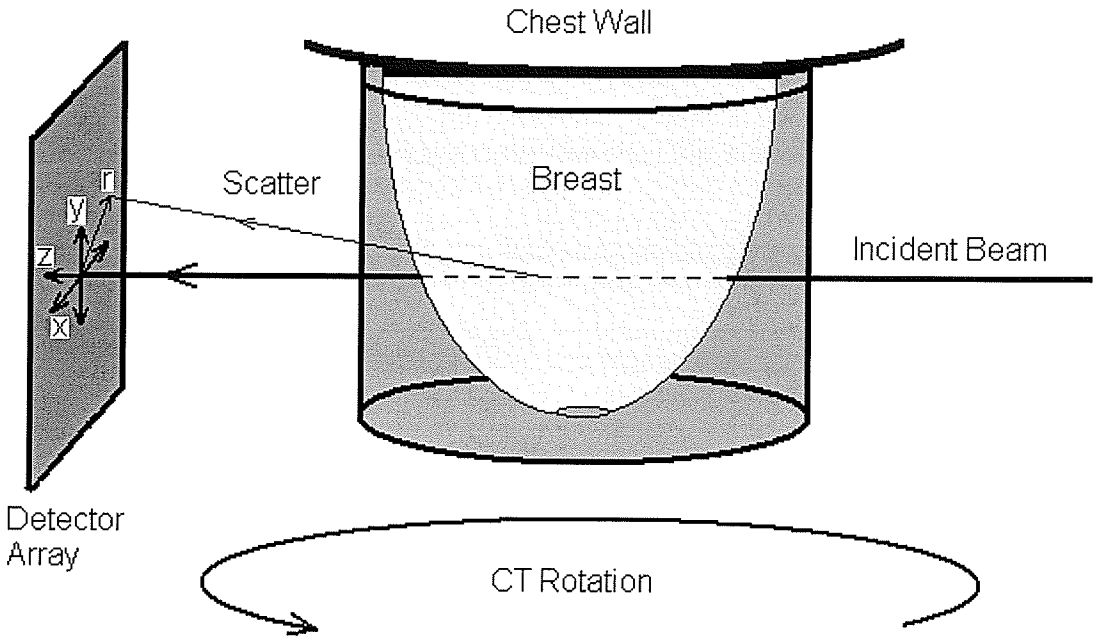


Figure 6.7: Proposed implementation of CCSR into breast CT. The geometry is that proposed by Boone for breast CT. The CT detector array is replaced by a matrix of energy discriminating detectors. The surrounding cylinder is a tissue equivalent sleeve, designed to allow accurate multiple scatter subtraction (see discussion).

# 7

## Compton Coherent Scatter Radiography

## 7.1 Introduction

As discussed in Chapter 2, one of the factors reducing the sensitivity of traditional mammography is the obscuring of lesions by overlapping structural noise. Though breast compression is used to alleviate this problem, structure noise has proven to be one the largest contributors to sub-optimal sensitivity.[118] CCSR may be used as an adjunct to mammography to provide coarse 3D electron density information which may be used to help identify and characterize lesions. Although CCSR does not boast a resolution comparable to mammography, (1 mm theoretical vs. 0.05 mm measured, respectively) it does assist with the crucial problem of overcoming 3D structure noise.

In this chapter, we further develop the CCSR algorithm and apply it to a low energy single projection mammographic geometry. As the simulated breast is compressed, the overall thickness of the phantom is reduced from the phantom introduced in the previous chapter. Klein-Nishina physics approximations are removed, and cylindrical symmetry is no longer assumed as we switch to a more generalized Cartesian geometry. The experiments are divided into two major

sections. The first part deals with multiple scatter correction and the geometry devised to test it. The second part deals with imaging of a simulated accreditation phantom.

## 7.2 Materials and Methods

Several simulation elements are common to both sections. A parallel polyenergetic beam with a 1 $mm^2$ cross section was simulated incident on a 5x5x5 $cm^3$ cubic phantom, representative of a compressed breast. For each beam position, $10^8$ photons were simulated. We used the beam spectrum shown in Figure 7.1, which was obtained by using a molybdenum target and niobium (0.1 mm)/molybdenum (0.15 mm) filtration. The filtrations were selected based on the observations of Calicchia[119], where the molybdenum filtration is supplemented with niobium filtration to remove the molybdenum K$\beta$ line. Calicchia observed increased contrast in mammography with very little increase in glandular dose. Furthermore, a quasi-monochromatic beam dramatically increases the reconstruction speed of CCSR, which is one of the limiting factors of our technique. A quasi-monoenergetic beam of this sort may also be obtained in practice by using either heavy filtration or a crystal to select energies via diffraction, and typically involves attaching a module to a standard mammographic x ray tube.

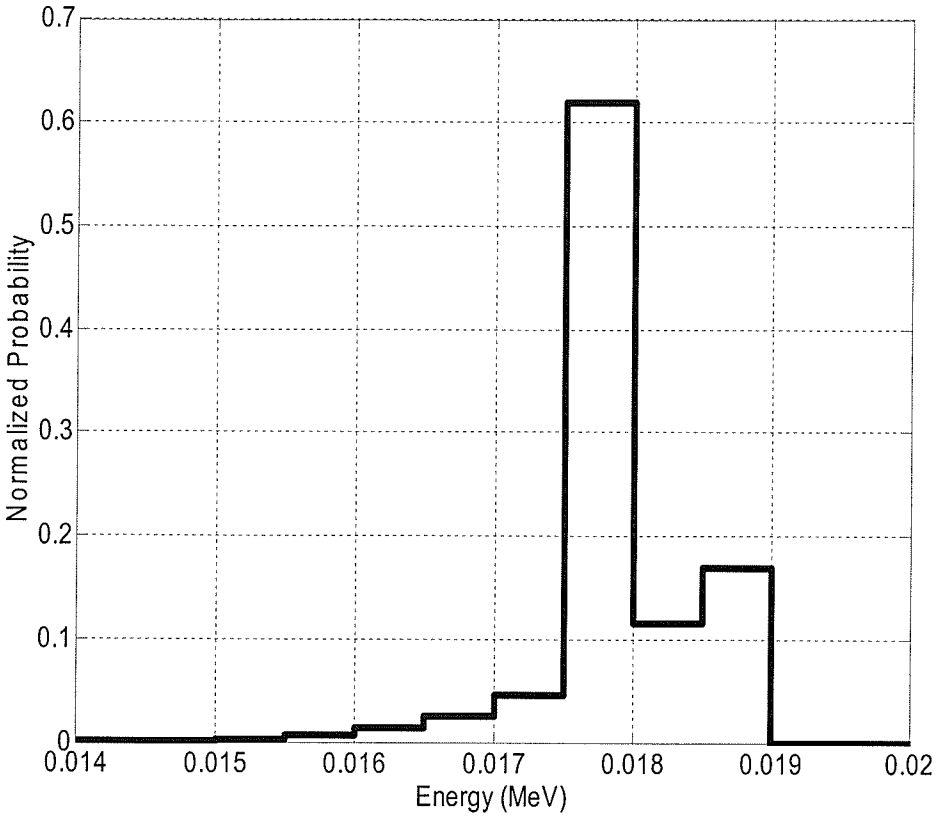


Figure 7.1: X ray spectrum of the incident pencil beam, which would be produced using a standard x ray tube with molybdenum target and niobium/molybdenum filtration[1].

### 7.2.1 Multiple Scatter Correction

Currently, the extraction of atomic structure information from both Compton and coherent scattering is limited to first-order scatter only. To prevent contamination from second order scatter and higher, many scatter techniques implement imaging systems that rely on collimation[57]. Investigation of multiple

scatter typically involves measuring the multiple scatter component in advance for a wide range of collimated geometries[120]. CCSR uses an uncollimated scatter geometry, where the detector system records both the single and multiple scatter signals, the latter component being as large as 40% of the total scatter signal at some locations, based on EGSnrc simulations. The presence of uncorrected multiple scatter introduces large imaging errors in CCSR as the input to the algorithm is assumed to be the single scatter signal. This section describes a method of multiple scatter prediction based on Monte Carlo, allowing accurate subtraction of multiple scatter from the total detector distribution prior to CCSR imaging. The following two subsections examine two solutions which we have considered during the course of this work.

**Parameter Based Model**

In a well defined scattering geometry, it is possible to predict the photon scatter distribution based on a limited number of defining parameters. That is, we would be able to obtain a full scatter spectrum scatter distribution given certain key parameters, such as incident beam spectrum, object location and dimensions, average material composition, and detector position. The distribution could either be calculated analytically (not feasible for multiple scatter), measured through iterative experiment (time-consuming), or simulated using a Monte Carlo technique. For our work, the last technique seems most appropriate.

Using Monte Carlo, an $n$-dimensional parameter space may be simulated iteratively and used as a lookup table. The multiple scatter distribution is especially sensitive to position and in a CT-like geometry, the dimensions of a hanging pendulant breast are difficult to parameterize easily. To solve this, we hypothesized using a water sleeve as shown in Figure 7.2(a) may be used to simplify the shape of the object. The addition of the sleeve effectively creates a cylinder of water equivalent material (water + tissue) which only has three parameters affecting the multiple scatter distribution: diameter, length, and beam position. The situation is of course much simpler in the case of a mammographic geometry, as the breast shape can be parameterized based on paddle separation. There may however still be a need to include a water sleeve, as illustrated in Figure 7.2(b).

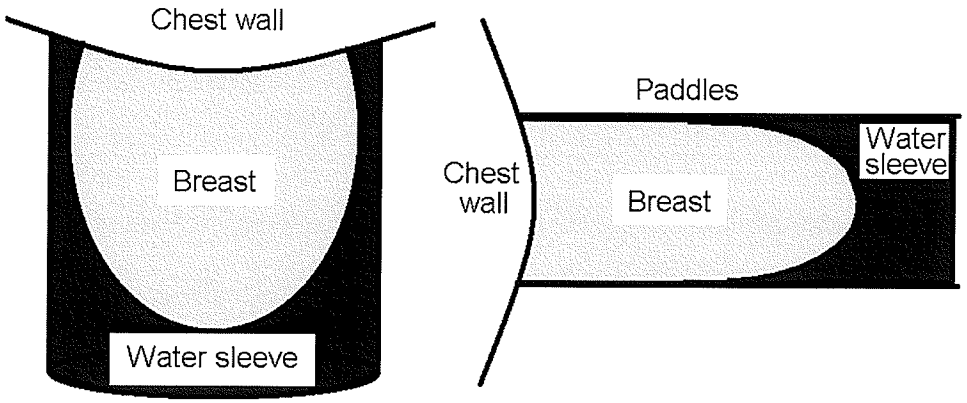


Figure 7.2: Proposed geometries to enable multiple scatter prediction and correction - (a) Pendulum (CT-like) (b) Compressed (mammographic).

**Direct Prediction Using Monte Carlo Simulation**

Using high-performance computing, limited real-time Monte Carlo multiple scatter prediction is now possible during image processing. Instead of a parameter based model, we opted to use an iterative Monte Carlo method of multiple scatter prediction, taking advantage of the simple geometry involved in mammography. The initial multiple scatter distribution is predicted using a homogenous breast phantom, with subsequent iterative imaging, phantom modification, and multiple scatter reprediction. While it is possible to simply use the multiple scatter distribution obtained using a homogenous phantom, we have found that calcifications in the beam line (Figure 7.3) may perturb the multiple scatter signal up to 5% at some positions. These perturbations are of the same order of magnitude as the single scatter perturbations resulting from lesions, and thus we developed this iterative technique to attempt to eliminate them.

While our iterative technique requires a significant amount of computational power, variance reduction techniques can be exploited to decrease the simulation time drastically. In our simulations, electrons are immediately discarded as soon as they are produced. Doing this dramatically speeds up simulation time. The cost of this speed is the accurate reporting of dose. However this is generally not necessary for routine use of the algorithm. We have found that using this approach allows simulations involving $10^8$ primary histories to be performed in 5 minutes or less on a personal computer. This makes it

feasible to dynamically predict multiple scatter by running Monte Carlo simulations during image reconstruction.

As is the case with the parameter based model, several parameters are required to accurately reconstruct the image. However, as we are simulating using Monte Carlo instead of using a lookup system, the situation is a little simpler. For example we do not need to force a simple shape to simulate using a water sleeve; we simply need to know the external dimensions of the object.

In the case of a mammographic geometry, the primary image only provides a limited description of the material distribution. The exterior boundaries can be obtained easily enough from the thickness of the compression paddles, though it may be necessary to include the water sleeve to fill in the air gaps near the distant volume proximal to the nipple.

As a first approximation, the breast is considered to be composed of an average mixture of 50/50 breast tissue. This can be considered to be a robust approximation except when there are inhomogeneities occurring in the object along the beamline (Figure 7.3).

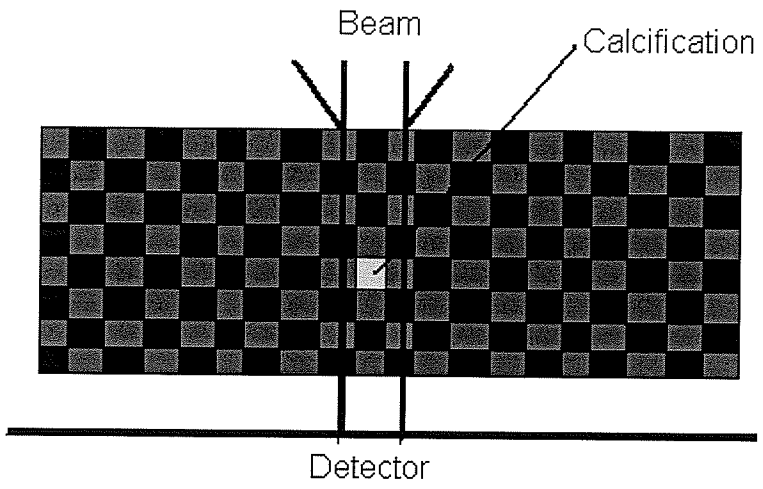


Figure 7.3: High density inhomogeneities in the beam line disrupt accurate multiple scatter prediction using a heterogeneous phantom.

As we demonstrate in section 7.3, the presence of a calcification disturbs the scattered photon distribution significantly. At first, it is difficult to incorporate the effect of the inhomogeneity in simulation due to the lack of $z$ axis information from the primary image.

The details of our iterative technique are outlined in Figure 7.4, and are as follows. As input, CCSR requires single scatter photon distributions, collected using a wide-area energy sensitive detector using no collimation, leading to a three dimensional detector space (one for energy and two for position). The predicted multiple scatter signal is simulated and subtracted from the total experimental signal and the difference is input into CCSR. Variations between the predicted and actual multiple scatter distributions are presumed, and thus the preliminary image is reconstructed using a subset of available scatter data with

multiple scatter components of < 1% (based o EGSnrc simulations). We have found that backscatter with R < 2 cm to conform to this arbitrary restriction. The image is reconstructed using a 1 cm resolution to compensate for the relatively limited (~5%) amount of data being used for reconstruction. Following reconstruction, the image data is used to create a new Monte Carlo phantom, and Monte Carlo multiple scatter prediction is performed again using the new phantom. The new multiple scatter distribution is subtracted from the total distribution and CCSR reconstruction is performed again with a coarse resolution. The results are compared to previous results and if a significant change is present the iterative process continues. When there is no longer significant change between iterations (<0.1% change), we assume that the multiple scatter has been approximated with sufficient accuracy and reconstruct the image using all available scatter data at a higher resolution.

We examined the scatter components resulting from the interaction with the radiation beam described above and a 5x5x5 $cm^3$ phantom. Two beam positions were simulated and compared (Figure 7.5). The first beam position was simulated incident on the center of the top face of the phantom, and is hereafter referred to as the central beam position. Another beam position was chosen incident on the top of the phantom 1.41 cm from the lower left corner of the plan view as defined in Figure 7.5, and is referred to as the edge beam position. In each case, a lesion was placed in the beam line 2.125 cm in depth from the top of the phantom. The lesion corresponds to the insertion of a 0.5x0.5x0.5 $mm^3$ calcification in a 1x1x2.5 $mm^3$ voxel (defined as a type A lesion in the following

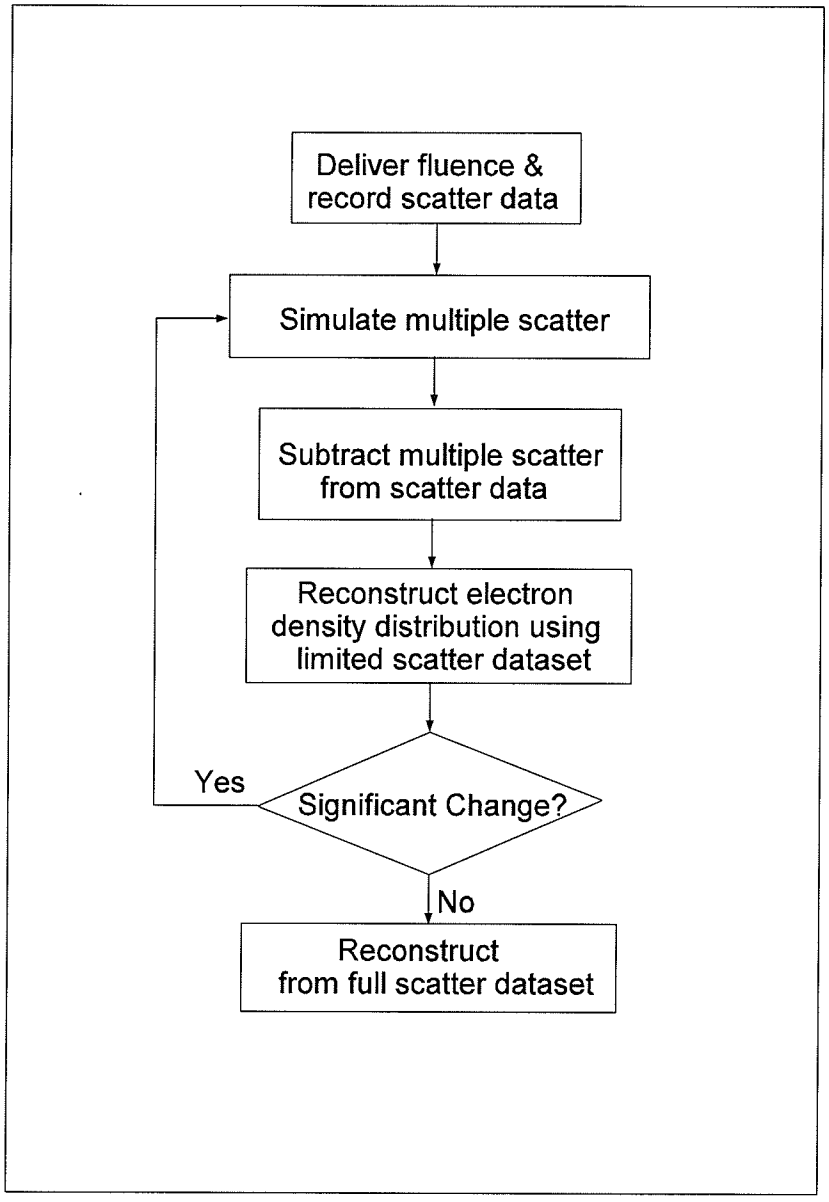


Figure 7.4: Logic diagram of the iterative process of multiple scatter prediction.

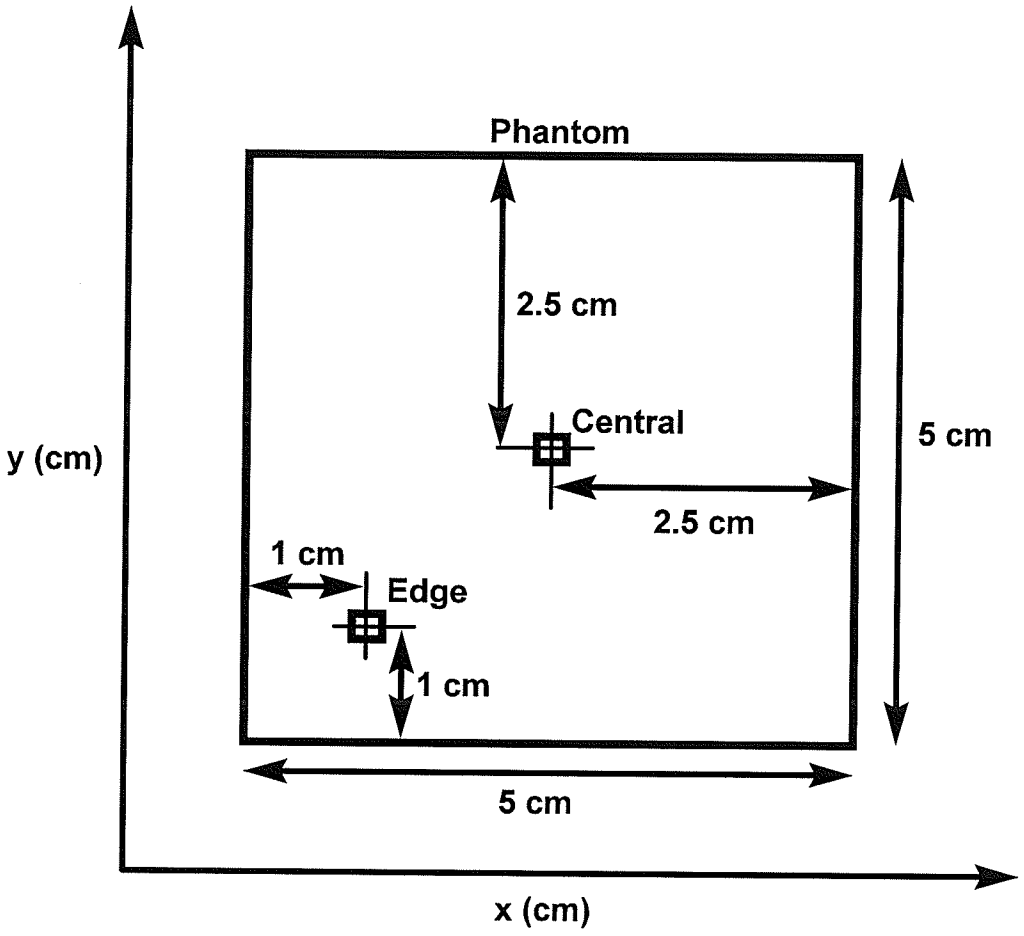


Figure 7.5: Plan view of phantom showing beam positions used to investigate the properties of multiple scatter.

section). Following comparison of the scatter properties of these two situations, the edge beam is then chosen to test multiple scatter correction, as the asymmetric photon distribution inherent in the edge beam position is more challenging to correct.

### 7.2.2 Imaging of an Accreditation Phantom

Using a digital stereotactic mammographic accreditation phantom* as a template, we have constructed a simulated 5x5x5 $cm^3$ breast phantom containing inhomogeneities of various sizes and electron densities. We chose to simulate a phantom with a simulation resolution† of 0.5x0.5x0.5 $mm^3$, allowing us to image small lesions and large calcifications. Our imaging resolution of 1x1x2.5 $mm^3$ is suitable for imaging small low contrast lesions. The strengths of our system lie in imaging low contrast lesions, and thus we focus on imaging an accreditation phantom embedded with lesions of various calcification content. We have selected the dimensions of our lesions to correspond to one voxel in our imaging system, 1x1x2.5 $mm^3$. To obtain the physical properties of the lesions, we have produced 1x1x2.5 $mm^3$ voxels of breast tissue with calcium hydroxyapatite ($Ca_{10}(PO_4)_6(OH)_2$) content of 5%, 3.2%, 2.4% and 1.6% by volume, corresponding to inserting a single calcification of size 0.5, 0.43, 0.39, 0.34 mm in a 1x1x2.5 $mm^3$ voxel of glandular tissue (Table 7.1). We have defined these

* A standard phantom used for testing steoreotactic mammographic equipment.
† This is the resolution used to construct the phantom in DOSXYZNRC, which is different from the resolution used to image the phantom.

lesions as types A-D, respectively. These calcifications sizes are typical of those used in an accreditation phantom.[121] The averaged physical and electron density were obtained using the derivation provided in Appendix A. Each imhomogeneity was replicated five times and ordered in rows of the phantom at various depths. The inhomogeneity centers were placed at 0.375, 1.375, 2.375, 3.375, 4.375 cm from the top of the phantom.

Two larger type D lesions simulating larger tumors of size 4x4x5 $mm^3$ were placed in the phantom with centers at depths 1.5 and 3.5 cm from the top of the slab. Two calcifications of calcium hydroxyapatite of size 0.5x0.5x0.5 $mm^3$ were placed in the phantom with centers at depths 1.275 cm and 3.5 cm, to investigate partial volume effects, as the imaging resolution is greater than the size of the calcifications.

Table 7.1: Summary of lesion types used in the accreditation phantom.

| Lesion Classification | Percentage Calcification by Volume | Percentage Calcification by Weight | Corresponding Calcification Size (mm) |
|---|---|---|---|
| A | 0.05 | 13.8% | 0.5 |
| B | 0.032 | 9.1% | 0.43 |
| C | 0.024 | 1.7% | 0.39 |
| D | 0.016 | 0.5% | 0.34 |

A plan view of the phantom is shown in Figure 7.6, where the pixel values represent the integrated electron density along the z-axis. Figure 7.7 is a simulated radiograph of the phantom, simulated with EGSnrc, with pixel values representing the number of transmitted primaries. Figure 7.8 illustrates a slice of the phantom obtained at y = 3.05 cm, showing how type A lesions were placed at various depths. Figure 7.9 illustrates another slice at a depth of 3.55 cm, where the large tumors and the calcifications are visible.

The matrix of the phantom is composed of glandular and adipose tissue. Simulating structure noise, each simulation voxel value (with the exception of inhomogeneities) was randomly assigned either adipose or glandular tissue, creating a binary structure background with 0.5 mm resolution similar to the structure background used by Bliznakova et al.[102] in their modeling of a simulated breast. Figures 7.10 and Figures 7.11 were produced in a similar fashion to figures 7.6 and 7.7, representing integrated electron density and simulated radiographic plan views. The structure noise has obscured most of the simulated lesions, though larger type A lesions are still visible. Figures 7.12 and 7.13 are analogous to Figures 7.8 and 7.9, showing the inhomogeneities in the presence of structure noise. In Figure 7.13, the electron density of the large type D lesions is 3% higher than glandular structure noise. Please note that the noiseless phantoms are shown here to indicate the locations of the inhomogeneities. The structure noise phantoms were used for actual simulation and image reconstruction.

For each row of inhomogeneities, the beam was scanned through 30 positions, allowing us to produce 30x48 slice images of the phantom. Five scans

were performed, one for each row of lesions and one for the extended lesions/calcifications row.

In addition to imaging the phantom of Figure 7.6, two separate geometries were devised to explore the ability of the algorithm to accurately detect and localize two lesions superimposed on one another along the z-axis. In the first case, we placed two type A 1x1x2.5 $mm^3$ lesions in an otherwise homogenous 5x5x5 $cm^3$ phantom, centered in the phantom along the $x$- and $y$-axis and with centers 0.375 cm in depth from the top and bottom of the phantom along the $z$-axis. This experiment was to investigate the ability of the algorithm to image dual inhomogeneities very close to the skin boundary. It has been demonstrated[73] that lesions occurring within a depth of 14 mm of the breast surface are much more likely to be malignant that deeper lesions. The second experiment we devised involved placing two 1x1x2.5 $mm^3$ lesions centered in the phantom along the $x$- and $y$-axes at 1.875 and 2.375 cm in depth along the $z$-axis, and tested the ability of the algorithm to resolve two closely spaced lesions.

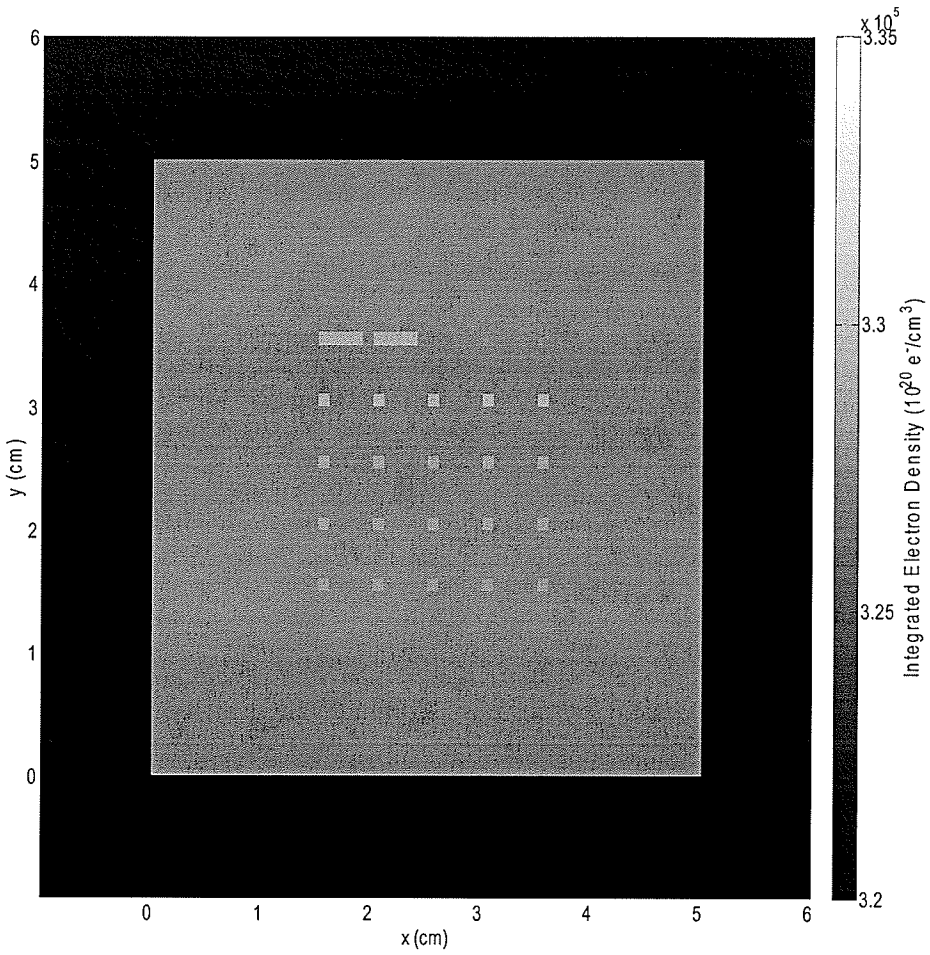


Figure 7.6: Top view of the accreditation phantom, where the pixel values indicate integrated electron density. The first row shows 4x4x5 $mm^3$ lesions of type D and two 0.5x0.5x0.5 $mm^3$ point calcifications. The second row contains 1x1x2.5 $mm^3$ type A lesions. The third, fourth, and fifth rows indicate calcification content of type B, type C, and type D, respectively.

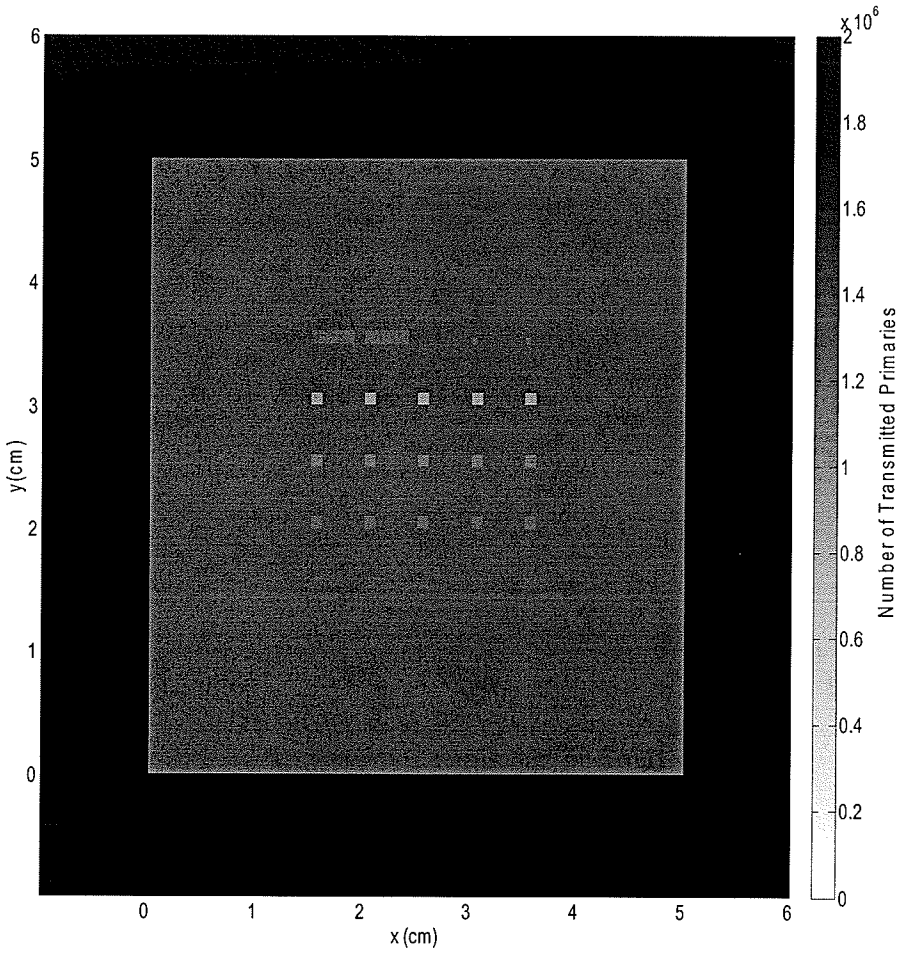


Figure 7.7: Simulated radiograph of the accreditation phantom.

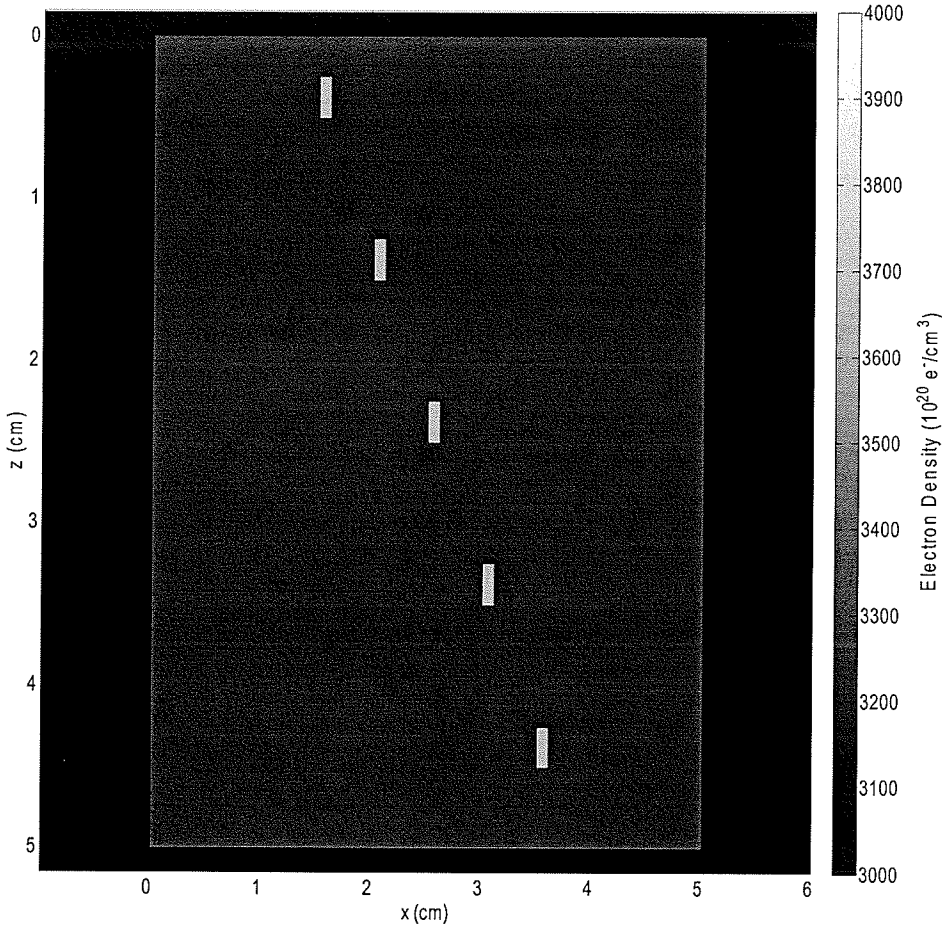


Figure 7.8: Slice taken in the $(x,z)$ plane of the row containing type A lesions. Lesions are spaced 5 mm in the $x$ direction and 1 cm in the $z$ direction.

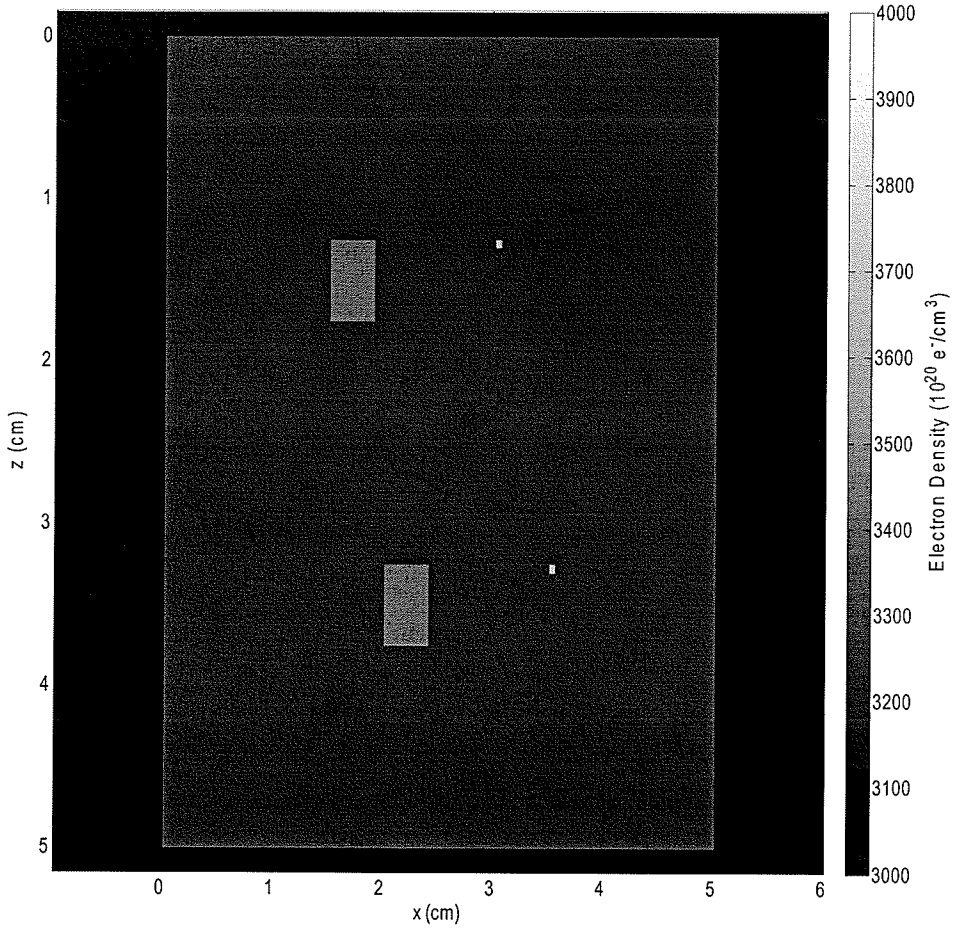


Figure 7.9: Slice in the $(x,z)$ plane of the row containing two large type D inhomogeneities of size 4x4x5 mm$^3$ and two 0.5x0.5x0.5 mm$^3$ calcifications, spaced 2 cm apart in the $z$-direction and 0.5 cm in the $x$-direction.

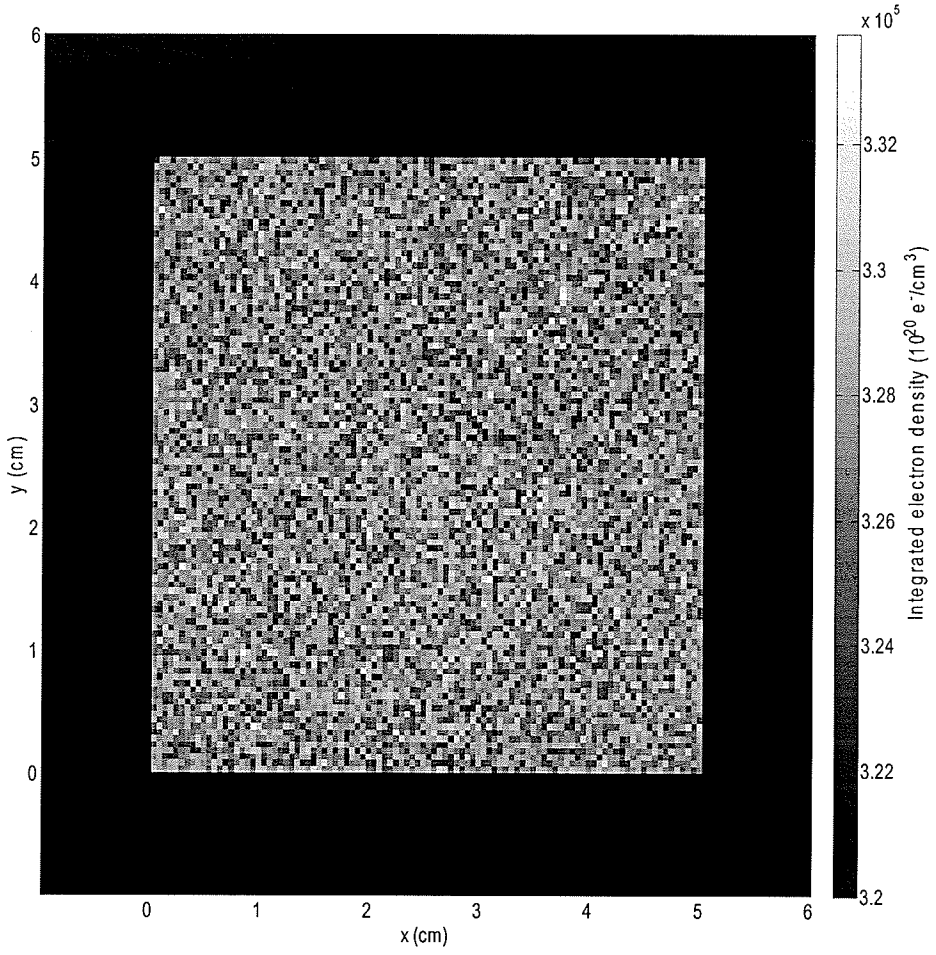


Figure 7.10: Top view of the integrated phantom after the introduction of 50/50 adipose glandular structure noise, where pixel values indicate integrated electron density. Abnormal features of the phantom are washed out.

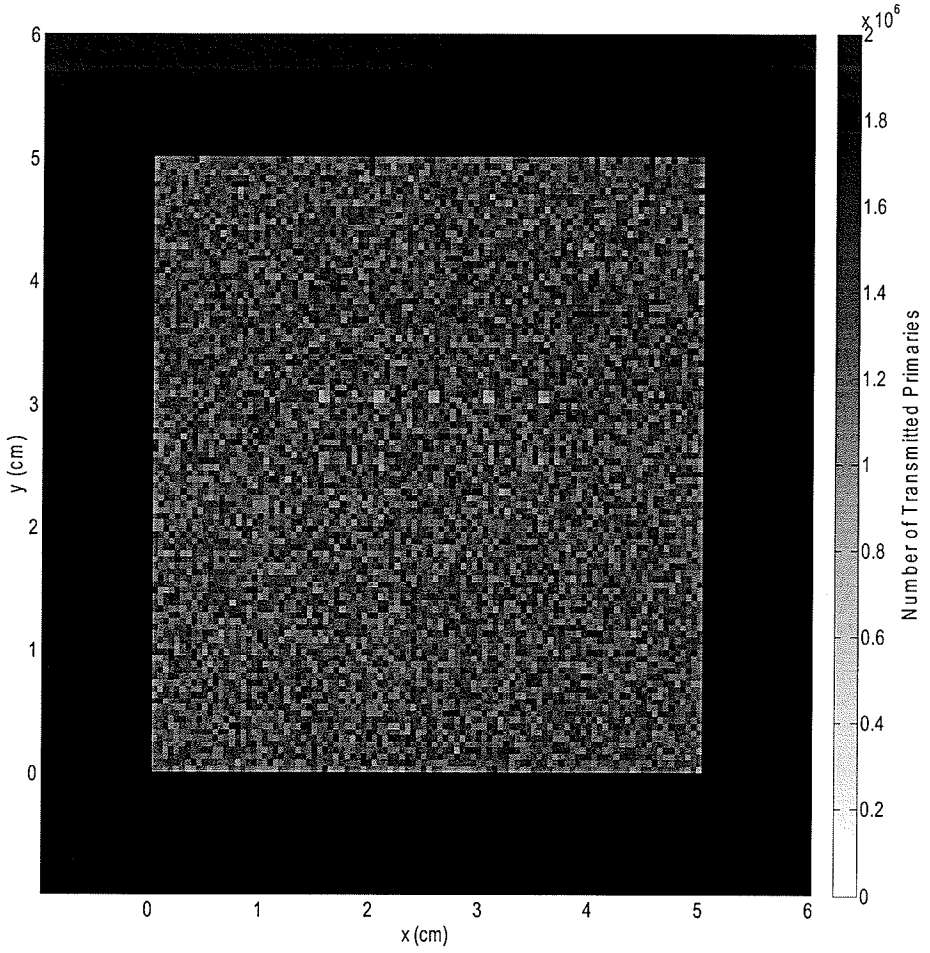


Figure 7.11: Simulated radiograph of the accreditation phantom after the introduction of structure noise. Type A lesions are visible due to the non-linear properties of photon attenuation.

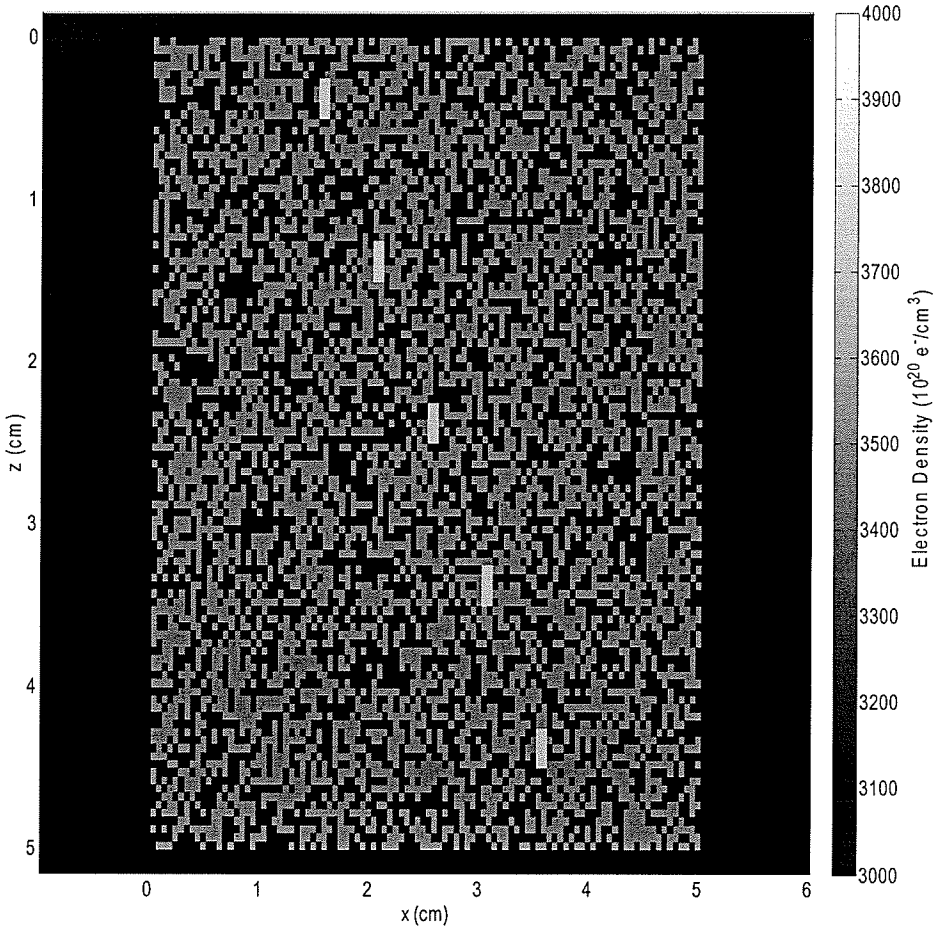


Figure 7.12: Slice taken in the *xz* plane of the row containing type A lesions in the presence of structure noise. Lesions are spaced 5 mm in the *x* direction and 1 cm in the *y* direction. Structure noise resolution is 1x1x2.5 mm$^3$.

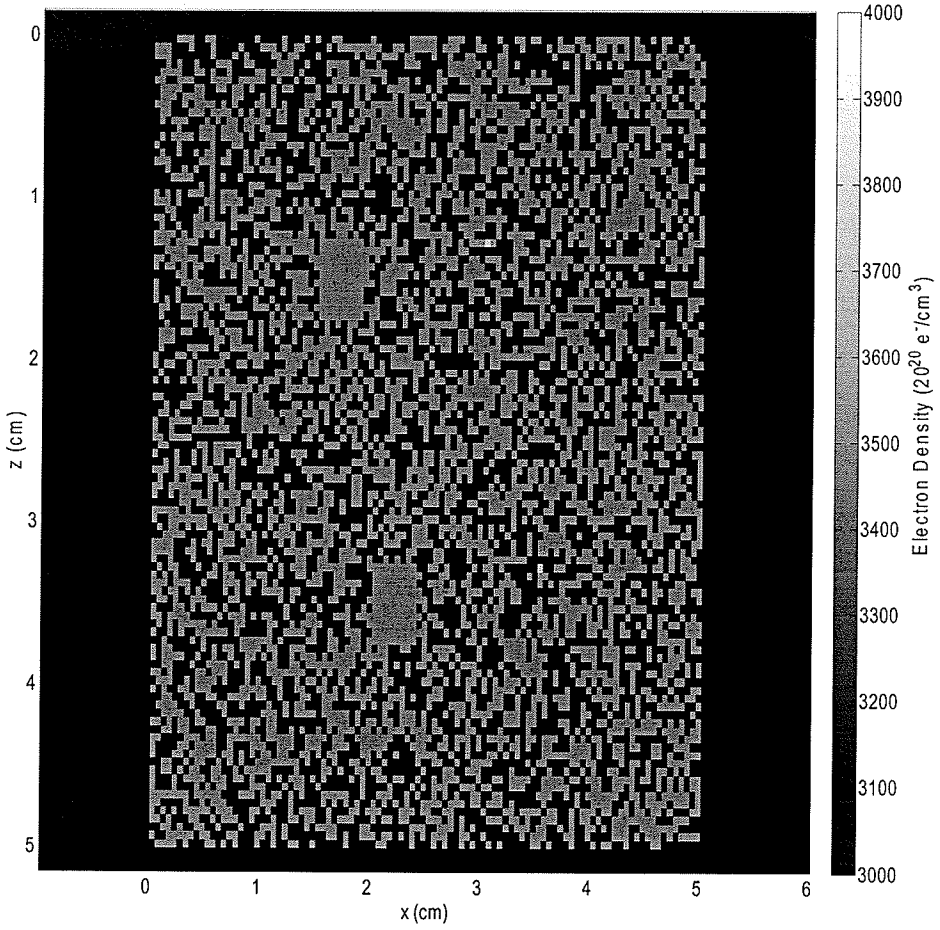


Figure 7.13: Slice in the *xz* plane of the row containing two type D lesions (4x4x5 $mm^3$) and two 0.5x0.5x0.5 $mm^3$ calcifications, spaced 2 cm apart in the *z*-direction and 0.5 cm in the *x*-direction.

For each slice scan of the accreditation phantom, several image quality parameters were calculated. Mean and standard deviation of electron density is presented for each image, and are calculated for the normal and abnormal voxel groups. Three image quality parameters were calculated. Contrast-to-noise ratio (CNR) is a good test of the visibility of the lesions over the background of normal tissue, and is calculated using the following equation[3]:

$$CNR = \frac{\frac{1}{M}\sum_{m=1}^{M}\rho_e^m - \frac{1}{N}\sum_{n=1}^{N}\rho_e^n}{\sigma} \tag{7.1}$$

The first term in the numerator is the average of $M$ abnormal voxels and the second term is the average of $N$ normal voxels. $\sigma$ is the standard deviation of the normal voxels, which is approximately equal to the standard deviation of the abnormal voxels.

Reconstruction fidelity can be assessed using a root mean square difference between the electron density image and the original phantom:

$$\delta = \left| \left(\frac{1}{mn}\right) \sum_{i=1}^{m}\sum_{j=1}^{n} \left[\rho_e^{image}(i,j) - \rho_e^{phantom}(i,j)\right]^2 \right|^{1/2} \tag{7.2}$$

where $m$ and $n$ are the matrix dimensions of the reconstructed image, and $\rho_e^{image}$ and $\rho_e^{phantom}$ are the electron densities of the imaged and original phantom, respectively.

A Mann-Whitney unpaired non-parameterized test was performed on each slice image to test the null hypothesis that the distribution of voxels containing lesions did not vary significantly from the distribution of normal tissue voxels. The results of this test determine if CCSR can separate the distributions of normal and malignant image voxels.

Finally, a receiver operating characteristic (ROC) curve was generated to test the relative quality of the test to predict the presence of cancer. The area under the ROC curve was calculated and used to evaluate the test.

## 7.3 Results

### 7.3.1 Multiple Scatter

Scatter distributions when the beam is incident on the center of the phantom are shown in Figure 7.14. Table 7.2 gives the number of scattered photons belonging to first, second, and third or more orders, as well as percentages of the total forward or back-scatter.

Multiple scatter distributions when the beam is incident on the edge of the phantom are shown in Figure 7.15. The results for the edge beam position are given in table 7.3.

We note that multiple scatter can account for as much as 32.9% of the total scatter signal, in the case of forward scatter of the center beam position.

Also, the magnitude and distribution of scatter signal is a function of beam position (central or edge). In the case of forward scatter, we note differences in Table 7.2: Distribution of first, second, and third or higher order scatter for a central beam position.

| Scatter Order | Forward | Backward |
|---|---|---|
| First | 1035559 (67.1%) | 3920211 (79.0%) |
| Second | 373349 (24.2%) | 814285 (16.4%) |
| Third or more | 134597 (8.7%) | 228967 (4.6%) |

Table 7.3: Distribution of first, second, and third or more order scatter for an edge beam position.

| Scatter Order | Forward | Backward |
|---|---|---|
| First | 2237199 (73.0%) | 4406850 (78.7%) |
| Second | 651678 (21.3%) | 952826 (17.0%) |
| Third or more | 173592 (5.7%) | 240146 (4.3%) |

the edge beam position relative to a central beam position. The single order scatter signal increases 5.9%, the second order scatter signal decreases 2.9%, and the third order and more scatter decreases by 3%. The changes in backscatter are smaller, with < 1% difference occurring over all orders of scatter. Furthermore, the total scattered photon fluence of the edge beam position is 33% higher than for the central beam position, due to the decrease in attenuation of scattered photons near the edge relative to a central beam position. When only 2$^{nd}$ order

scatter and higher is considered, the increase in edge beam fluence is 14%, demonstrating that multiple scatter for a central beam position would be insufficient for edge beam correction, as the error is higher than the aforementioned 1% tolerance.

Due to an asymmetric geometry, the single and multiple scatter for an edge beam position is more challenging to predict, and thus we focus on this case when presenting results. The total spatial photon distribution at the detector plane is shown in Figure 7.16. The distribution is asymmetric, with an increased amount of scatter for negative values of $x$ and $y$, as expected due to generally shorter radiation path length, integrated over all scattering centers. The multiple scatter signal is shown in Figure 7.17 for both Compton and coherent components. The mean value of the image is 21 counts/pixel, with a standard deviation of 11 counts/pixel. The breakdown of the multiple scatter into Compton and coherent components is shown in Figure 7.18.

Figure 7.19 shows a plot of the difference between actual and predicted multiple scatter distributions. The mean value of the plot is 0.1 counts/pixel, indicating a systematic error of less than 0.1%. The background is mainly dominated by statistical error with standard deviation of 6.6 counts/pixel.

Figure 7.20 (a) represents the converged electron density distribution, obtained from using the total scatter distributions with no multiple scatter correction. Voxels associated with breast tissue vary from 3.14 to $3.58 \times 10^{23}$ $e^-/cm^3$, and the value of the voxel associated with calcification (arrow) is $3.50 \times 10^{23}$ $e^-/cm^3$, 6.7% lower than expected. Furthermore, despite a true positive

in the abnormal region, the detection is masked by four false positives with higher electron density values. Following correction of multiple scatter (Figure 7.20 (b)), breast tissue voxels fall within the narrower range of $3.17\text{-}3.41\text{x}10^{23}$ $e^-/cm^3$, and the voxel associated with calcification has an electron density of $3.74\text{x}10^{23}$ $e^-/cm^3$, deviating 0.2% from the expected value and 9.7% above the highest value ($3.41\text{x}10^{23}$ $e^-/cm^3$) of the normal range. No false positives exist in the abnormal region, indicating a successful detection with a ROC score of 1.

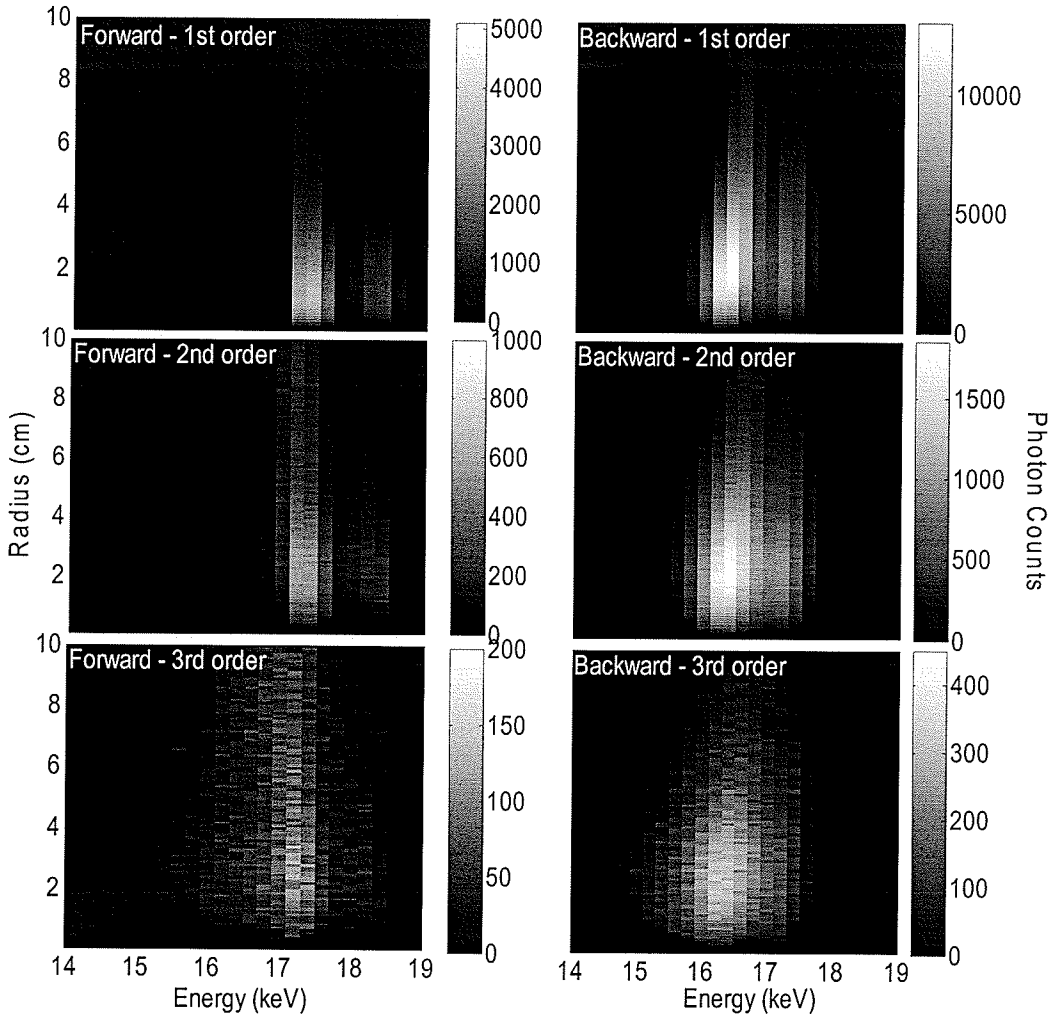


Figure 7.14: Scatter distributions for a central beam position, sorted by order (1st row – single, 2nd row – double, 3rd row – third and higher) and type (1st column – forward scatter, 2nd column – backscatter)

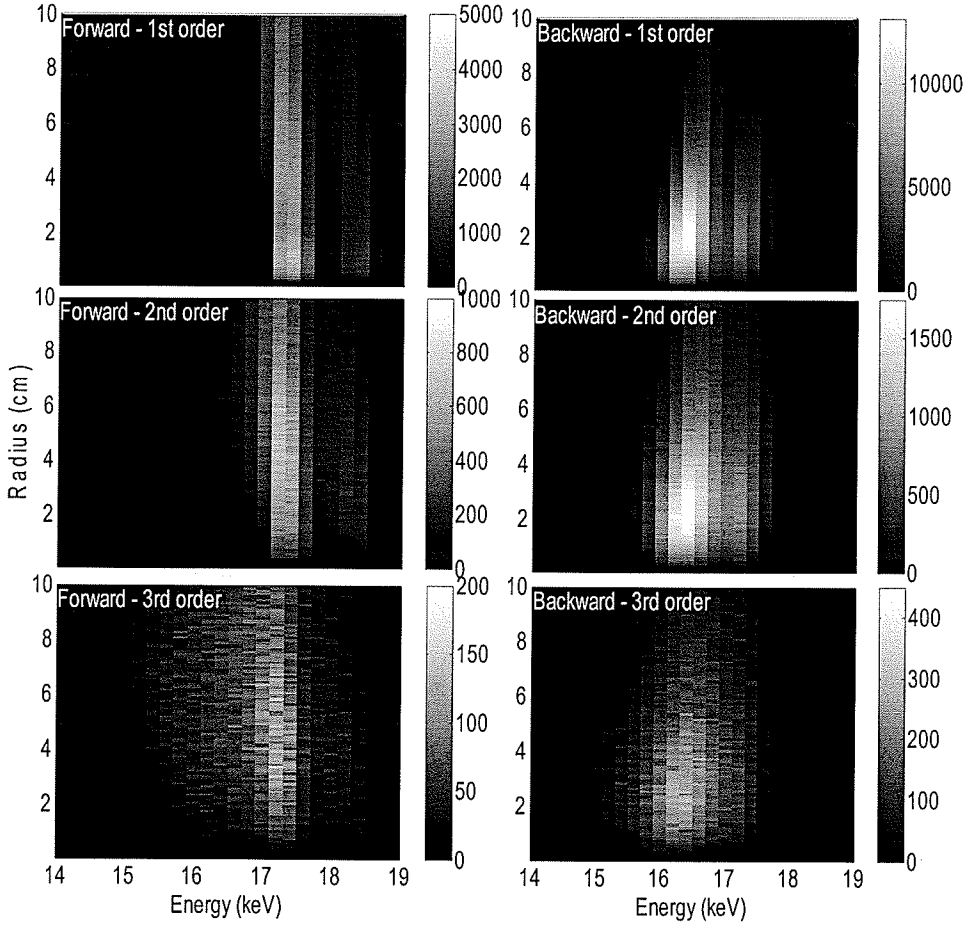


Figure 7.15: Scatter distributions for an edge beam position, sorted by order (1st row – single, 2nd row – double, 3rd row – third and higher) and type (1st column – forward scatter, 2nd column – backscatter)

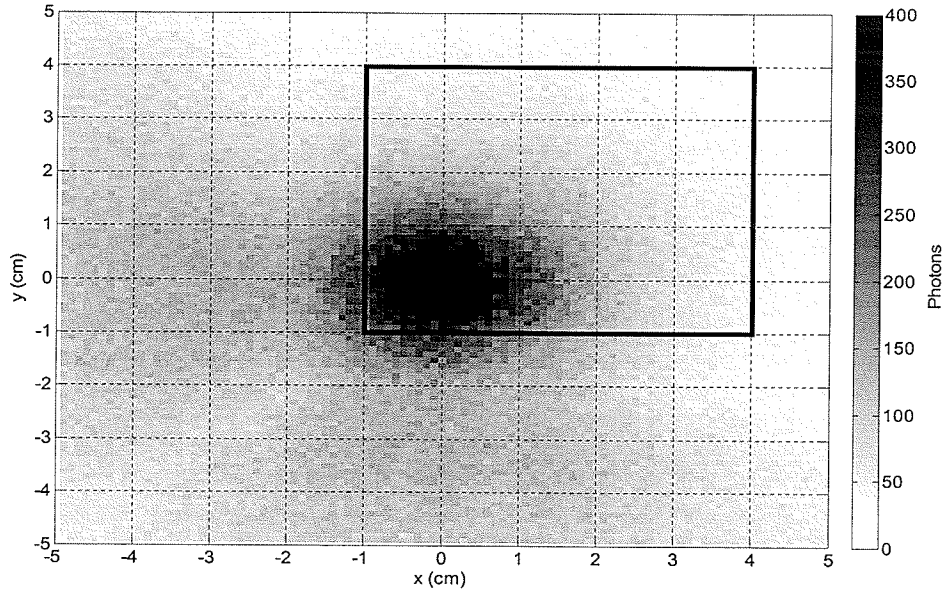


Figure 7.16: Spatial distribution of all orders of scatter on the forward detector plane.

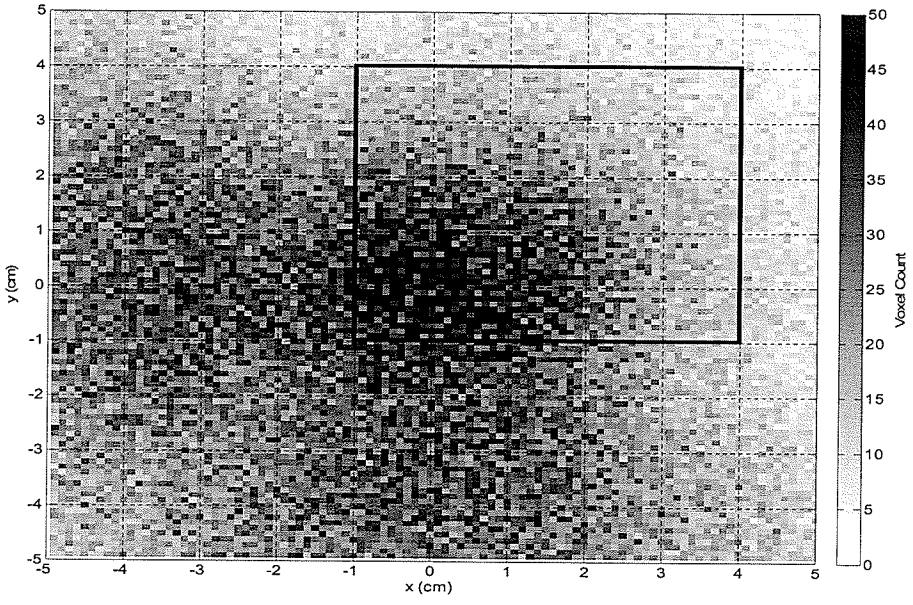


Figure 7.17: Spatial distribution of multiple scatter ($2^{nd}$ order and higher scatter) on the forward detector plane.

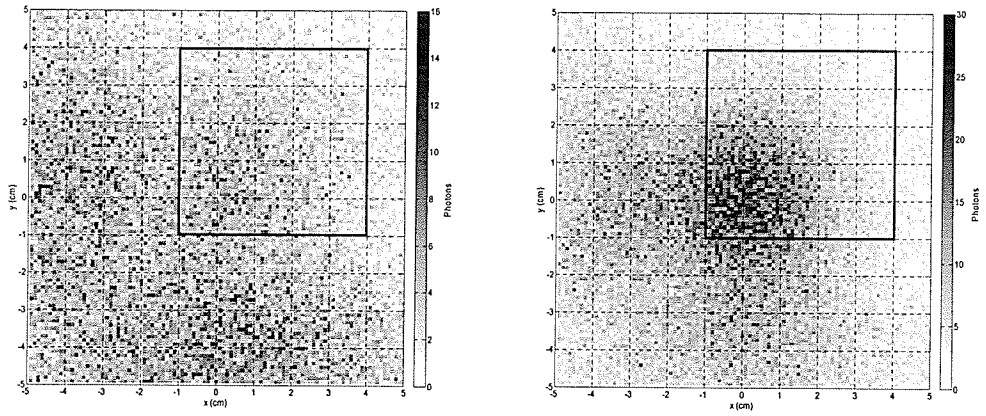


(a) (b)

Figure 7.18: Spatial distribution of 2nd order and higher (a) Compton and (b) coherent scatter.

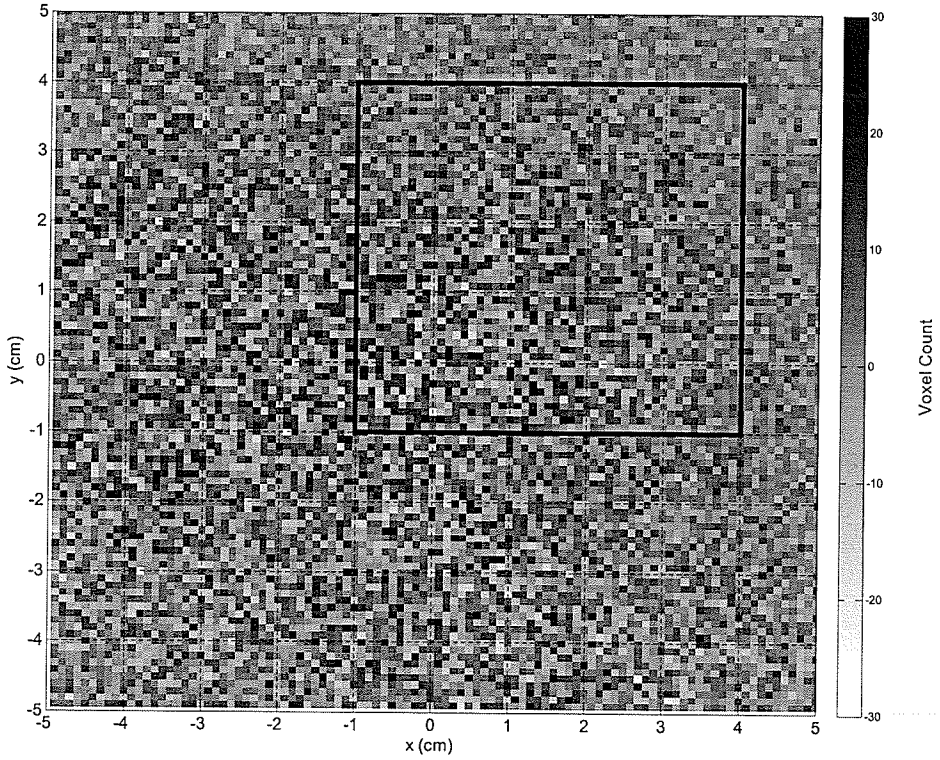


Figure 7.19: Corrected multiple scatter distribution.

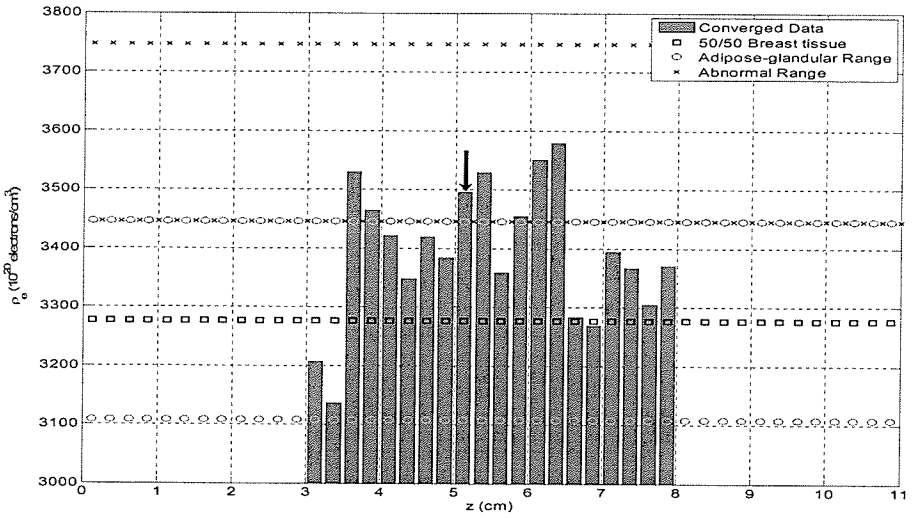


(a)

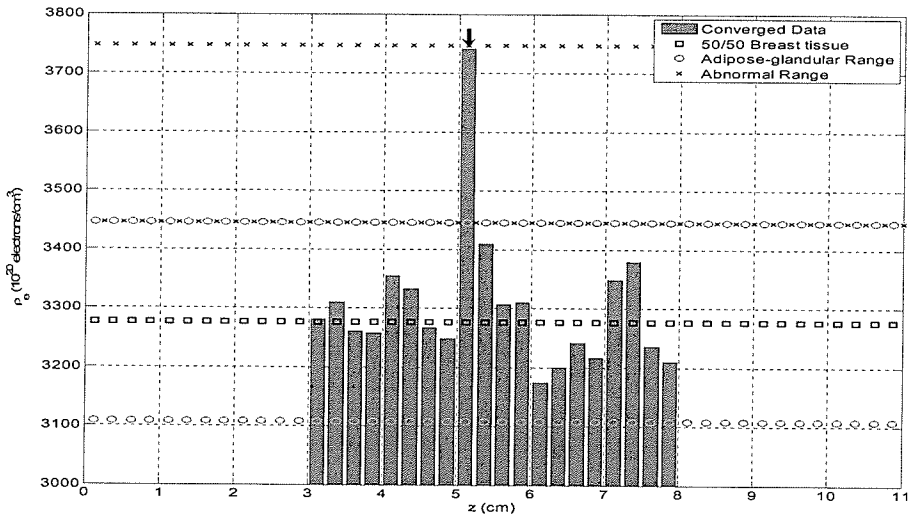


(b)

Figure 7.20: Electron density distributions (a) before and (b) after multiple scatter correction.

### 7.3.2 Accreditation Phantom

Figures 7.21-7.24(a) show the electron density images produced as the beam was scanned across each row of inhomogeneities of the phantom. For each image, a histogram of electron density values is shown, in 7.21-7.24(b). Image quality parameters were calculated, and are summarized in Table 7.4.

As illustrated in Figure 7.21(a), type A are readily visible (according to the Rose criterion*), with a difference of $503 \times 10^{20}$ $e^-/cm^3$ between mean normal and abnormal tissues. Standard deviation of both normal and abnormal distributions is less than $100 \times 10^{20}$ $e^-/cm^3$. There is no overlap between distributions (Figure 7.21(b)), and the CNR is within the range of 5-8 specified by the Rose criterion for easy visibility.

For type B lesions (Figure 7.22(a)), the gap between means reduced to $385 \times 10^{20}$ $e^-/cm^3$, while the error of the abnormal distribution increased to $146 \times 10^{20}$ $e^-/cm^3$. As can be seen on Figure 7.22(b), an overlap occurs between the two distributions. The CNR is 4.2, falling outside of the Rose criterion range. However, most lesions are still identifiable on the image.

The results of type C lesions are similar to those of type B, with a small decrease in the standard deviation of the abnormal distribution and a drop in lesion visibility (Figure 7.23(a)). Three lesions fall inside the overlap range, and the CNR has fallen to 3.04 (Figure 7.23(b)).

* Small lesions are clearly visible when CNR > 5.

Finally, type D lesions are no longer readily visible on the electron density image (Figure 7.24 (a)). Four of the five lesions fall within the overlap zone (Figure 7.24 (b)).

Figure 7.25 shows the electron density image of the extended lesion and the calcifications.

For the idealized case of a perfect image, the electron density histogram is shown in Figure 7.26. For the purposes of determining statistical significance and generating ROC curves, the voxels of adipose and glandular tissue were combined to form a population of 'normal' voxels. In Figures 7.21-7.24, the distribution of 'normal' voxels is non-Gaussian, thus we decided to use the non-parametrized Mann-Whitney statistical significance test.[122] The results of the test indicate that the lesion groups in each image are different from the population of normal voxels to a significant degree. ROC curves were generated for Figures 7.21-7.24. The ROC results are shown in Figure 7.27. As expected, the results worsen as the lesion calcification content is reduced. Type A ROC results indicate a perfect test. For type D lesions, the ROC area drops to 0.958, still indicative of an excellent test, and one point on the ROC curve indicates a sensitivity of 80% and a specificity of 82%, on par with mammography.

The ROC curve corresponding to the image of extended lesions and point calcifications (Figure 7.25) is shown in Figure 7.28. The ROC area of the lesions is 0.879 (very good), while the ROC area of the calcifications is 1. The CNR of the lesions was 2.13, while the CNR for the calcifications is 4.09, both below the Rose criterion.

We were interested to determine if imaged normal tissue voxels were correlated with the phantom counterparts. The phantom was converted to a resolution matching the image. The phantom electron densities were then subtracted from the image to yield Figure 7.29. A histogram of electron density values belonging to the difference image is shown in Figure 7.30. To check correlation, a new phantom was created with the same lesions but with a new randomly generated structure pattern. The subtraction was repeated. A Wilcoxon signed-rank test[123] was performed to determine if the actual subtraction image (Figure 7.29) differed significantly from a subtraction image generated using the fake phantom. The resulting Spearman correlation coefficient[124] was 0.092, indicating a significant paired correlation between the real subtraction image and the fake one. Since the correlation between the image and both real and fake phantoms is the same, we conclude that as far as the normal tissue image values are concerned, no correlation exists between the phantom values and the image values.

The results of the overlapping lesion experiments are shown in Figure 7.31 and Figure 7.32. In each case, the expected lesion electron density is $3.75 \times 10^{20}$ electrons/cm$^3$, indicated by the upper boundary of the abnormal range. While normal tissue values image in the proper range, there appears to be a systematic undershoot of lesion electron density values. In Figure 7.30, the undershoot is $20 \times 10^{20}$ electrons/cm$^3$ and $90 \times 10^{20}$ electrons/cm$^3$, or 0.5% and 2.5%, respectively. In Figure 7.31, the undershoot is $100 \times 10^{20}$ electrons/cm$^3$ and $140 \times 10^{20}$ electrons/cm$^3$, or 2.7% and 3.9%, respectively.

However, in each image, both lesions correctly register as true positives, with no other voxel values in the abnormal range. In both cases the ROC score is 1, considered excellent.

Table 7.4: Summary of mean and standard deviations of electron density as a function of calcification level and image quality tests.

| Lesion Type | Electron density ($x10^{20}$ electrons/$cm^3$). Error is 1st standard deviation. | | Expected Normal Electron Density | Expected Abnormal Electron Density | Statistically significant? (Mann-Whitney) | CNR | RMS ($x10^{20}$ electrons/$cm^3$) | ROC Area |
|---|---|---|---|---|---|---|---|---|
| | Normal | Abnormal | | | | | | |
| A | 3286±94 | 3789±80 | 3275 | 3747 | p=0.0001 (extremely) | 5.37 | 55.0 | 1 |
| B | 3284±91 | 3669±146 | 3275 | 3638 | p=0.0001 (extremely) | 4.20 | 56.9 | 0.999 |
| C | 3280±86 | 3542±117 | 3275 | 3590 | p=0.0002 (extremely) | 3.04 | 55.9 | 0.982 |
| D | 3278±85 | 3501±109 | 3275 | 3542 | p=0.0005 (very) | 2.63 | 55.4 | 0.958 |

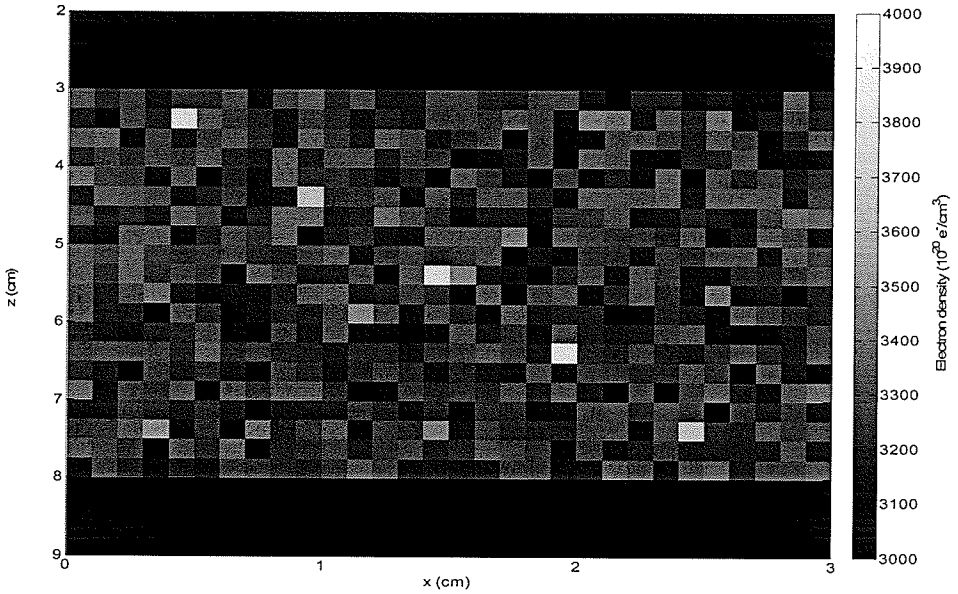


(a)

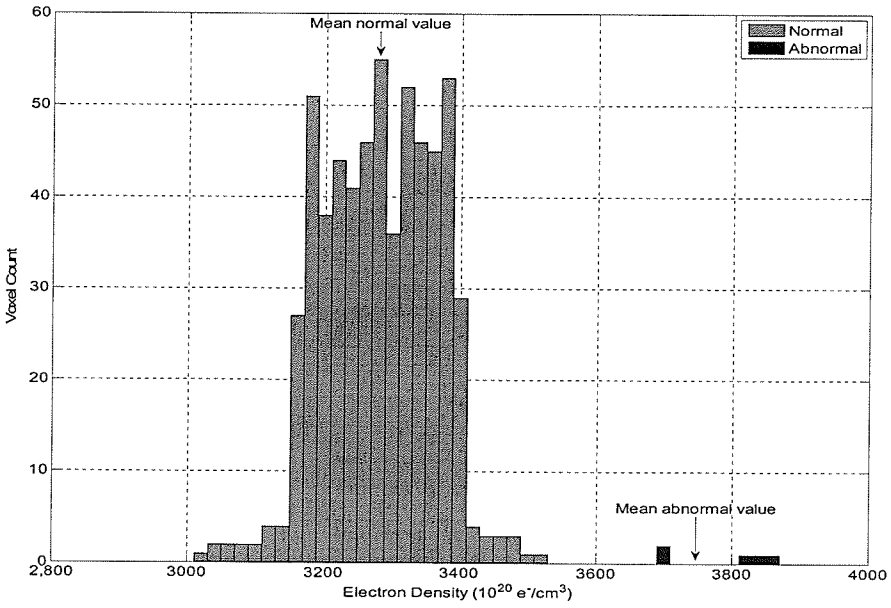


(b)

Figure 7.21: (a) Image of the row of type A lesions. (b) Distribution of electron densities.

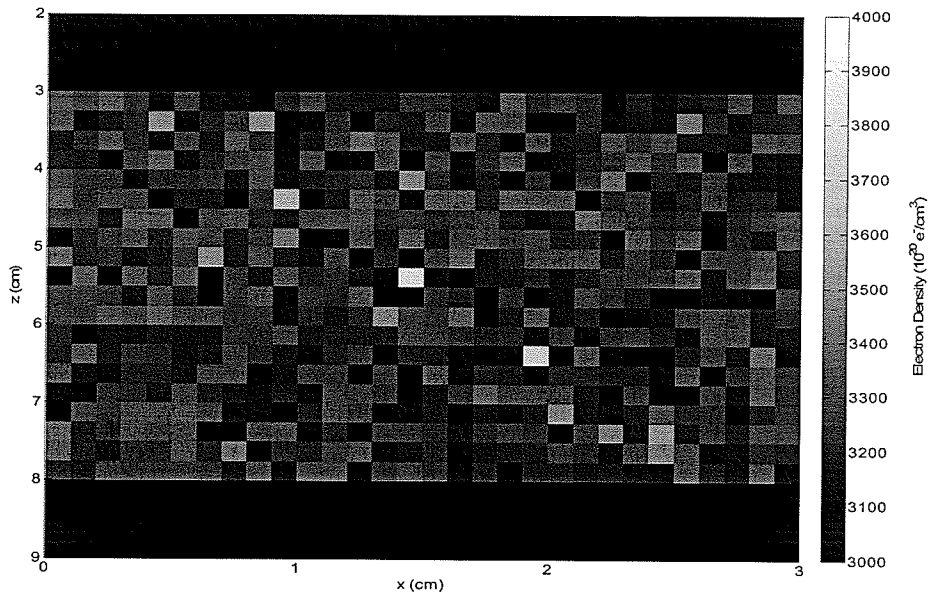


(a)

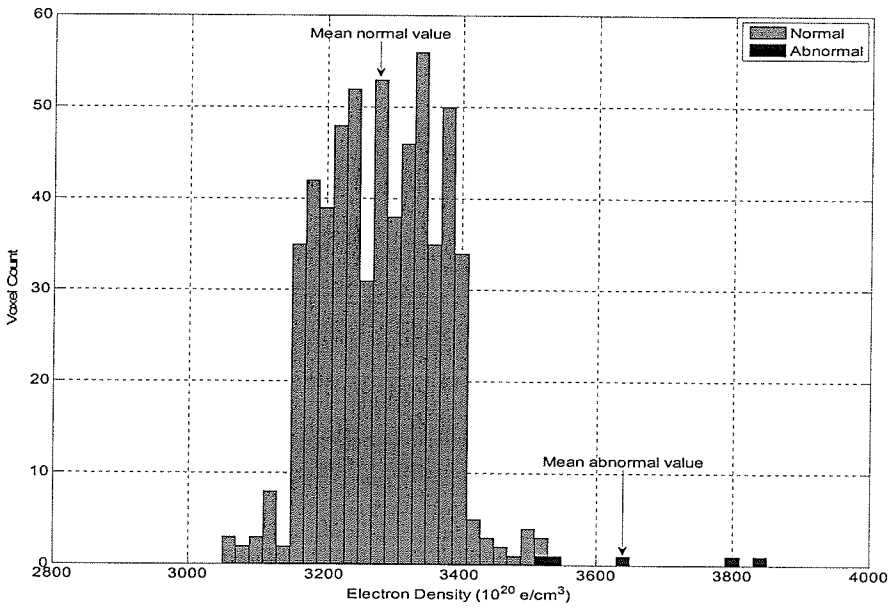


(b)

Figure 7.22: (a) Image of the row of type B lesions. (b) Distribution of electron densities.

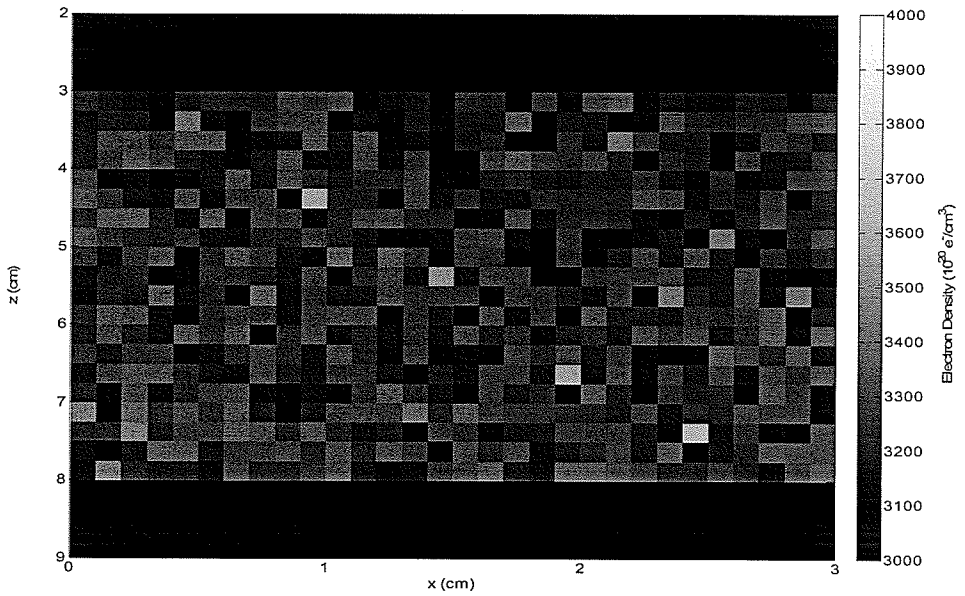


(a)

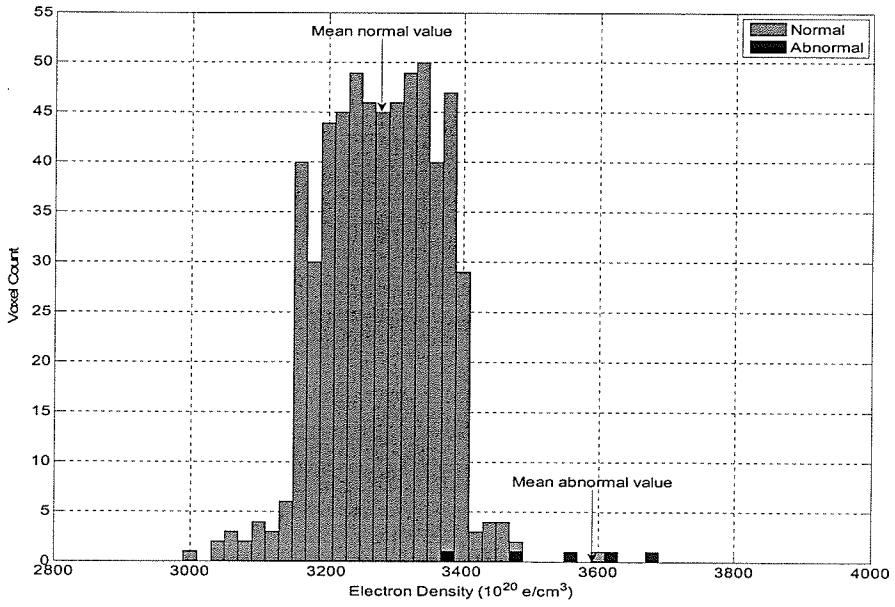


(b)

Figure 7.23: (a) Image of the row of type C lesions. (b) Distribution of electron densities.

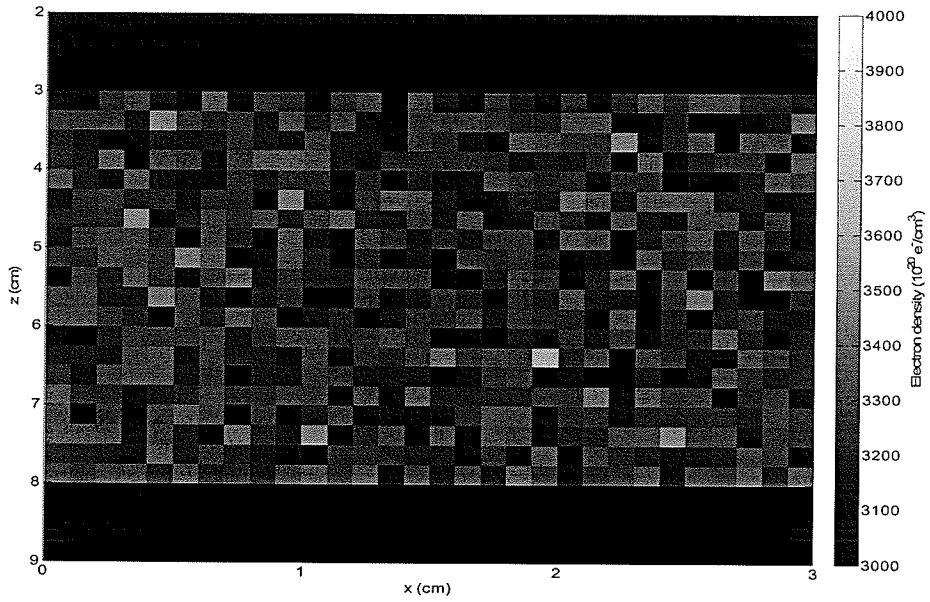


(a)

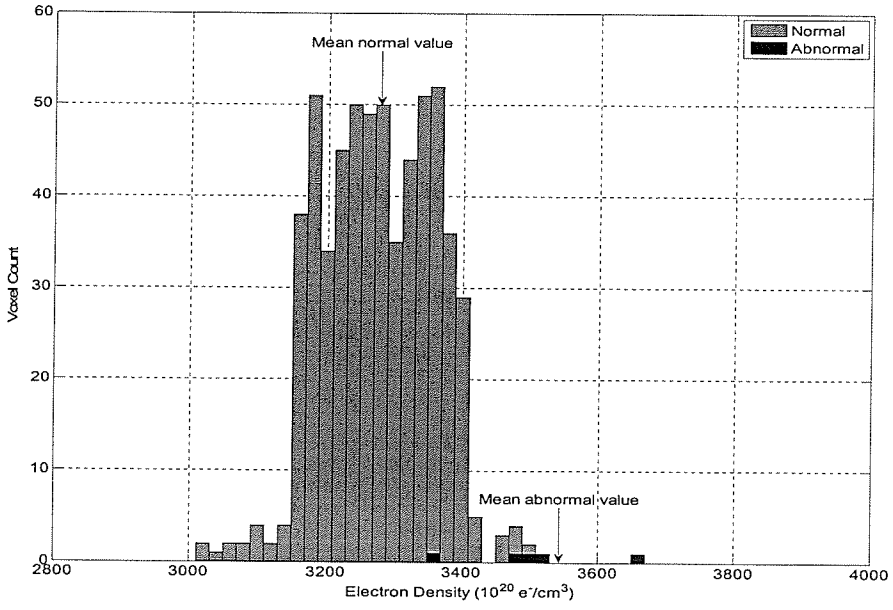


(b)

Figure 7.24: (a) Image of the row of type D lesions. (b) Distribution of electron densities.

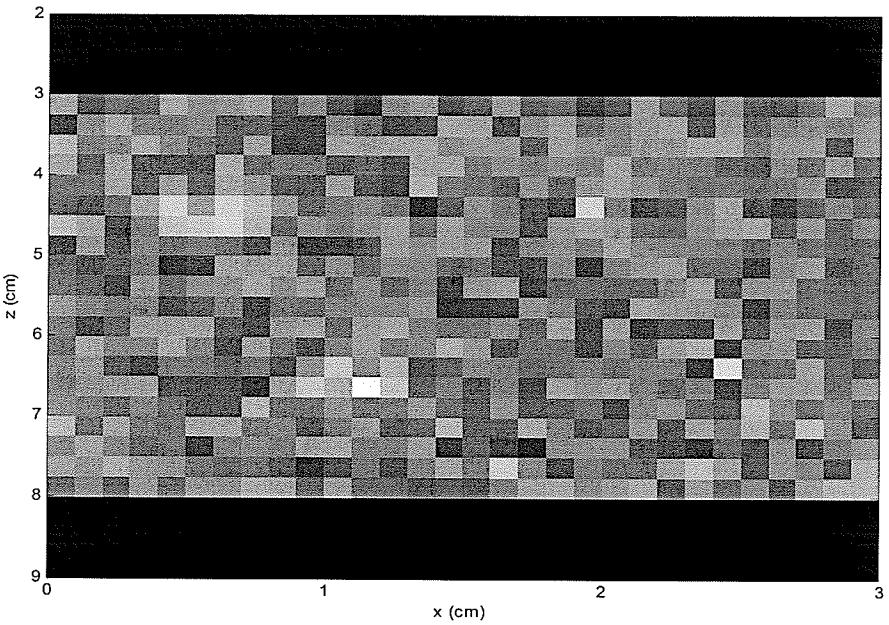


Figure 7.25: Image of extended type D masses and 0.5x0.5x0.5 $mm^3$ calcifications.

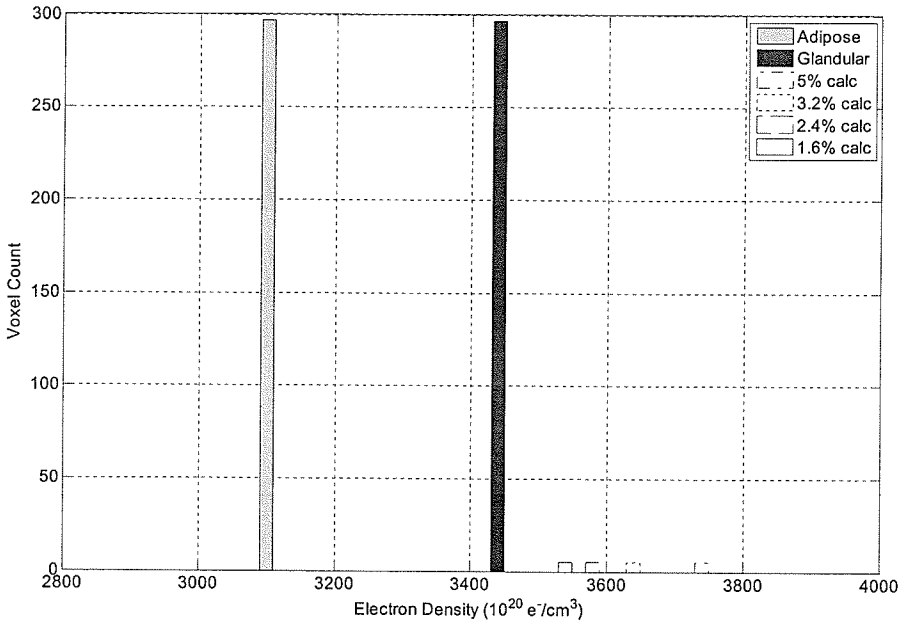


Figure 7.26: Ideal electron density histogram.

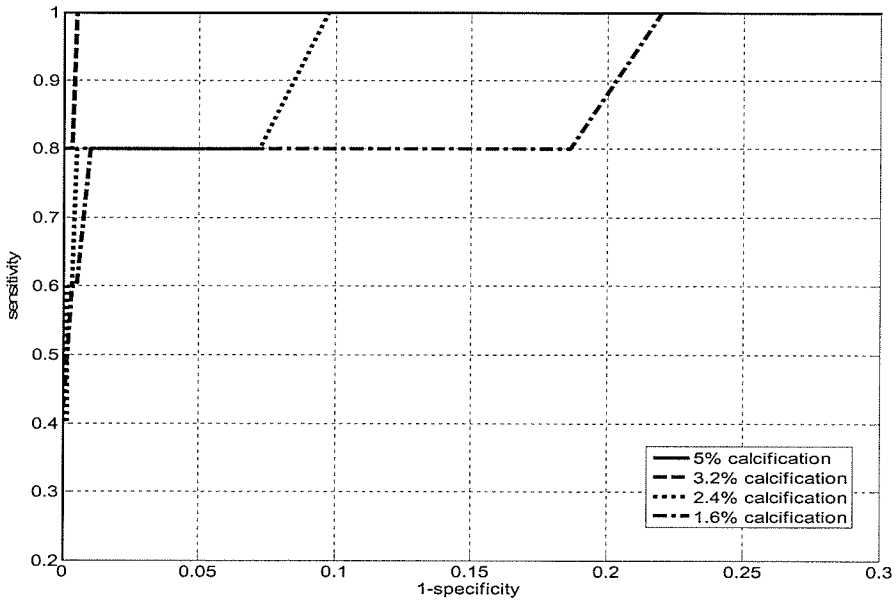


Figure 7.27: ROC curves for lesions ranging in calcification from 5% to 1.6%.

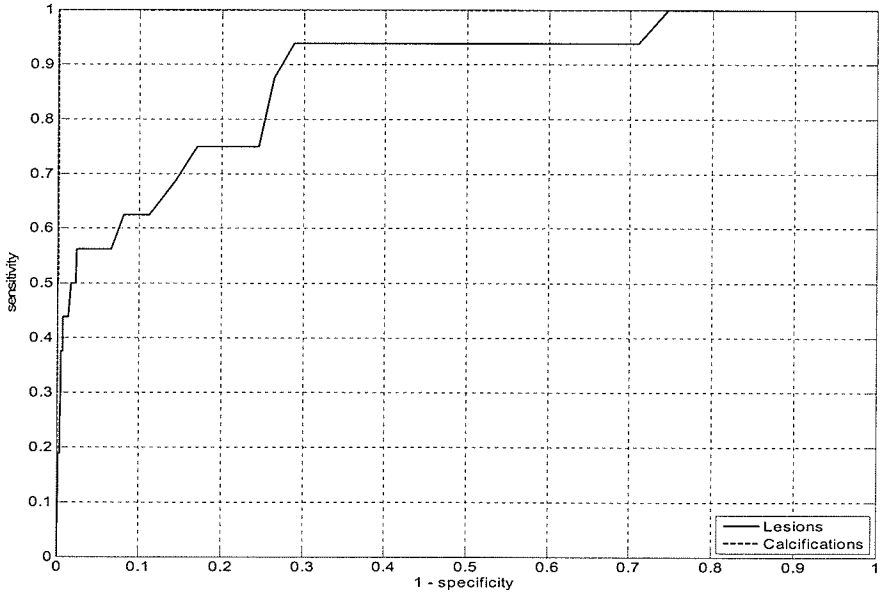


Figure 7:28: ROC curves for extended type D lesions and 0.5x0.5x0.5 $mm^3$ point calcifications.

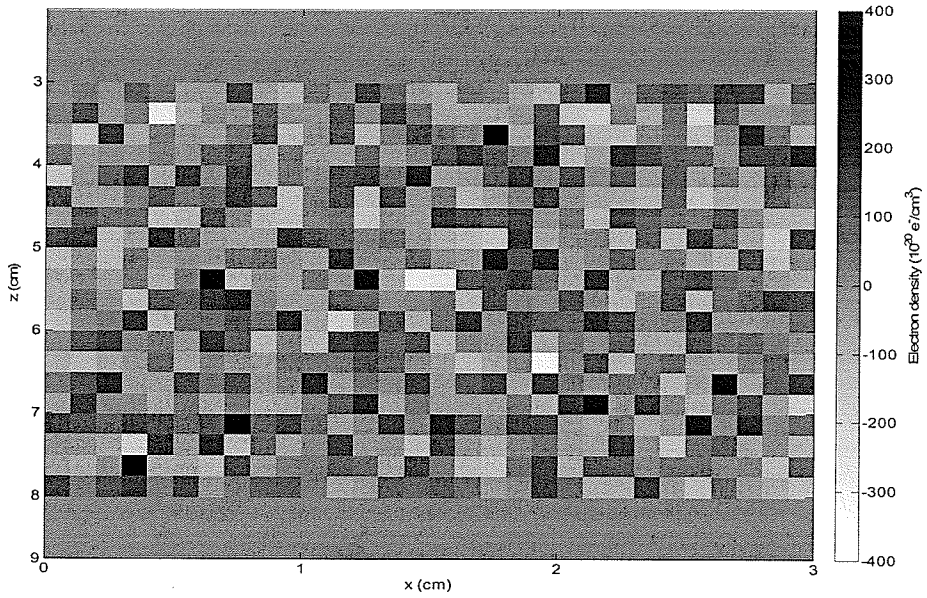


Figure 7.29: Difference image generated by subtracting the Figure 7.20(a) from the corresponding phantom slice.

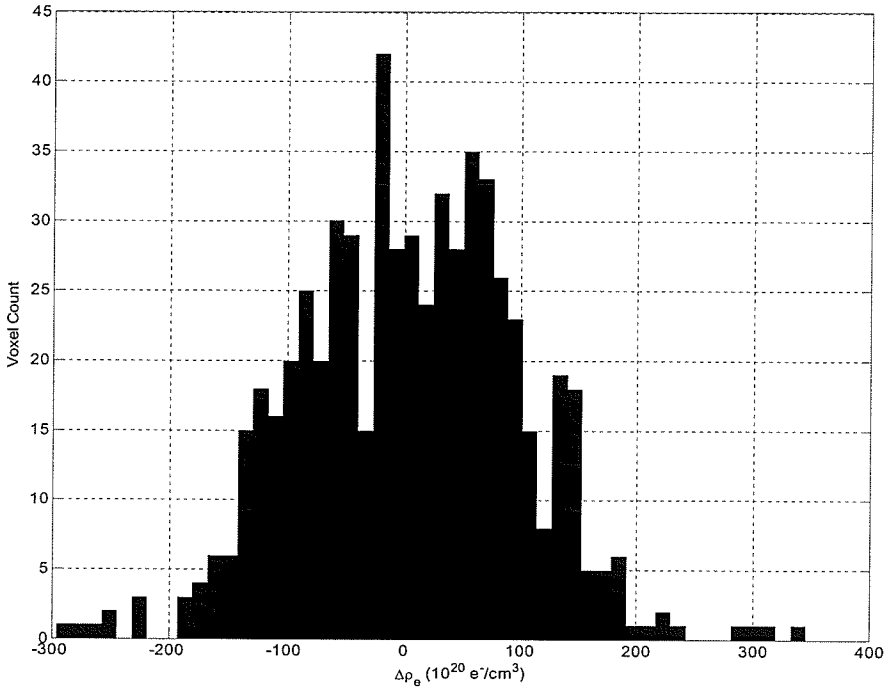


Figure 7.30: Electron density distribution of Figure 7.28.

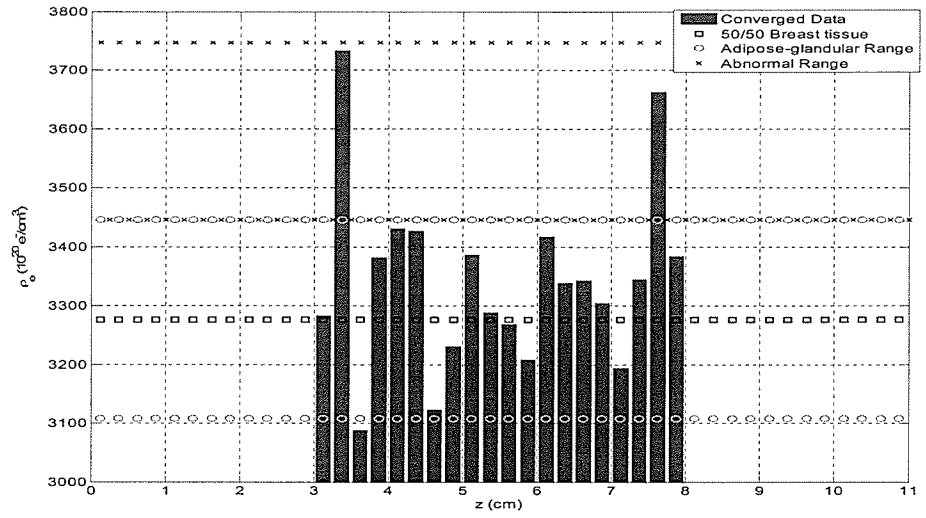


Figure 7.31: Histogram of electron density as a function of $z$ for overlapping lesion case 1. Both lesions are near phantom boundaries, and are clearly imaged in the abnormal region.

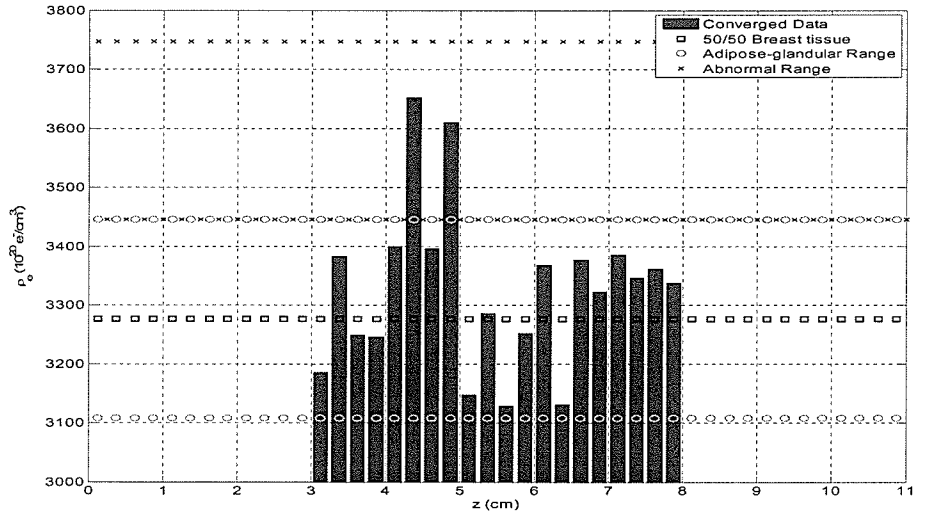


Figure 7.32: Histogram of electron density as a function of $z$ for overlapping lesion case 2. Both lesions are near the center of the phantom, and are clearly imaged in the abnormal region.

## 7.4 Discussion

Variance reduction techniques offer the potential to use Monte Carlo simulations in our reconstruction algorithms. The high tolerances required by CCSR have required the development of an algorithm for accurate prediction of multiple scatter, iteratively using the image information generated using CCSR to reconstruct and repredict multiple scatter distributions. The use of this technique offers the potential for CCSR to be implemented clinically in a mammographic setting.

Modeling a scanning pencil beam and an asymmetric inhomogeneous phantom in a Cartesian geometry, we have demonstrated an imaging algorithm capable of generating 3D images with a single projection. The suitability of CCSR as a lesion detection modality was validated using a simulated accreditation phantom. ROC scores ranging from 0.958 to 1 indicate the ability of the algorithm to image lesions of varying calcification content at various depths. Using a Mann-Whitney correlation test, these results have been confirmed.

We have also explored the ability of the imaging algorithm to resolve two overlapping lesions. While the lesions were successfully identified, a systematic underestimate of the electron density values are apparent. So far, these underestimates cannot be explained. The influence of many parameters remains a topic for future work, discussed more fully in Chapter 9.

Limitations of the test include remaining approximations, idealized geometry and detector, and a narrow scanning beam. While the narrow pencil beam approach is inherent to the technique presented in this chapter, converting to a fan beam is theoretically possible with the assumption of a unique solution. However, we feel we have achieved a sufficient degree of realism to warrant experimental development of the imaging system.

# 8

## Compton Spectrometry

## 8.1 Introduction

We mentioned in Chapter 7 that elemental composition data was limited or lacking for mixtures such as calcified tissue. This fact prompted us to investigate whether our imaging system could be used for spectroscopic purposes. The physical model of Doppler broadening indicates that the elemental composition of each voxel of tissue had a direct effect on the resulting scattered photon distribution. In fact, the Doppler profile of each element is uniquely characteristic of the element in question.

A brief summary of some spectroscopic methods used to analyze samples in organic chemistry and their limitations are as follows:

- Infrared (IR) spectroscopy measures the bond vibration frequencies in a molecule and is used to determine the functional group.
- Optical absorption or emission spectrometry: this technique converts atoms of a material into in a state which will either absorb or transmit

characteristic light. It is insensitive to the major organic elements such as carbon, hydrogen, oxygen, and nitrogen.

- Mass spectrometry (MS) fragments the molecule and measures the masses of the fragments. The fragment masses are used to search a database of known fragments for a match. Routine use of the technique is limited by the contents of the fragment database as well as by time and cost.
- X ray fluorescence (XRF): X ray fluorescence spectroscopy uses a method of exciting a sample with electrons, and subsequently measuring the flux of characteristic photons which are emitted. However, this method suffers limitations, the most important being an inability to properly determine the fractional composition of elements with atomic numbers below that of carbon. The determination of the fluorescence yield of elements lighter than sodium (Z=11) is experimentally difficult due to low yields.[125]
- Nuclear magnetic resonance (NMR) spectroscopy detects signals from hydrogen atoms and can be used to distinguish isomers. However, it is insensitive to other organic atoms.
- Ultraviolet (UV) spectroscopy uses electron transitions to determine bonding patterns. It is however difficult to identify the elemental composition from this information.
- Secondary Ion Mass Spectroscopy (SIMS) involves bombarding the surface to the tested with a stream of ions. Secondary ions are released by the material and measured. Sensitive to organic ions, but destructive, and only records information from the surface of a target material.

These methods are limited in their ability to universally determine elemental composition due to their dependence on atomic and molecular configurations.

The usage of Compton scatter for spectroscopy is not new, though it typically involves the determination of effective atomic number or electron density[126] as opposed to a full breakdown of elemental composition. While the application presented by Hazan et al. was not spectroscopic in nature, the authors did suggest that the Doppler profiles of various elements are characteristic of the elements in question, and can be adequately measured using a germanium energy sensitive point detector. Naydenov et al.[127] proposed a multi-energy radiographic approach to perform elemental spectroscopy, theorizing that the relative composition of elements from carbon (Z=6) to uranium (Z=92) could be determined.

## 8.2 Materials and Methods

In previous chapters, we argued that is was necessary to link the electron density of a voxel with the complete elemental composition. This approximation was necessary as it was impossible to reconstruct the image otherwise. Normally, the algorithm reconstructs a 1D matrix of electron density values. Uncoupling the elemental composition matrix would increase the number of convergence variables by a factor equal to the number of potential elements. At present, the algorithm is not able to handle such a large number of variables.

Now, consider the geometry illustrated in Figure 8.1, where the usual large volume of tissue has been replaced with a small single voxel sample. Since only one voxel contains material (this is known beforehand), the electron density plus the uncoupled elemental composition can be reduced to 7 variables, the electron density and the elements hydrogen, carbon, nitrogen, oxygen, phosphorous, and calcium, in the case of breast imaging. The volume of the sample needs to be known to correct scatter attenuation. The imaging algorithm can then be adapted to 'image' the elemental composition using the same iterative convergence technique.

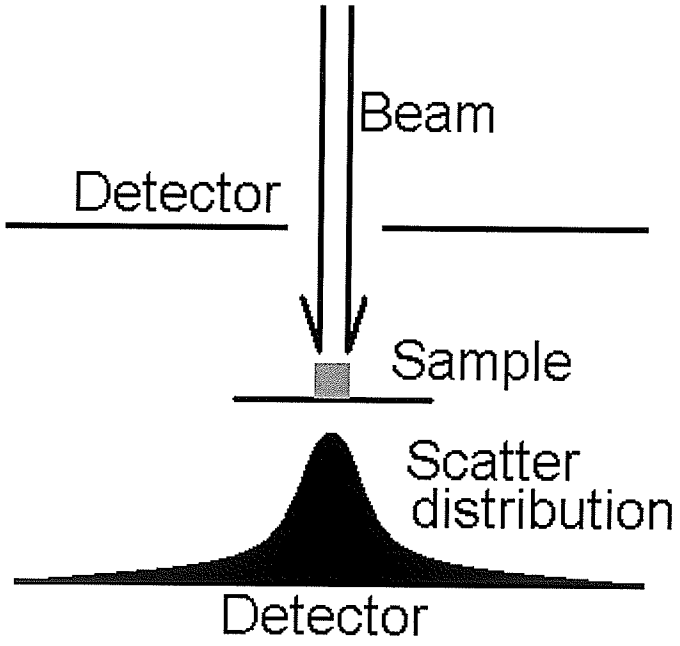


Figure 8.1: Proposed geometry for Compton spectrometry.

## 8.3 Results and Discussion

Several tissue samples were tested, including, normal (50/50) breast tissue, glandular tissue, adipose tissue, calcified (5% calcification by volume) tissue, and a pure calcification. The results are shown in Table 8.1.

The percent difference was calculated for each of the 30 elemental results (5 sets of 6 elements). The average of this percent difference is 48.35%. While this demonstrates a large uncertainty, we note that the largest uncertainty is confined to trace elements, defined in this case as being less than 5% of the total material by weight. If we neglect trace elements, the percent difference is calculated as 3.39%. The percent difference if only the trace elements are considered is 116.4%.

Both a paired Student's *t*-test and a paired Wilcoxon were used to test for correlation. The first test, assuming Gaussian distributions, returned a correlation coefficient of 0.9998, indicating an extremely significant correlation. The second test, which does not make the assumption of Gaussian distributions, returned a correlation coefficient of 0.9429, considered very significant.

Compton spectroscopy may be useful as a fast and cost efficient means of obtaining elemental composition and electron density of a small sample.

Compton spectroscopy may become a potentially useful system for determining the elemental composition of organic molecules as it is sensitive to the organic elements, and requires only the equipment used in CCSR imaging.

Table 8.1: Results of Compton spectrometry for various tissues. First number is experimental results, second number is actual value.

| | H | C | N | O | P | Ca | $\rho_e$ (x$10^{23}$) |
|---|---|---|---|---|---|---|---|
| 50% Glandular | 0.107/0.107 | 0.4056/0.401 | 0.0147/0.025 | 0.4713/0.464 | 0.0004/0.0030 | 0.001/0.0 | 3.264/3.2673 |
| Adipose | 0.114/0.112 | 0.607/0.619 | 0.010/0.017 | 0.264/0.251 | 0.005/0.001 | 0/0 | 3.134/3.108 |
| Glandular | 0.112/0.102 | 0.189/0.184 | 0.040/0.032 | 0.658/0.677 | 0/0.005 | 0.001/0 | 3.398/3.446 |
| Calcification | 0.003/0.002 | 0.004/0 | 0.002/0 | 0.425/0.414 | 0.175/0.185 | 0.391/0.399 | 9.429/9.471 |
| 5% Calcification | 0.094/0.088 | 0.157/0.159 | 0.040/0.028 | 0.638/0.641 | 0.021/0.030 | 0.050/0.055 | 3.771/3.747 |

# 9

# Summary and Future Work

## 9.1 Summary

This thesis work studies the hypothesis that x ray scatter distributions present in mammographic and breast CT primary imaging modalities allow the imaging of 3D electron density distributions, and that these distributions may be used to enhance the sensitivity and specificity of the associated primary imaging modality. Furthermore, the suitability of using x ray scatter distributions to perform spectroscopy of organic tissue is examined. The experiments testing the hypothesis were performed entirely within a simulated environment. The major experiments and findings of this work are, as follows:

**Compton Computed Tomography (Chapter 6)**

- A narrow polyenergetic beam (60-70 keV) was used to image a small pencil-like field of view contained within a cylindrical phantom 8 cm thick and 8 cm in diameter. A dose similar to mammography was used.

- The field of view contained two superimposed lesions of size 1x1x2.5 $mm^3$ .
- Images were produced for a full mammographic dose and $1/10^{th}$ of a mammographic dose, to allow for 10 CT projections. The detector area was also reduced to ¼ the previous value, to investigate the importance of detector size.
- The lesions were clearly visible on all images.
- An ROC study was performed, where the two lesions were placed in random voxels of the phantom over a total of 15 trials. The qualitative results of the ROC study ranged from very good to excellent.

**Compton Mammography (Chapter 7)**

- A narrow polyenergetic beam (15-20 keV) was used to image several slices of a 5x5x5 $cm^3$ simulated accreditation phantom containing 4 types of lesions ranging in calcification content from 1.6% to 5%.
- Images of electron density were produced for each lesion for 5 depths, producing a total of 4 images. Electron density histograms were also produced for two special cases.
- Contrast-to-noise ratio met the Rose criterion for 5% calcifications. Images of 3.2% and 2.4% calcification presented reasonably visible lesions but below the CNR level of the Rose criterion. Extended lesions and calcifications were both visible on an electron density image.

**Compton spectrometry (Chapter 8)**

- Small samples of adipose, 50/50, glandular, calcification, and 5% lesion were analyzed using CCSR spectroscopy
- Neglecting trace elements, the accuracy of the technique in determining relative elemental composition was 4%.

## 9.2 Future Work

One major challenge in the development of CCSR was finding the global minimum in an $n$-dimensional data space, where $n$ was as high as 32. Using limited computational resources, we sampled a small handful of optimization algorithms, selecting a Gauss-Newton algorithm in the end for its computational efficiency and performance in our geometries. A Gauss-Newton algorithm may become unsuitable in future experiments of CCSR, and much work remains to investigate the suitability of other optimization techniques, including simulated annealing, genetic optimization, and neural networks. We have developed techniques to assist our Gauss-Newton algorithm in selecting a global minimum; however some of these techniques are dependent on the breast imaging geometry we have presented in this work. We have also not investigated any manipulation of the data space which may assist in eliminating local minima.

There are a large number of variables involved in the simulation. In some cases, we chose values for these variables which we felt were realistic. However, it is unknown what effect these variables have on the overall imaging process. In effect, we have only explored a limited volume in parameter space. Investigation of the parameter space may allow further optimization of the overall convergence process.

The multiple scatter prediction model assumes a 50/50 glandular adipose/glandular content. However, in some cases the breast composition might be overly glandular ($\rho$=1.04) or fatty ($\rho$=0.93), which could lead to a 4-7% density difference between the sleeve and the breast. Also, molecular differences between water and breast tissue may negatively affect the Doppler-broadened and coherent multiple scatter. Further investigation of these issues is recommended.

We have invested much effort in removing what we felt were the largest simplifying approximations. However, some approximations were retained which we felt were lower priority. For example, we used a non-diverging beam in simulation, while all x ray beams have some level of divergence. In future work, these approximations will need to be addressed.

Compton scatter offers potential for quantitative 3D breast imaging and preliminary results indicate that the information content in Compton scatter is sufficient to detect small simulated calcifications to within 0.25 cm in 5 cm and 8 cm breast phantoms. Our results illustrate that with the advent of state-of-the-art energy sensitive imaging detectors, it is feasible to reconstruct an electron density

image of a phantom using only the Compton scattered photon information due to the interaction of the primary beam with the phantom.

Much of the future work involves the further development of CCSR in an experimental setting. We feel we have shown the robustness of the technique in a simulated environment, however, there are many experimental challenges which need to be addressed when the algorithm is applied in an experimental setting. To begin, a simple experimental geometry may be devised (Figure 9.1). A quasi-monoenergetic pencil beam produced by a filtered mammographic x ray tube is used to irradiate a small water equivalent target. Since dose deposition is no concern in the early stages, a scanning point detector may be used in lieu of an extended area flat panel detector. As mammographic energies are used on a small target, the influence of multiple scatter is limited.

Many applications of CCSR remain to be investigated. Theoretically, the algorithm could be applied to any x ray imaging technique, including CT, radiography, portal dose imaging, or tomosynthesis. In clinical practice, a standard mammography x ray cone beam may be adapted to a scanning monochromatic pencil by installing a scanning monochromator downstream of the x ray tube. We also envisage a scanning energy sensitive ring detector installed upstream of the standard mammography detector system, whether it be film or digital.

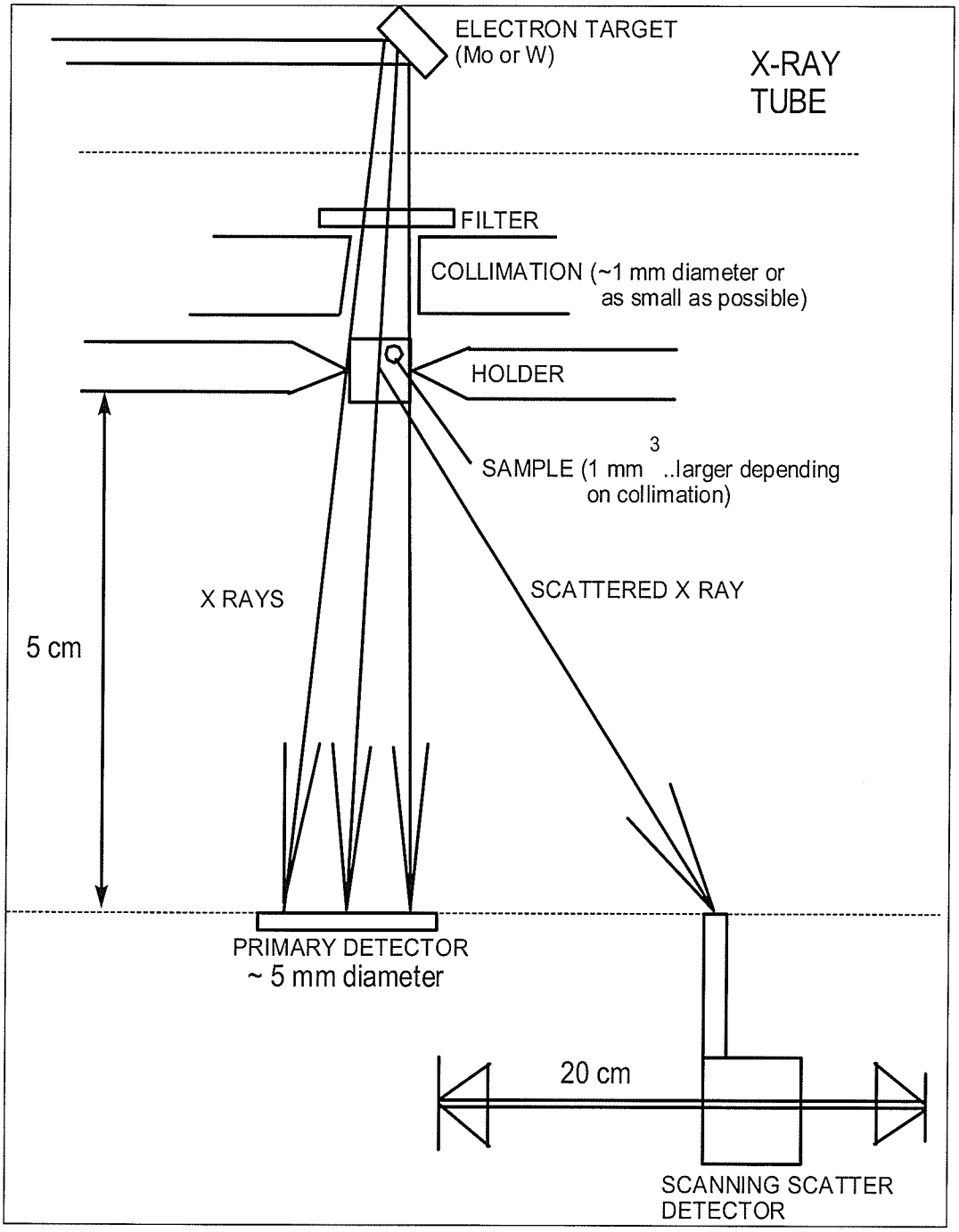


Figure 9.1: Proposed experimental geometry.

There is still a great deal of work to be done before CCSR can move to clinical trial. However, the ability of this approach to generate 3D images from a single projection may allow CCSR to improve the sensitivity and specificity of breast imaging, while retaining comparable dose. When combined with the primary and coherently scattered photons even better results are envisioned. However, we believe that CCSR may significantly improve select x ray modalities such as breast CT and mammography, allowing an increase in sensitivity and specificity. Ultimately, we hope this work will reduce the cost burden in mammography and improve the quality of life in human society.

# A

## Properties of Breast Tissue

The purpose of this appendix is to provide useful data and formulae for the calculation of quantities relating to tissues present in the breast. From the elemental composition by weight and the physical densities of two or more materials, we desire to calculate the electron density and the linear attenuation coefficients of the mixture at various energies.

Let us assume a mixture of at least 2 materials. If we combine the materials in a proportion by *volume*, the physical density of the resulting mixture is:

$$\rho = \sum_{i=1}^{n} p_i \rho_i \qquad \text{(A.1)}$$

where $\rho_i$ is the density and $p_i$ is the proportion by volume of material $i$. The summation is over the total number of materials. The proportion by volume is converted to the proportion by weight through the following formula:

$$p_i^w = \frac{p_i \rho_i}{\rho} \tag{A.2}$$

Electron densities by volume of each element $i$ are then calculated using the following formula:

$$\rho_i^e = p_i^w N_A \frac{Z_i}{A_i} \rho \tag{A.3}$$

The total electron density per unit volume is thus given by:

$$\rho^e = \sum_i \rho_i^e \tag{A.4}$$

where $N_A$ is Avogadro's number, $Z_i$ is the atomic number of the $i$th element, and $A_i$ is the atomic mass number.

Now that we have the total density and the proportion by weight, we can determine the elemental composition of the mixture. The percentage of any element $E$ by weight in the mixture is given by:

$$[\%E]_{mix} = \sum_{i=1}^{N} [\%E]_i \, p_i^w \tag{A.5}$$

where $\%E$ represents the percentage of element E existing in material $i$.

Finally, given the elemental composition and density of our mixture, and

elemental mass attenuation values, the mass attenuation coefficient of the mixture at energy $E$ can be calculated using simple addition:

$$\frac{\mu}{\rho} = \sum_{i=1}^{N} \frac{[\%E]_{mix}}{100} \times \left(\frac{\mu}{\rho}\right)_i \tag{A.6}$$

Table A.1 provides a summary of the breast tissues used in this project. The physical densities and elemental compositions were obtained from Hammerstein[101], while the electron density was calculated using Equation A.3. The mass attenuation coefficients of all tissues were also calculated for energies ranging from 10-70 keV using equation A.6, and are presented in Table A.2.

Table A.1: Elemental composition of materials used in this work

| Tissue Type | Physical Density | Electron Density | H | C | N | O | P | Ca |
|---|---|---|---|---|---|---|---|---|
| 0% (Adipose) | 0.9301 | 3.108 | 0.112 | 0.619 | 0.017 | 0.251 | 0.001 | - |
| 10% | 0.9399 | 3.142 | 0.111 | 0.576 | 0.019 | 0.294 | 0.001 | - |
| 20% | 0.9501 | 3.176 | 0.110 | 0.532 | 0.020 | 0.336 | 0.002 | - |
| 30% | 0.9605 | 3.209 | 0.109 | 0.488 | 0.022 | 0.379 | 0.002 | - |
| 40% | 0.9711 | 3.243 | 0.108 | 0.445 | 0.023 | 0.421 | 0.003 | - |
| 50% (Normal) | 0.9819 | 3.277 | 0.107 | 0.401 | 0.025 | 0.464 | 0.003 | - |
| 60% | 0.9930 | 3.311 | 0.106 | 0.358 | 0.026 | 0.507 | 0.003 | - |
| 70% | 1.0044 | 3.344 | 0.105 | 0.315 | 0.028 | 0.549 | 0.004 | - |
| 80% | 1.0160 | 3.378 | 0.104 | 0.271 | 0.029 | 0.592 | 0.004 | - |
| 90% | 1.0278 | 3.412 | 0.103 | 0.227 | 0.030 | 0.634 | 0.005 | - |
| 100% (Glan.) | 1.0400 | 3.446 | 0.102 | 0.184 | 0.032 | 0.677 | 0.005 | - |
| Carc. 5% | 1.146 | 3.747 | 0.088 | 0.159 | 0.028 | 0.641 | 0.030 | 0.055 |
| Carc. 3.2% | 1.0676 | 3.524 | 0.092 | 0.167 | 0.0295 | 0.655 | 0.0215 | 0.03721 |
| Carc. 2.4% | 1.052 | 3.479 | 0.095 | 0.171 | 0.030 | 0.66 | 0.0175 | 0.028 |
| Carc. 1.6% | 1.0432 | 3.455 | 0.097 | 0.175 | 0.0305 | 0.665 | 0.01347 | 0.01879 |
| $Ca_{10}(PO_4)_6(OH)_2$ | 3.16 | 9.4710 | 0.002 | 0 | 0 | 0.414 | 0.185 | 0.399 |

Table A.2: Mass attenuation coefficients in the mammographic range of materials used in this work.

| | Energy | | | | | | | | | | | | |
|---|---|---|---|---|---|---|---|---|---|---|---|---|---|
| | 10 | 15 | 20 | 25 | 30 | 35 | 40 | 45 | 50 | 55 | 60 | 65 | 70 |
| Adipose | 2.776 | 0.9321 | 0.5 | 0.3467 | 0.2787 | 0.2422 | 0.2207 | 0.2123 | 0.2013 | 0.1930 | 0.1865 | 0.1811 | 0.1766 |
| Normal | 3.7622 | 1.2225 | 0.6271 | 0.4156 | 0.3228 | 0.2735 | 0.2448 | 0.2335 | 0.2193 | 0.2090 | 0.2009 | 0.1945 | 0.1890 |
| Glandular | 4.839 | 1.539 | 0.7648 | 0.4899 | 0.3700 | 0.3066 | 0.2702 | 0.2547 | 0.2374 | 0.2249 | 0.2153 | 0.2078 | 0.2014 |
| Carcinoma (5%) | 11.90 | 3.784 | 1.748 | 1.003 | 0.6753 | 0.5062 | 0.4101 | 0.3606 | 0.3198 | 0.2910 | 0.2700 | 0.2544 | 0.2418 |
| Carcinoma (3.2%) | 9.355 | 2.9756 | 1.394 | 0.8181 | 0.5654 | 0.4343 | 0.3597 | 0.3225 | 0.2901 | 0.2672 | 0.2503 | 0.2376 | 0.2272 |
| Carcinoma (2.4%) | 8.2259 | 2.6163 | 1.237 | 7.360 | 0.5165 | 0.4024 | 0.3373 | 0.3055 | 0.2769 | 0.2566 | 0.2416 | 0.2301 | 0.2208 |
| Carcinoma (1.6%) | 7.097 | 2.257 | 1.079 | 0.6540 | 0.4677 | 0.3705 | 0.3149 | 0.3225 | 0.2901 | 0.2672 | 0.2503 | 0.2376 | 0.2272 |
| Calcification | 146.0 | 46.44 | 20.43 | 10.75 | 6.48 | 4.30 | 3.069 | 2.3731 | 1.8842 | 1.5464 | 1.3092 | 1.1391 | 1.0083 |

# B

## The Question of Unique Solutions

In order for our technique of Compton imaging to be an effective technique for imaging, it is necessary to demonstrate that the inverse technique we use provides unique electron density solutions given the distributions of photon scatter. That is, only one global minimum exists in the objective function f(x), and it is the correct solution. This is not to be confused with the completely different problem of local minima. In this case we answer the question: is there more than one electron density pattern which can provide the scattered photon distribution?

Consider a column of voxels situated in the irradiation zone. Given a particular object geometry, each voxel can be considered to be a 'source' of scattered photons, and likened with a vector of scattered intensity as a function of solid angle and energy. To prove a unique solution exists, consider the properties of a basis B spanning a vector space V:

- B is a minimal generating set of V.

- B is a maximal set of linearly independent vectors, i.e., it is a linearly independent set while no other linearly independent set contains it as a proper subset.
- Every vector in V can be expressed as a linear combination of vectors in B in a *unique* way. For a given vector, the corresponding coefficients in the linear combination are the coordinates of the vector relative to the basis.

If we consider the cumulative scatter photon distribution to be a vector in vector space V, then the electron density distribution producing V would be considered a basis B if we can prove assertion 2, that the vectors are linearly independent. However, there is great difficulty in attempting to generalize the problem, as the vector space V and basis B is a function of:

- electron density distribution
- detector distance
- attenuation properties of the object

As such, it is impossible to verify the basis for all possible combinations of the above parameters. However, a small function has been integrated into the algorithm which checks the linear independence of all voxel scatter vectors during each iteration. Using this algorithm, we have checked all the geometries presented

in this thesis, as well as all estimated iterative geometries tried by the algorithm during convergence.

To examine the effect of noise, Poisson noise was added to each geometry presented in this thesis, and linear independence was verified. Each case was repeated 10,000 times. As of yet, we have yet to discover a single case where we have found the voxels to be linearly dependent.

For a practical example, a simulation was performed using a 5x5x5 $cm^3$ phantom with 3 cm air gaps and a central beam position. For clarity, a monoenergetic beam of 17.5 keV, the mean energy of our mammographic spectrum was used. Figure B.1 shows the geometry, with three highlighted voxels, (a), (b), and (c). These voxels correspond to the $z$ ranges of 3-3.25 cm, 5.5-5.75 cm, and 7.75-8 cm, respectively. Each voxel produces its own basis photon distribution at the detector plane. Simulating $10^8$ photon histories, we obtain the results of Figure B.2. Each photon distribution is characteristic, with differences occurring due to simple geometric differences (positions) as well as attenuation effects. The three distributions shown in Figure B.2 were verified to be unique, as well as the distributions for all intermediary voxels.

Based on the evidence presented here, the possibility of a linearly dependent configuration of voxels is extremely unlikely. All the cases we have explored have demonstrated a unique solution.

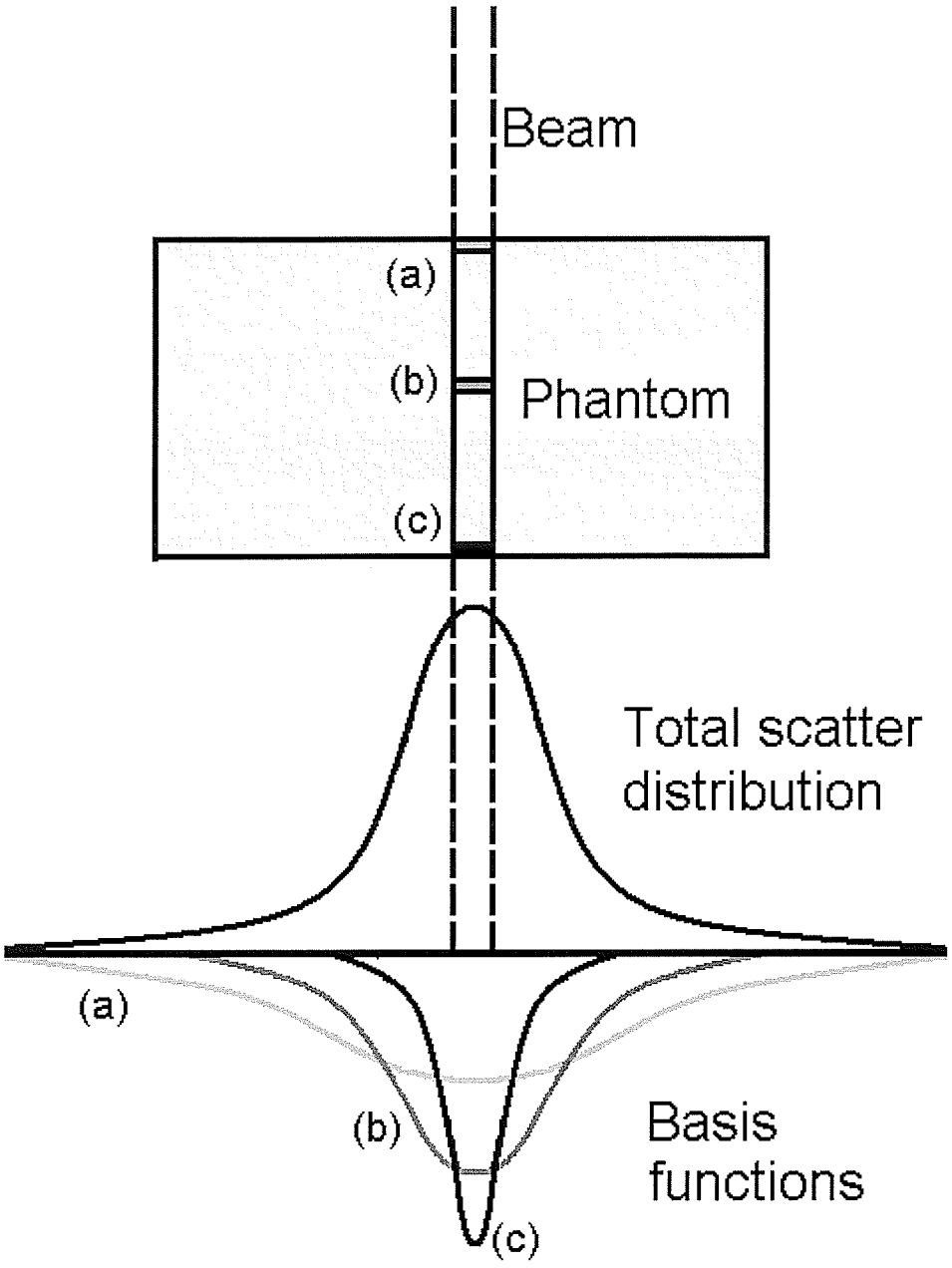


Figure B.1: The scattered photon distribution of each voxel (a), (b), and (c), acts is a basis function in the vector space V, defined here as the total scattered photon distribution.

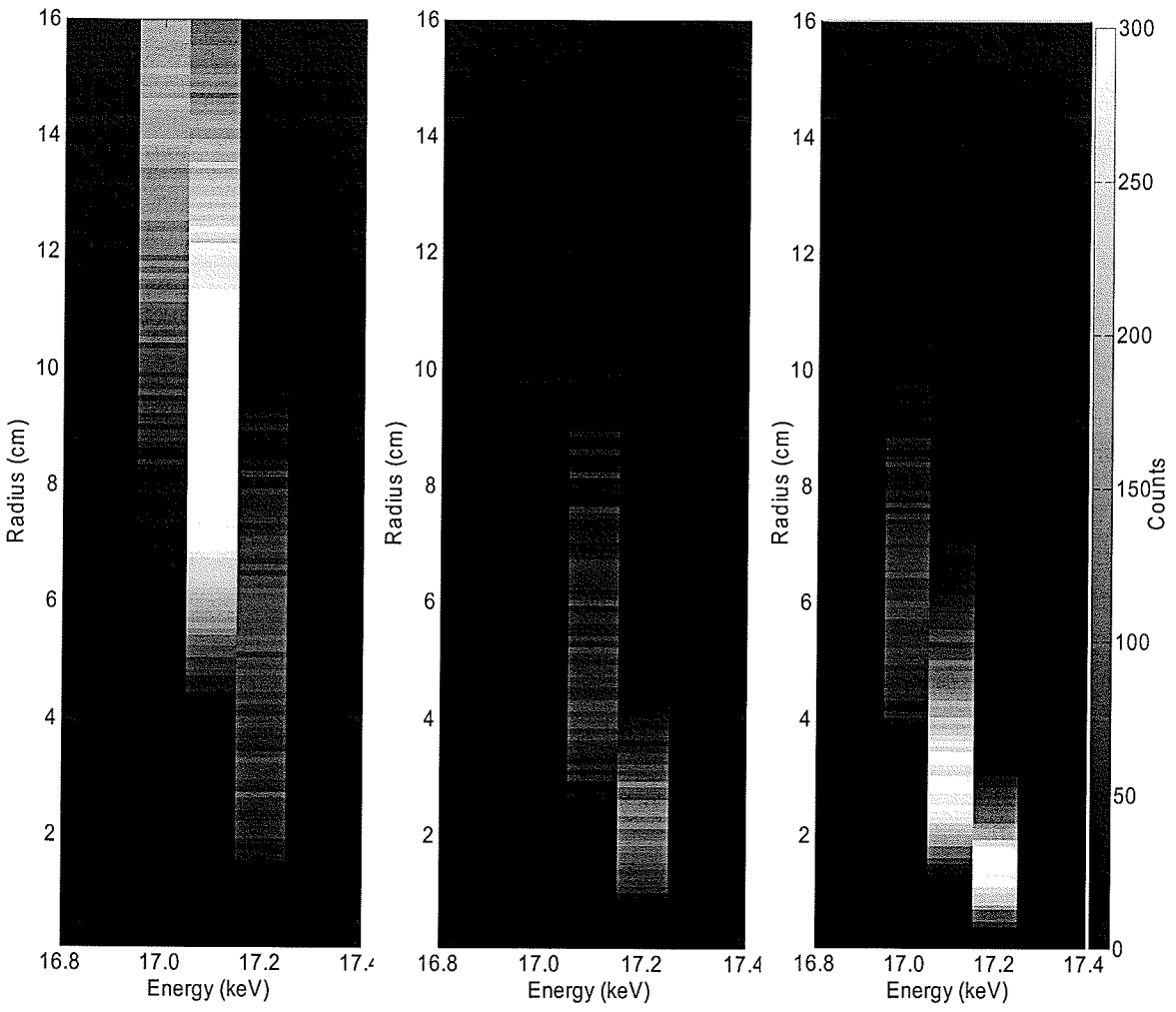


(a) (b) (c)

Figure B.2: Simulated basis functions corresponding to the voxels (a), (b), and (c) indicated in Figure B.1. The photon count colorbar on the right applies to all three figures.

# References


[1] K. Cranley, B.J. Gilmore, G.W.A. Fogarty, and L. Desponds, *Catalogue of Diagnostic Spectra and Other Data*, (The Institute of Physics and Engineering in Medicine, York, U.K., 1997).

[2] J.S. Suri and R.M. Rangayyan, eds. *Recent Advances in Breast Imaging, Mammography, and Computer-Aided Diagnosis of Breast Cancer*. 2006, SPIE: The international Society for Optical Engineering: Bellingham.

[3] J.T. Bushberg, J.A. Seibert, E.M. Leidholdt, and J.M. Boone, *The Essential Physics of Medical Imaging*, (Lippincott Williams & Wilkins, Philadelphia, 2002).

[4] T. Tot, *The Subgross Morphology of Normal and Pathologically Altered Breast Tissue*, in *Recent Advances in Breast Imaging, Mammography, and Computer-Aided Diagnosis of Breast Cancer*, J.S. Suri and R.M. Rangayyan, Editors. 2006, SPIE: Society for Photo-Optical Instrumentation Engineers. p. 1-49.

[5] K.H. Ng, D.A. Bradley, and L.M. Looi, "Elevated trace element concentrations in malignant breast tissues," Br J Radiol. **70,** 375-82 (1997).

[6] D.B. Kopans, *Breast Imaging*, (Lippincoff, Philadelphia, 1989).

[7] S.S. Buchbinder, I.S. Leichter, R.B. Lederman, B. Novak, P.N. Bamberger, H. Coopersmith, and S.I. Fields, "Can the size of microcalcifications predict malignancy of clusters at mammography?" Acad Radiol. **9,** 18-25 (2002).

[8] W.A. Murphy and K. DeSchryver-Kecskemeti, "Isolated clustered microcalcifications in the breast: radiologic-pathologic correlation," Radiology. **127,** 335-41 (1978).

[9] B.B. Muir, J. Lamb, T.J. Anderson, and A.E. Kirkpatrick, "Microcalcification and its relationship to cancer of the breast: experience in a screening clinic," Clin Radiol. **34,** 193-200 (1983).

[10] M. Lanyi, *Morphological analysis of calcifications*, in *Early Breast Cancer: Histopathology, Diagnosis, and Treatment*, J. Zander and J. Baltzer, Editors. 1985, Springer-Verlag: Berlin.

[11] R.R. Millis, R. Davis, and A.J. Stacey, "The detection and significance of calcifications in the breast: a radiological and pathological study," Br J Radiol. **49,** 12-26 (1976).

[12] E.A. Sickles, "Mammographic features of 300 consecutive nonpalpable breast cancers," AJR Am J Roentgenol. **146,** 661-3 (1986).

[13] A. Tan, D.H. Freeman, Jr., J.S. Goodwin, and J.L. Freeman, "Variation in false-positive rates of mammography reading among 1067 radiologists: a population-based assessment," Breast Cancer Res Treat. **100,** 309-18 (2006).

[14] J. Sun, J. Chapman, R. Gordon, R. Sivaramakrishna, M. Link, and E. Fish, "Survival from primary breast cancer after routine clinical use of mammography," Breast J. **8,** 199-208 (2002).

[15] S. Koscielny, M. Tubiana, M.G. Le, A.J. Valleron, H. Mouriesse, G. Contesso, and D. Sarrazin, "Breast cancer: relationship between the size of the primary tumour and the probability of metastatic dissemination," Br J Cancer. **49,** 709-15 (1984).

[16] A. Maffuz, S. Barroso-Bravo, I. Najera, G. Zarco, I. Alvarado-Cabrero, and S.A. Rodriguez-Cuevas, "Tumor size as predictor of microinvasion, invasion, and axillary metastasis in ductal carcinoma in situ," J Exp Clin Cancer Res. **25,** 223-7 (2006).

[17] J. Anttinen, H. Kautiainen, and T. Kuopio, "Role of mammography screening as a predictor of survival in postmenopausal breast cancer patients," Br J Cancer. **94,** 147-51 (2006).

[18] A.H. Olsen, et al., "A model for determining the effect of mammography service screening," Acta Oncol. **44,** 120-8 (2005).

[19] P.J. Klemi, I. Parvinen, L. Pylkkanen, L. Kauhava, P. Immonen-Raiha, O. Rasanen, and H. Helenius, "Significant improvement in breast cancer survival through population-based mammography screening," Breast. **12,** 308-13 (2003).

[20] M. Paziault, et al., "[Pathological characteristics in screening versus clinically-detected breast cancer]," Bull Cancer. **93,** 731-6 (2006).

[21] P.G. Gill, G. Farshid, C.G. Luke, and D.M. Roder, "Detection by screening mammography is a powerful independent predictor of survival in women diagnosed with breast cancer," Breast. **13,** 15-22 (2004).

[22] B.E. Wojcik, M.K. Spinks, and C.R. Stein, "Effects of screening mammography on the comparative survival rates of African American, white, and Hispanic beneficiaries of a comprehensive health care system," Breast J. **9,** 175-83 (2003).

[23] L. Tabar, H.H. Chen, S.W. Duffy, and U.B. Krusemo, "Primary and adjuvant therapy, prognostic factors and survival in 1053 breast cancers diagnosed in a trial of mammography screening," Jpn J Clin Oncol. **29,** 608-16 (1999).

[24] T.L. Bauer, S.M. Pandelidis, and J.E. Rhoads, Jr., "Five-year survival of 100 women with carcinoma of the breast diagnosed by screening mammography and needle-localization biopsy," J Am Coll Surg. **178,** 427-30 (1994).

[25] C.H. Lee, "Screening mammography: proven benefit, continued controversy," Radiol Clin North Am. **40,** 395-407 (2002).

[26] S.W. Duffy, et al., "The impact of organized mammography service screening on breast carcinoma mortality in seven Swedish counties," Cancer. **95,** 458-69 (2002).

[27] X.H. Zhou and R. Gordon, "Detection of early breast cancer: an overview and future prospects," Crit Rev Biomed Eng. **17,** 203-55 (1989).

[28] K. Blanchard, et al., "Long-term risk of false-positive screening results and subsequent biopsy as a function of mammography use," Radiology. **240,** 335-42 (2006).

[29] S.V. Destounis, P. DiNitto, W. Logan-Young, E. Bonaccio, M.L. Zuley, and K.M. Willison, "Can computer-aided detection with double reading of screening mammograms help decrease the false-negative rate? Initial experience," Radiology. **232,** 578-84 (2004).

[30] P. Taylor, J. Champness, R. Given-Wilson, K. Johnston, and H. Potts, "Impact of computer-aided detection prompts on the sensitivity and specificity of screening mammography," Health Technol Assess. **9,** iii, 1-58 (2005).

[31] R. Gordon and R. Sivaramakrishna, "Mammograms are Waldograms: why we need 3D longitudinal breast screening," Appl. Radiol. **28,** 12-25 (1999).

[32] B. Acha, R. Rangayyan, and J.E. Desautels, *Detection of Microcalcifications in Mammograms*, in *Recent Advances in Breast Imaging, Mammography, and Computer-Aided Diagnosis of Breast Cancer*, J. Suri and R. Rangayyan, Editors. 2006, SPIE: Society for Photo-Optical Instrumentation Engineers. p. 291-314.

[33] A. Berrington de Gonzalez and G. Reeves, "Mammographic screening before age 50 years in the UK: comparison of the radiation risks with the mortality benefits," Br J Cancer. **93,** 590-6 (2005).

[34] D. Goldfrank, et al., "Effect of Mammography on Breast Cancer Risk in Women with Mutations in BRCA1 or BRCA2," Cancer Epidemiol Biomarkers Prev. **15,** 2311-3 (2006).

[35] K. Faulkner, "Mammographic screening: is the benefit worth the risk?" Radiat Prot Dosimetry. **117,** 318-20 (2005).

[36] H.D. Cheng, X. Cai, X. Chen, L. Hu, and X. Lou, "Computer-aided detection and classification of microcalcifications in mammograms: A survey," Pattern Recogn. **36,** 2967-2991 (2003).

[37] R.L. Birdwell, D.M. Ikeda, K.F. O'Shaughnessy, and E.A. Sickles, "Mammographic characteristics of 115 missed cancers later detected with screening mammography and the potential utility of computer-aided detection," Radiology. **219,** 192-202 (2001).

[38] A.J. Maxwell, I.M. Hanson, C.J. Sutton, J. Fitzgerald, and J.M. Pearson, "A study of breast cancers detected in the incident round of the UK NHS Breast Screening Programme: the importance of early detection and treatment of ductal carcinoma in situ.," Breast. **10,** 392-398 (2001).

[39] A. Poulos and M. Rickard, "Compression in mammography and the perception of discomfort," Australas Radiol. **41,** 247-52 (1997).

[40] E.J. Hall and A.J. Giaccia, *Radiobiology for the Radiobiologist, 5th ed.*, (Lippincott Williams & Wilkins, Philadelphia, 2005).

[41] K.N. Feigin, D.M. Keating, P.M. Telford, and M.A. Cohen, "Clinical breast examination in a comprehensive breast cancer screening program: contribution and cost," Radiology. **240,** 650-5 (2006).

[42] B.J. Harvey, A.B. Miller, C.J. Baines, and P.N. Corey, "Effect of breast self-examination techniques on the risk of death from breast cancer," Cmaj. **157,** 1205-12 (1997).

[43] J. Li, et al., "Identification of biomarkers for breast cancer in nipple aspiration and ductal lavage fluid," Clin Cancer Res. **11,** 8312-20 (2005).

[44] W. Zhang, et al., "Biomarker analysis on breast ductal lavage cells in women with and without breast cancer," Int J Cancer. **119,** 359-64 (2006).

[45] E.C. Fear, X. Li, S.C. Hagness, and M.A. Stuchly, "Confocal microwave imaging for breast cancer detection: localization of tumors in three dimensions," IEEE Trans Biomed Eng. **49,** 812-22 (2002).

[46] V. Corsetti, et al., "Role of ultrasonography in detecting mammographically occult breast carcinoma in women with dense breasts," Radiol Med (Torino). **111,** 440-8 (2006).

[47] A. Godavarty, A.B. Thompson, R. Roy, M. Gurfinkel, M.J. Eppstein, C. Zhang, and E.M. Sevick-Muraca, "Diagnostic imaging of breast cancer using fluorescence-enhanced optical tomography: phantom studies," J Biomed Opt. **9,** 488-96 (2004).

[48] M.C. Abreu, et al., "Clear-PEM: a dedicated PET camera for improved breast cancer detection," Radiat Prot Dosimetry. **116,** 208-10 (2005).

[49] T. Suzuki, K. Uno, and A. Kubo, "[Usefulness of 18F-FDG PET in the diagnosis for breast cancer patients]," Nippon Rinsho. **64,** 504-10 (2006).

[50] D. Fukuoka, T. Hara, and H. Fujita, *Detection, Characterization, and Visualization of Breast Cancer using 3D Ultrasound Images*, in *Recent*

*Advances in Breast Imaging, Mammography, and Computer-Aided Diagnosis of Breast Cancer*, J. Suri and R. Rangayyan, Editors. 2006, SPIE: Society for Photo-Optical Instrumentation Engineers. p. 557-566.

[51] J.M. Boone, T.R. Nelson, K.K. Lindfors, and J.A. Seibert, "Dedicated Breast CT: Radiation Dose and Image Quality Evaluation," Med. Phys. **221,** 657-667 (2001).

[52] B. Chen and R. Ning, "Cone-beam volume CT breast imaging: feasibility study," Med. Phys. **29,** 755-70 (2002).

[53] C.D. Lehman, "Screening MRI for women at high risk for breast cancer," Semin Ultrasound CT MR. **27,** 333-8 (2006).

[54] P.G. Lale, "The examination of internal tissues, using gamma-ray scatter with a possible extension to megavoltage radiography," Phys. Med. Biol. **4,** 159-67 (1959).

[55] P.G. Lale, "The examination of internal tissues by high-energy scattered x-radiation," Radiology. **90,** 510-7 (1968).

[56] F.T. Farmer and M.P. Collins, "A further appraisal of the Compton scattering method for determining anatomical cross-sections of the body," Phys. Med. Biol. **19,** 808-18 (1974).

[57] J.J. Battista, L.W. Santon, and M.J. Bronskill, "Compton Scatter Imaging of Transverse Sections: Corrections for Multiple Scatter and Attenuations," Phys. Med. Biol. **22,** 229-244 (1977).

[58] J.J. Battista and M.J. Bronskill, "Compton-scatter tissue densitometry: calculation of single and multiple scatter photon fluences," Phys. Med. Biol. **23,** 1-23 (1978).

[59] A. Del Guerra, R. Bellazzini, G. Tonelli, and R. Venturi. *Application of the Method of Monte Carlo to Compton Scattering Radiography in Homogenous Media*. SLAC-PUB-2648 1981 [cited; Available from: file://C:%5CPAPERS%5Cdelguerra_1981.pdf.

[60] J.J. Battista and M.J. Bronskill, "Compton scatter imaging of transverse sections: an overall appraisal and evaluation for radiotherapy planning," Phys. Med. Biol. **26,** 81-99 (1981).

[61] P.R. Duke and J.A. Hanson, "Compton scatter densitometry with polychromatic sources," Med. Phys. **11,** 624-32 (1984).

[62] L. Brateman, A.M. Jacobs, and L.T. Fitzgerald, "Compton scatter axial tomography with x-rays: SCAT-CAT," Phys. Med. Biol. **29,** 1353-70 (1984).

[63] B. Achmad and E.M. Hussein, "An X-ray Compton scatter method for density measurement at a point within an object," Appl Radiat Isot. **60,** 805-14 (2004).

[64] F. El Khettabi, I. Yaar, and E.M. Hussein, "A three-dimensional x-ray scattering system for multi-parameter imaging of the human head," Phys Med Biol. **48,** 3445-58 (2003).

[65] P. Arsenault and E. Hussein, "Image Reconstruction From the Compton Scattering of X-Ray Fan Beams in Thick/Dense Objects," IEEE Trans Nucl Sci. **53,** 1622-1633 (2006).

[66] D.R. Dance and G.J. Day, "The computation of scatter in mammography by Monte Carlo methods," Phys. Med. Biol. **29,** 237-47 (1984).

[67] J.M. Boone, K.K. Lindfors, V.N. Cooper, and J.A. Seibert, "Scatter/primary in mammography: comprehensive results," Med. Phys. **27,** 2408-16 (2000).

[68] D.L. Batchelar and I.A. Cunningham, "Material-specific analysis using coherent-scatter imaging," Med. Phys. **29,** 1651-60 (2002).

[69] R.L. Clarke, "A Gamma Ray Scanner for Diagnostic Radiology." **2270,** (1965).

[70] R.L. Clarke and G. Van Dyk, "A new method for measurement of bone mineral content using both transmitted and scattered beams of gamma-rays," Phys Med Biol. **18,** 532-539 (1973).

[71] R.J. Leclair and P.C. Johns, "A semianalytic model to investigate the potential applications of x-ray scatter imaging," Med. Phys. **25,** 1008-1020 (1998).

[72] R.J. Leclair and P.C. Johns, "X-ray forward-scatter imaging: Experimental Validation of model," Med. Phys. **28,** 210-219 (2001).

[73] J.E. Cunningham, A.L. Jurj, L. Oman, A.E. Stonerock, D.K. Nitcheva, and T.E. Cupples, "Is risk of axillary lymph node metastasis associated with proximity of breast cancer to the skin?" Breast Cancer Res Treat, (2006).

[74] S.H. Estourgie, O.E. Nieweg, and B.B. Kroon, "High incidence of in-transit metastases after sentinel node biopsy in patients with melanoma," Br J Surg. **91,** 1370-1 (2004).

[75] D.W.O. Rogers and I. Kawrakow, "The EGSnrc Code System: Monte Carlo Simulation of Electron and Photon Transport," (2003).

[76] G. Marsaglia and A. Zaman, "A new class of random number generators," Annals of Applied Probability. **1,** 462-480 (1991).

[77] D.W. Rogers, "Fifty years of Monte Carlo simulations for medical physics," Phys Med Biol. **51,** R287-301 (2006).

[78] R.E. Bentley, J.C. Jones, and S.C. Lillicrap, "X-ray spectra from accelerators in the range 2 to 6 MeV," Phys Med Biol. **12,** 301-314 (1967).

[79] K.G. Vosburgh and R.S. Newbower, "Moore's Law, disruptive technologies, and the clinician," Stud Health Technol Inform. **85,** 8-13 (2002).

[80] J.F. Williamson and M.J. Rivard, *Quantitative dosimetry methods for brachytherapy*, in *Brachytherapy Physics*, B.R. Thomadsen, M.J. Rivard, and W.M. Butler, Editors. 2005, Medical Physics Publishing: Madison, WI. p. 233-294.

[81] J.E. Cygler, G.M. Daskalov, G.H. Chan, and G.X. Ding, "Evaluation of the first commercial Monte Carlo dose calculation engine for electron beam treatment planning," Med Phys. **31,** 142-53 (2004).

[82] E. Heath, J. Seuntjens, and D. Sheikh-Bagheri, "Dosimetric evaluation of the clinical implementation of the first commercial IMRT Monte Carlo treatment planning system at 6 MV," Med Phys. **31,** 2771-9 (2004).

[83] C.L. Hartmann Siantar, et al., "Description and dosimetric verification of the PEREGRINE Monte Carlo dose calculation system for photon beams incident on a water phantom," Med Phys. **28,** 1322-37 (2001).

[84] J.M. Boone and J.A. Seibert, "Monte Carlo simulation of the scattered radiation distribution in diagnostic radiology," Med Phys. **15,** 713-20 (1988).

[85] N. Petoussi-Henss, M. Zanki, U. Fill, and D. Regulla, "The GSF family of voxel phantoms," Phys Med Biol. **47,** 89-106 (2002).

[86] I.J.e.a. Chetty, "Issues associated with clinical implementation of Monte Carlo-based treatment planning: report of the AAPM Task Group No. 105," Med Phys. **submitted,** (2006).

[87] U. Fano, "Note on the Bragg-Gray cavity principle for measuring energy dissipation," Radiat Res. **1,** 237-40 (1954).

[88] I. Kawrakow, "Accurate condensed history Monte Carlo simulation of electron transport. II. Application to ion chamber response simulations," Med Phys. **27,** 499-513 (2000).

[89] J. Seuntjens, I. Kawrakow, J. Borg, F. Hobelia, and D.W. Rogers, *Calculated and measured air-kerma response of ionization chambers in low and medium energy photon beams*, in *Recent developments in accurate radiation dosimetry, Proc. of an Int'l Workshop*, J. Seuntjens and P. Mobit, Editors. 2002, Medical Physics Publishing: Madison. p. 69-84.

[90] W.R. Nelson, H. Hirayama, and D.W.O. Rogers, *The EGS4 Code System*, in *Report SLAC-265*. 1985, Stanford Linear Accelerator Center: Stanford, California.

[91] J.H. Hubbell and S.M. Seltzer, *Tables of X-Ray Mass Attenuation Coefficients and Mass Energy-Absorption Coefficients 1 keV to 20 MeV for Elements Z = 1 to 92 and 48 Additional Substances of Dosimetric Interest.* 1995, National Institute of Standards and Technology: Gaithersburg, MD.

[92] J.H. Hubbell, "Photon Mass Attenuation and Energy-absorption Coefficients from 1 keV to 20 MeV," Int J Appl Radiat. **33,** 1269-1290 (1982).

[93] M.J. Berger and J.H. Hubbell, *XCOM: Photon Cross Sections on a Personal Computer*, in *Report NBSIR87–3597*. 1987, NIST: Gaithersburg, MD.

[94] J.H. Hubbell, "Review of photon interaction cross section data in the medical and biological context," Phys Med Biol. **44,** R1-22 (1999).

[95] F. Attix, *Introduction to Radiological Physics and Radiation Dosimetry*, (John Wiley and Sons, Canada, 1986).

[96] P.C. Johns and M.J. Yaffe, "X-ray characterisation of normal and neoplastic breast tissues," Phys Med Biol. **32,** 675-95 (1987).

[97] R. Ribberfors, "Relationship of the relativistic Compton cross section to the momentum distribution of bound electron states," Phys. Rev. B. **12,** 2067-2074 (1975).

[98] D. Brusa, G. Stutz, J. Riveros, J.M. Fernandez-Verea, and F. Salvat, "Fast sampling

algorithm for the simulation of photon Compton scattering," Nuc. Inst. Meth. **A379,** 167-175 (1996).

[99] P.C. Johns and M.J. Yaffe, "Coherent scatter in diagnostic radiology," Med. Phys. **10,** 40-50 (1983).

[100] J.H. Hubbell and I. Overbo, "Relativistic atomic form factors and photon coherent scattering cross sections," Phys Chem Ref Data. **9,** (1979).

[101] G.R. Hammerstein, D.W. Miller, D.R. White, M.E. Masterson, H.Q. Woodard, and J.S. Laughlin, "Absorbed radiation dose in mammography.," Radiology. **130,** 485-491 (1979).

[102] K. Bliznakova, Z. Bliznakov, V. Bravou, Z. Kolitsi, and N. Pallikarakis, "A three-dimensional breast software phantom for mammography simulation," Phys Med Biol. **48,** 3699-719 (2003).

[103] E. Storm and H.I. Israel, "Photon cross sections from 1 keV to 100 MeV for elements Z=1 to Z=100," Atomic Data and Nuclear Data Tables. **7,** 565-681 (1970).

[104] D. Chow, A. Loshak, M. van der Berg, M. Frank, T.J. Barbee, and S. Labov, "High-resolution gamma-ray spectrometers using bulk absorbers coupled to Mo/Cu multilayer superconducting transition-edge sensors," Proc. SPIE. **4141,** 67-75 (2000).

[105] G. Knoll, *Radiation Detection and Measurement, 3rd ed.*, 2 (John Wiley and Sons, New York, 2000).

[106] G. Lutz, *Semiconductor Radiation Detectors*, (Springer-Verlag, Berlin, 1999).

[107] U. Fano, "On the theory of ionization yield of radiations in different substances," Phys. Rev. B. **70,** (1946).

[108] G. Bale, A. Holland, P. Seller, and B. Lowe, "Cooled cdznte detectors for x-ray astronomy," Nucl. Instr. and Meth. **A436,** 150-154 (1999).

[109] F. Biggs, "Hartree-Fock Compton Profiles for the Elements," Atomic Data and Nuclear Data Tables. **16,** 201-309 (1975).

[110] T.F. Coleman and Y. Li, "An Interior, Trust Region Approach for Nonlinear Minimization Subject to Bounds," SIAM Journal on Optimization. **6,** 418-445 (1996).

[111] S. Kirkpatrick, C.D.J. Gerlatt, and M.P. Vecchi, "Optimization by Simulated Annealing," Science. **220,** 671-680 (1983).

[112] T.F. Coleman and Y. Li, "On the Convergence of Reflective Newton Methods for Large-Scale Nonlinear Minimization Subject to Bounds," Mathematical Programming. **67,** 189-224 (1994).

[113] J.J. More, *The Levenberg-Marquardt Algorithm: Implementation and Theory*, in *Numerical Analysis*, G.A. Watson, Editor. 1977, Springer-Verlag: Philadelphia. p. 105-116.

[114] J.M. Boone, "Glandular breast dose for monoenergetic and high-energy X-ray beams: Monte Carlo assessment," Radiology. **213,** 23-37 (1999).

[115] R.A. Lewis, "Medical phase contrast x-ray imaging: current status and future prospects," Phys Med Biol. **49,** 3573-83 (2004).

[116] R. Lawaczeck, V. Arkadiev, F. Diekmann, and M. Krumrey, "Monochromatic x-rays in digital mammography," Invest Radiol. **40,** 33-9 (2005).

[117] E. Van Uytven, S. Pistorius, and R. Gordon, "An iterative three-dimensional electron density imaging algorithm using uncollimated Compton scattered x rays from a polyenergetic primary pencil beam," Med Phys. **34,** 256-265 (2007).

[118] C.J. Kotre, "The effect of background structure on the detection of low contrast objects in mammography," Br J Radiol. **71,** 1162-7 (1998).

[119] A. Calicchia, M. Gambaccini, P.L. Indovina, F. Mazzei, and L. Pugliani, "Niobium/molybdenum K-edge filtration in mammography: contrast and dose evaluation," Phys Med Biol. **41,** 1717-26 (1996).

[120] M.J. Mooney, S.S. Naga, R.D. Speller, and T. Koligliatis, "Monitoring and correction of multiple scatter during clinical Compton scatter densitometry measurements," Phys. Med. Biol. **41,** 2399-410 (1996).

[121] *Digital Mammography Accreditation Phantom.* [cited 2007 April 1]; Available from: http://www.cirsinc.com/015dm_mammo.html.

[122] H.B. Mann and D.R. Whitney, "On a test of whether one of 2 random variables is stochastically larger than the other," Annals of Mathematical Statistics. **18,** 50-60 (1947).

[123] F. Wilcoxon, "Individual comparisons by ranking methods," Biometrics Bulletin. **1,** 80-83 (1945).

[124] C. Spearman, "The proof and measurement of association between two rings," Amer. J. Psychol. **15,** 72-101 (1904).

[125] P.L. Warren and P.Y. Shadforth, *Scope and Limitations for Semi-Quantitative XRF Analysis*. 1999, The International Centre for Diffraction Data: Newtown Square.

[126] G. Hazan, I. Leichter, E. Loewinger, A. Weinreb, and G.C. Robin, "The early detection of osteoporosis by Compton gamma ray spectroscopy," Phys Med Biol. **22,** 1073-84 (1977).

[127] S. Naydenov, V. Ryzhikov, and C. Smith. *Radiographic Spectroscopy of Atomic Composition of Materials: a Multi-Energy Approach*. in *Nuclear Science Symposium*. 2004. Rome, Italy.